Zinc stannate modified graphitic carbon nitride for the photocatalytic reduction of Cr(VI) to Cr(III)

N Gobile

orcid.org/0000-0003-1110-1299

Dissertation submitted in fulfilment of the requirements for the degree *Master of Science in Chemistry* at the North West University

Supervisor: Prof. D.C. Onwudiwe

Co-supervisor: Dr. O.A. Oyewo

Graduation ceremony: November 2022

Student number: 17103061

DECLARATION

I hereby declare that the work presented in this research project entitled: “Zinc stannate modified graphitic carbon nitride for the photocatalytic reduction of Cr(VI) to Cr(III)” submitted for the requirement of MSc degree in chemistry to the Department of Chemistry, North-West University, Mafikeng Campus is an original research work of my own under the supervision of Prof D.C. Onwudiwe. This research work has not previously been submitted to any other University or by another student of the North-West University or other University.

Signature: ----------

Nombulelo Gobile

Signature: ----------

Prof D.C Onwudiwe

Signature: ----------

Dr. O.A. Oyewo

DEDICATION

I dedicate this dissertation to my family, whom I left to finish my studies, my husband and daughter.

ACKNOWLEDGEMENTS

I would like to express my deepest gratitude to my supervisors Prof Damian Onwudiwe and Dr Oyewo for their great knowledge, understanding, encouragement and professional guidance that have made this dissertation possible.

The Department of Chemistry is also acknowledged for allowing me the opportunity to further my studies, as well as all the technical staff for their help and support.

The Inorganic and Materials Chemistry Research Group for their inputs and encouragement.

I would also like to thank my parents and extended family for their love, encouragement and financial support, it is greatly appreciated.

Lastly I thank God for making this work possible through the toughest times.

TABLE OF CONTENTS

LIST OF FIGURES

LIST OF TABLES

LIST OF SCHEMATIC DIAGRAMS

LIST OF ABBREVIATIONS

ZnO	Zinc oxide
ZTO	Zinc tin oxide
g-C_3N_4	Graphitic Carbon Nitride
XRD	X-ray Diffractometry
SEM	Scanning Electron Microscopy
TEM	Transmission Electron Microscopy
PL	Photoluminescence
UV-Vis	Ultraviolet visible
Eg	Energy Band Gap
CB	Conduction Band

VB	Valence Band
LUMO	Lower Unoccupied Molecular Orbital
ZTO-ZnO	Zinc tin oxide/Zinc oxide
WHO	World Health Organization
LIBs	Lithium ion batteries
DSSC	Dye sensitized solar cells
Zndtc	Zinc dithoicarbamate
H_2S	Hydrogen sulphide
Dtc	Dithiocarbamate
ZnS	Zinc sulphide
HRTEM	High Resonance Transmission Electron Microscopy
GC-MS	Gas chromatography – mass spectrometry

ABSTRACT

Water is one of the most important natural resources for basic human life. Its pollution has become a serious threat to the survival of both humans and animals. Most water bodies have become dumping sites due to industrial growth, human population growth and urbanization. Over 30% of the world's population still relies on these contaminated water bodies for drinking water. Among these contaminants, Cr(VI) is of great concern because of its ease of solubility and mobility therefore finding its way to the environment and water bodies, leaving all living organisms that use these resources exposed to the pollutant. Once it accumulates to a certain extent, Cr(VI) severely threatens human health, since it is carcinogenic and mutagenic. According to the World Health Organisation (WHO), the permissible limit for chromium in water is 0,1mg/L. To address the problems of water pollution, and specifically of Cr(VI) removal, there is ongoing research to explore more efficient, environmentally safe and cost effective methods of environmental remediation.

Photocatalysis has proven to be a more promising method in wastewater treatment, due to its safe, cost effectiveness and environmental friendliness, more so as it uses abundant energy

from the sunlight. Semiconductors are used as tools for the process of photocatalysis as they have a band gap which promotes generation of electrons and holes responsible for the production of radicals which are used in the process of pollutant degradation. However, to utilize the process to its fullest capabilities the right semiconductor needs to be employed for the process. Semiconductors such as ZnO and SnO have limitation of efficiency and practical application due to electron-hole recombination since most semiconductors absorb in the UV region. Therefore, the design of semiconductors that are able to overcome this limitation need to be revised, through the right band gap alignment. Through modification of traditional semiconductors ZnO and SnO by forming a heterojunction the bad gap will be reduced thus allowing the nanoparticle to absorb more in the UV region hence improving its optical properties and enhancing its photocatalytic properties as well.

This research reports the modification of traditional semiconductor ZnO and SnO through the synthesis of heterojunction compound of Zn_2SnO_4-ZnO nanoparticles which were subsequently incorporated into graphitic carbon nitride using high temperature solid state method. The nanoparticles were then used for the application of the reduction of Cr(VI) to Cr(III) in water. In the process of the synthesis of the heterojunction, characterization revealed that at lower temperature of 600 ºC the Sn salt used acted as a dopant and did not form the heterojunction compound. Only at high temperature of about 1000 ºC and high concentration of Sn (15, 20 & 30%) was the heterojunction obtained as per XRD results. Scanning electron microscopy (SEM) and transmission electron microscopy (TEM) revealed that there was a variation in the size and shape with increase in concentration of Sn and also between the Sn doped samples and the Zn_2SnO_4-ZnO nanoparticles, with ZTO-ZnO showing two different morphologies. Optical properties were studied using photoluminescent (PL) and UV-Vis spectrophometer. All samples were found to exhibit absorption in the UV and visible region. Furthermore, the heterojunction at higher Sn concentration (20 & 30%) were selected to be incorporated into g-C_3N_4 as they revealed more positive results then the ones at lower concentration. The g-C_3N_4/ZTO-ZnO nanocomposite displayed peaks from the precursor materials: ZTO-ZnO and g-C_3N_4, which confirmed the incorporation of ZTO-ZnO nanoparticles into the g-C_3N_4.

The photocatalytic properties of the two nanocomposite: g-C_3N_4/ZTO-ZnO@20% and gC_3N_4/ZTO-ZnO@30%, were evaluated using chromate(VI) salt. Photocatalytic reaction parameters including

- the effects of solution pH,
- effect of photocatalyst (g-C_3N_4/ZTO-ZnO@20) dosage,
- effect of initial concentration of Cr(IV) on the rate of reduction of Cr(IV) were evaluated.

The solution pH was varied from 2 to 8, and pH 2 displayed the highest removal of Cr(VI) at 99.2 and 72% for the g-C_3N_4/ZTO-ZnO@20% and gC_3N_4/ZTO-ZnO@30%, respectively.

The effect of photocatalyst dosage was only performed for the (g-C_3N_4/ ZTO-ZnO@20) composite due to its efficiency within the solution pH. The highest percentage chromium removal was found to be 99.2% at photocatalyst loading of 2 g/L and the lowest was 64% for 0.5g/L. Finally, the kinetic study of the photocatalytic reaction showed an increase in the overall rate constant *k* with increase in initial Cr(VI) concentration.

CHAPTER 1

1. INTRODUCTION AND PROBLEM STATEMENT

1.1. Introduction

Water pollution is the contamination of water by foreign matter, which leads to the deterioration of water quality. Water is one of the most important and valuable natural resources and it is crucial for the subsistence of all living organisms including humans, food production, and economic development. Presently, many cities are faced with a serious shortage of water and approximately 40 percent of the world's food supply is grown under irrigation and an extensive variety of industrial processes is dependent on water [1]. Humanity is faced by one of the most important challenges, which is to conserve and sustain natural resources, including water, for increased food production at the same time protecting the environment. The fast-growing world population and rapidly advancing industrialization has caused more demand than ever for the declining supply of water[2].

The disposal of waste into receiving water bodies is practiced with little or no regard of their receiving capacities. Pollution of water bodies such as rivers has become a major problem which is accumulating at a fast rate due to the inadequacy of surface water quality protection measures and sanitation [1]. Rivers and dams have become home for waste. The main sources of different pollutants are shown in Fig 1.1.

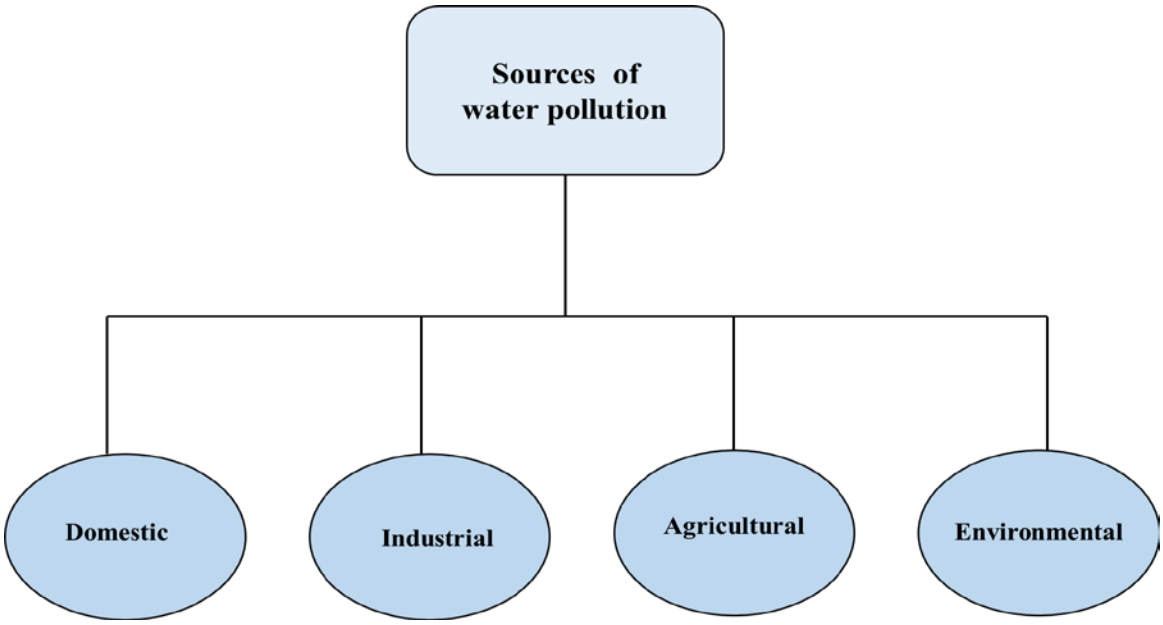

Figure 1. 1: Sources of water pollution.

Domestic wastes are usually generated from household use, *i.e.*, sanitary wastewater and sewage. On the other hand, industrial wastes are generated by industries such as leather tanning, metal plating, steel manufacturing and mining. Agricultural wastes are from fertilizers and pesticides, and lastly environmental wastes could emanate from oil spills and dumping of dirt into different water bodies [3, 4].

As the world's population increases, there is a general growth in the world's economy; hence, increasing the demand for industrial and agricultural production. South Africa is one of the world's leading coal producers in the mining industry [5]. In the process of meeting the increased demand of coal supply, the mining industries find themselves having to release increased levels of wastewater generated during production of coal. Coal combustion wastes contain varieties of toxic compounds such as carbon monoxide (CO), sulfur dioxide (SO_2) and sulfur trioxide (SO_3) [6, 7]. Among the wastes disposed by these mining industries are the heavy metals which find their way into surface water bodies such as river, dams and lakes. Extreme attention has been drawn to wastewater pollution produced by heavy metal ions [8].

Apart from the mining industries, companies that work with heavy metals such as Cd, Cr, Cu, Ni, As, Pb, and Zn, are the most hazardous among the chemical industries. This is due to the release of massive amounts of metal-contaminated wastewater into the environment. Since these metals have high solubility, they can be easily absorbed by living organisms in the aquatic environment. In the event where they are adsorbed by the living organism, they are said to have entered the food chain and may accumulate in the human body through digestion beyond permitted concentration, which can cause severe health disorder [9]. Therefore, making it a very essential step to ensure that metal contaminated wastewater is treated before releasing it to the environment. Among these heavy metals, Cr is of particular interest because of its biological and environmental effects which include but not limited to its carcinogenetic effect on human's health [10] .

Of particular interest to this study was chromium; this heavy metal has been widely used in several industries, such as leather tanning, metal plating, steel manufacturing, military purposes, as well as in the pigment and refractory industries [11]. It is a member of the heavy metal group whose character ranges from being an important trace metal to a deadly toxin. Its character is dependent on its oxidation state, and the most stable forms are +3 to +6. Cr(III) is an essential nutrient that helps the body to utilise sugar protein and fat [12]. At oxidative state

of +3, it is relatively insoluble, poorly adsorbed into cell tissue and does not bioaccumulate. While Cr(VI), on the other hand, is mobile as it is soluble, simply absorbed into cell tissues and can bioaccumulate in the human body and prove to be deadly [13]. Many countries in the world have included Cr(VI) as one of the priority pollutants in their list of pollutants. This is due to its toxicity and carcinogenic properties known for several years [11, 14]. The health organs that are affected due to high exposure of Cr(VI) are the lungs, liver and kidney. These organs play a major role in the functioning of the human body, therefore high concentration exposure to Cr(VI) could lead to death [15, 16].

Various techniques have been used in order to treat Cr(VI) contamination, these include: ion exchange, electrocoagulation, membrane separation, adsorption, electrochemical precipitation, solvent extraction, evaporation, reverse osmosis and biosorption [17-19]. However, despite the efficiency and progress attained by these techniques, there are certain setbacks that are associated with them such as generation of sludge, production of secondary pollutants, high maintenance in terms of cost and low efficiency. These setbacks limit their real-life applications.

Since current conventional methods are not fully equipped to remove Cr(VI), photocatalysis has emerged as a technique that utilizes sunlight or ultraviolet light to completely remove this heavy metal in wastewater without leaving traces of toxic by-product [20]. A few challenges associated with photocatalysis including slow reduction rate and poor reduction efficiency due to the recombination of electron-hole [20], could be addressed through the design of the right band alignment by the combination of two or more semiconductors to form a heterojunction [21]. Band alignment address fast electron hole recombination and help alter absorption region from ultraviolet to visible region. This makes it a good candidate for more effective and efficient removal of Cr(VI) in wastewater.

1.2. Problem statement

South Africa is one of world's leading chromite producing countries in the world [22]. Accounting for about 40% of chromite production by mining industry and some of the other chromium-based product factories. During the disposal process, the harmful Cr(VI) finds its way into the environment, leaving all living organisms that use resources such as rivers and dams exposed to the pollutant. Unlike organic pollutants, chromium is not biodegradable, it can easily enter the food chain and accumulate in living bodies over their life span. According to the World Health Organisation (WHO), the permissible limit for chromium in

water is 0.1mg/L. Anything > 0.1mg/L results in adverse health effect including respiratory cancer, kidney and liver damage [9]. It is for this reason that it is listed as one of the priority hazardous substances in the field of water policy in various countries. Figure 1.2 presents the mechanisms and individuality in chromium toxicity in both humans and plants. In humans, carcinogenesis of chromium has been proposed to proceed via Cr(VI)-induced multistage carcinogenesis, epigenetic modification, and genomic instability [23]. While in plants, the phytotoxicity of Cr involves the inducement of oxidative stress via the induction of lipid peroxidation that causes severe damage to plant's cell membranes [24].

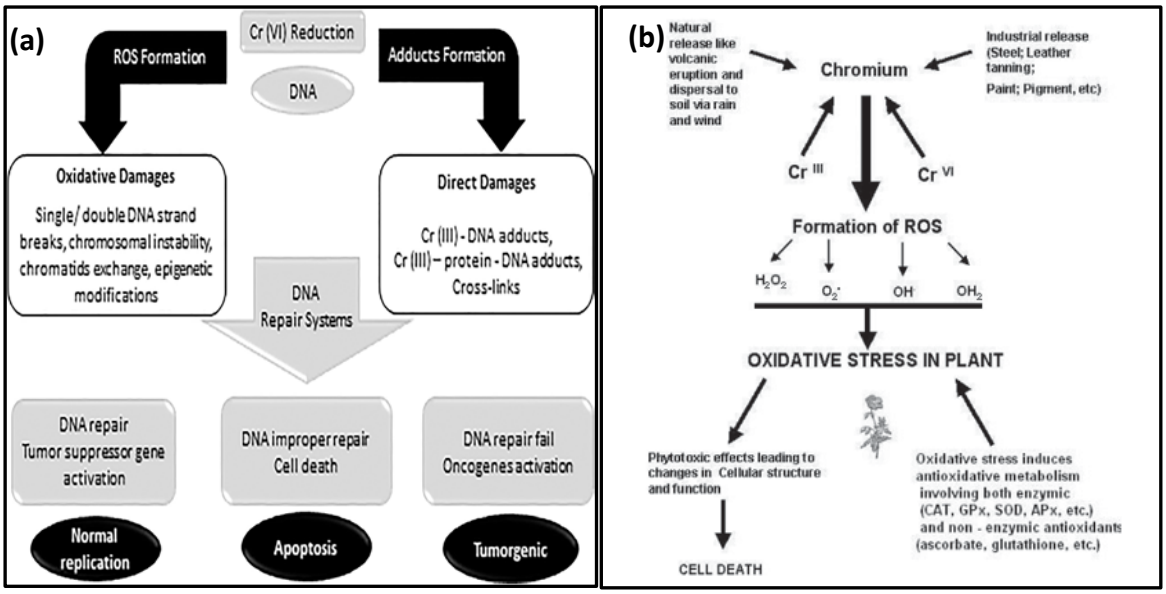

Figure 1. 2: Mechanisms and individuality in chromium toxicity in (a) humans and (b) plants [24].

Therefore, there is a need to look into effective and efficient methods for removal of Cr(VI) in wastewater. Compared to the conventional methods such as membrane separation, electrochemical precipitation, solvent extraction, reverse osmosis, electrocoagulation and adsorption, which require pre-treatment or secondary treatment and produce by-products, photocatalytic reduction has proven to be a more cost effective and efficient method for the removal of Cr(VI) in wastewater [19].

1.3. Aim and Objectives

1.3.1. Aim

The aim of this study is to prepare non-toxic graphitic carbon nitride functionalized with zinc tin oxide (ZTO) nanomaterial for improved efficiency for the removal of Cr(VI) from wastewater.

1.3.2. Objectives

Specific objectives of the study are to:

- synthesize zinc tin oxide (ZTO) nanoparticles,
- characterize the zinc tin oxide nanoparticles using different characterization techniques,
- synthesize and characterize ZTO/graphitic carbon nitride composite,
- evaluate the photocatalytic efficiency of the ZTO mixed metal oxide and ZTO/graphitic carbon nitride nanocomposites.

REFERENCES

1. Halder, J.N. and M.N. Islam, Water pollution and its impact on the human health. Journal of environment and human, 2015. **2**(1): p. 36-46.
2. Kumar Reddy, D. and S. Lee, Water pollution and treatment technologies. J Environ Anal Toxicol, 2012. **2**: p. e103.
3. Fried, J.J., Groundwater pollution. 1975: Elsevier.
4. Liu, D.H. and B.G. Lipták, Groundwater and surface water pollution. 1999: CRC Press.
5. Ferenc, k., geological and industrial coal resources in leading coal producer countries. universitas publishing house petroşani–românia, 2012, 2012. **13**: p. 30.
6. Munawer, M.E., Human health and environmental impacts of coal combustion and post-combustion wastes. Journal of Sustainable Mining, 2018. **17**(2): p. 87-96.
7. Carlson, C.L. and D.C. Adriano, Environmental impacts of coal combustion residues. Journal of Environmental quality, 1993. **22**(2): p. 227-247.
8. Barakat, M., New trends in removing heavy metals from industrial wastewater. Arabian journal of chemistry, 2011. **4**(4): p. 361-377.
9. Babel, S. and T.A. Kurniawan, Cr (VI) removal from synthetic wastewater using coconut shell charcoal and commercial activated carbon modified with oxidizing agents and/or chitosan. Chemosphere, 2004. **54**(7): p. 951-967.
10. Langård, S., Biological and environmental aspects of chromium. Vol. 5. 2013: Elsevier.
11. Qamar, M., M. Gondal, and Z. Yamani, Laser-induced efficient reduction of Cr (VI) catalyzed by ZnO nanoparticles. Journal of hazardous materials, 2011. **187**(1-3): p. 258-263.
12. Jacobs, J.A. and S.M. Testa, Overview of chromium (VI) in the environment: background and history. Chromium (VI) handbook, 2005: p. 1-21.
13. Vaiopoulou, E. and P. Gikas, Regulations for chromium emissions to the aquatic environment in Europe and elsewhere. Chemosphere, 2020. **254**: p. 126876.
14. Elahi, A., et al., Successive use of microorganisms to remove chromium from wastewater. Applied microbiology and biotechnology, 2020. **104**(9): p. 3729-3743.
15. Ajiboye, T.O., O.A. Oyewo, and D.C. Onwudiwe, Conventional and Current Methods of Toxic Metals Removal from Water Using g-C3N4-Based Materials. Journal of Inorganic and Organometallic Polymers and Materials, 2021. **31**(4): p. 1419-1442.

16. Kimbrough, D.E., et al., A critical assessment of chromium in the environment. Critical reviews in environmental science and technology, 1999. **29**(1): p. 1-46.
17. Khan, T.A., et al., Removal of chromium (VI) from aqueous solution using guar gum–nano zinc oxide biocomposite adsorbent. Arabian Journal of Chemistry, 2017. **10**: p. S2388-S2398.
18. Deravanesiyan, M., M. Beheshti, and A. Malekpour, The removal of Cr (III) and Co (II) ions from aqueous solution by two mechanisms using a new sorbent (alumina nanoparticles immobilized zeolite)—Equilibrium, kinetic and thermodynamic studies. Journal of Molecular Liquids, 2015. **209**: p. 246-257.
19. Dakiky, M., et al., Selective adsorption of chromium (VI) in industrial wastewater using low-cost abundantly available adsorbents. Advances in environmental research, 2002. **6**(4): p. 533-540.
20. Karimi-Maleh, H., et al., Recent advances in removal techniques of Cr (VI) toxic ion from aqueous solution: a comprehensive review. Journal of molecular liquids, 2020: p. 115062.
21. Ge, J., et al., Advanced design and synthesis of composite photocatalysts for the remediation of wastewater: A review. Catalysts, 2019. **9**(2): p. 122.
22. Das, A.P. and S. Singh, Occupational health assessment of chromite toxicity among Indian miners. Indian journal of occupational and environmental medicine, 2011. **15**(1): p. 6.
23. Pavesi, T. and J.C. Moreira, Mechanisms and individuality in chromium toxicity in humans. Journal of Applied Toxicology, 2020. **40**(9): p. 1183-1197.
24. Hayat, S., et al., Physiological changes induced by chromium stress in plants: an overview. Protoplasma, 2012. **249**(3): p. 599-611.

CHAPTER 2

2. LITERATURE REVIEW

2.1. The chemistry of chromium

Most transition metals exist under six oxidation states including chromium. Chromium is naturally occurring as chromite ore in oxidation state 3+. The most stable states are 3+ and 2+, while the most common are 3+ and 6+ found in aqueous solution [1]. Thermodynamically, Cr(VI) can only exist in relatively high pH, while Cr(III) can exist in several forms at varied pH levels as demonstrated in figure 2.1 [2]. Due to the solubility of Cr(VI) it is highly mobile and thus finds its way into the environment. It is known for being toxic and resulting in carcinogenic and mutagenic behaviour in humans. Furthermore, it may lead to human organ damage such as liver damage and pulmonary congestion [3]. While trivalent Cr(III) has partial hydroxide solubility, thus resulting in less mobility and less bioavailability. Its biological activity, chemical behaviour and impact on the atmosphere are of great importance. Cr(III) plays a vital role in sugar and fat metabolism [4]. Furthermore, it is an important nutrient, and thus influences a number of metabolism [3], therefore turning waste and harmful material such as Cr(VI) into something useful like Cr(III) is something that needs to be further looked into in order to preserve the environment.

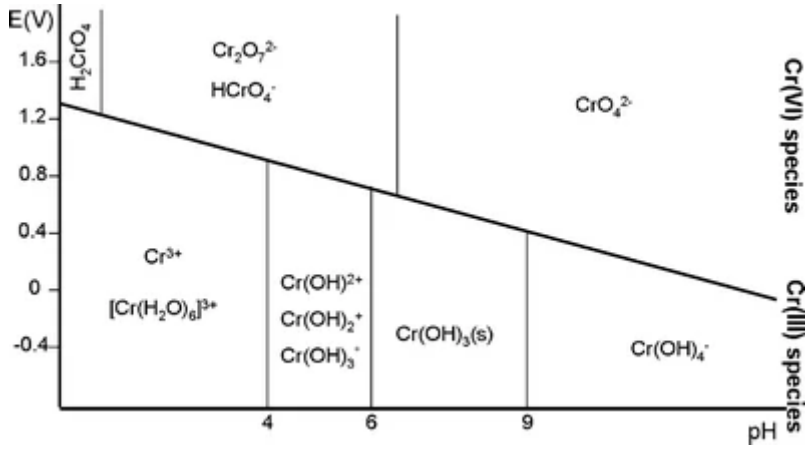

Figure 2. 1:Different chromium oxidation states.

2.2. Zinc stannate: properties and crystal structure

In nanotechnology, there has been a rising interest in research involving specially designed semiconductors with unique properties. Horrocks *et al*, studied zinc stannate as alternative synergist of antimony (III) oxide, due to its unique properties which include non-toxicity,

synergistic activity, flame retardancy and smoke suppressant [5]. Zn_2SnO_4, also called the zinc stannate [6], it is a typical ternary oxide semiconductor and belongs to the class of (II-IV-VI) oxides of the form $A_2^{II}B^{IV}O_4$. Zinc stannate is a transparent *n*-type semiconductor and its band gap is around 3.6 eV, with a low absorption coefficient, and high chemical sensitivity. In addition, it is very stable under extreme conditions (very high temperatures) and possesses high electron mobility and conductivity (~ 10^4 S cm^{-1}) [7]. Furthermore, it exhibits superior optical properties than its binary counterparts, and accounts for its extensive applications in solar cells, lithium batteries, sensors including the degradation of organic pollutants in wastewater [6].

Zinc stannate is found in two dissimilar crystallographic structures: the $ZnSnO_3$, which has an orthorhombic phase and Zn_2SnO_4 of cubic phase. The metastable perovskite ($ZnSnO_3$) form is produced at a temperature ranging from 350 - 750 ºC; and at even higher temperature of about > 750 ºC, it is then transformed to the stable cubic spinel (Zn_2SnO_4) structure [8]. The cubic phase Zn_2SnO_4 is a face-exposed octahedron, while orthorhombic $ZnSnO_3$ is a face-exposed hexahedron structure [9]. The metastable $ZnSnO_3$ has crystal lattice with two cation sites, where the Sn^{4+} is located at the corner, while Zn^{2+} is found in the centre together with the oxygen anion. Furthermore, the structure has strong covalent bonds between zinc and oxygen atoms and is said to be non-centrosymmetric [10].

Several $ZnSnO_3$ structures have been reported with space group (R-3) and lattice parameters a = 5.2835 Å, c = 14.0913 Å. [11-13]. The Zn_2SnO_4 has a cubic structure and its (O^{2-}) anions are organized in a rather cubic lattice with Sn^{2+} and Zn^{2+} cations located at some or all tetrahedral and octahedral sites. The lattice parameter of Zn_2SnO_4 is a = 8.65 Å with space group of Fd3m [6]. The structures of the two zinc stannate phases are shown in Fig. 2.2

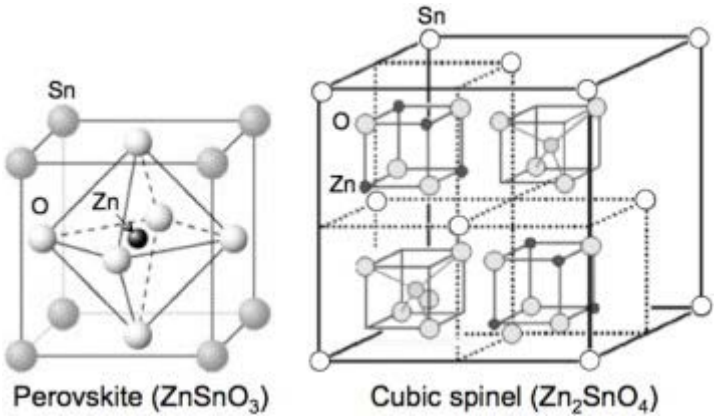

Figure 2. 2: The orthorhombic perovskite phase ($ZnSnO_3$) and cubic spinel (Zn_2SnO_4) structures [6].

Zn_2SnO_4 nanowires showed that the nanoparticles exhibit a blue-green emission at around 400 - 600 nm under UV light, revealing that Zn_2SnO_4 has exceptional potential in the field of photovoltaic devices, photocatalysis, sensors for moisture and combustible gas, transparent electrode as well as lithium batteries [14]. Most reports on the photocatalytic activity of zinc stannate deal with irradiation of UV light because of the optical absorption of zinc stannate, which lies in the UV region. The photocatalytic properties of the different structures of Zn_2SnO_4 have been evaluated using Congo red as a model contaminant [15], and both the shape and morphology of the particles were found to influence the photocatalytic activity. The study found that the influence in photocatalytic activity could be attributed to enhanced oxygen vacancies and crystallite defects formed by substitution of Zn^{+2} in the lattice of SnO_2, revealed in photoluminescence measurements. Other specific applications of zinc stannate are discussed in the following sections.

2.3. Applications of zinc stannate

2.3.1. Gas sensors

Toxic and combustible gas detection can never be over emphasised and plays a significant role in the monitoring of air quality in the environment. Gases such as C_3H_8, NH_3, H_2S, NO_2, CO, NO and H_2, are hazardous to human health, as they are flammable, toxic and explosive. Therefore, the detection of accidental leaks is very crucial as a safety measure for use in industries and household. Studies have reported on the possibility of zinc stannate as a sensing material for ethanol, formaldehyde, triethylamine and combustible gases [16]. Wang *et al* studied the sensing performance of zinc stannate for toluene and compared the sensing performance of different morphologies [17]. The nanosheet assembled Zn_2SnO_4 hierarchical

structure material outperformed many other hierarchical sphere and solid cube like Zn_2SnO_4 material by exhibiting fast speed at 280 ºC after 4 cycles as the sensing materials of gas sensor. Table 2.1 presents the sensing properties and performance of different zinc stannate based compounds on different target gases.

Table 2. 1: Zinc stannate based sensors [30].

No	Sensing material	Target gas	Conc. of gas	Operating temp.	% Sensor response	Response Time	Recovery Time	Refs.
1	Hallow $ZnSnO_3$ nanocubes	Ethanol	200 ppm	270 ºC	22.5	<2s	<30s	[18]
2	$ZnSnO_3$ nanocages	Ethanol	10 ppm	270 ºC	3.1	<2s	<30s	[19]
3	$ZnSnO_3$ nanocages	H_2S	50 ppm	310 ºC	17.6	<20s	<20s	[20]
4	$ZnSnO_3$-SnO_2	Ethanol	100 ppm	270 ºC	27.8	<1s	<1.8s	[21]
5	Hallow $ZnSnO_3$	Butane	500 ppm	380 ºC	5.79	0.3s	0.65s	[22]
6	$ZnSnO_3$ nanowires	Ethanol	500 ppm	300 ºC	42	1s	1s	[23]
7	Zinc stannate	H_2	50 ppm	375 ºC	652.36	1s	12s	[24]
8	$ZnSnO_3$ microparticles	H_2S	5.5 V	4.5 V	40.3	30s	100s	[8]
9	SnO_2/$ZnSnO_3$ nanostructures	Ethanol	100 ppm	275 ºC	36.5	3s	30s	[25]
10	$ZnSnO_3$ Hollow fibres	Ethanol	2000 ppm	300 ºC	74	<10s	<10s	[26]
11	$ZnSnO_3$	HCHO	100 ppm	300 ºC	36.81	3s	12s	[27]
12	Hallow octahedral Zn_2SnO_4	H_2S	50 ppm	260 ºC	46.0	10s	25s	[28]
13	Zn_2SnO_4 microcubes	LPG	3000 ppm	250 ºC	63	-	-	[29]
14	Hierarchical zinc stannate	LPG	5000 ppm	25 ºC	143	180s	240s	[30]

2.3.2. Lithium batteries

Automobile electrical systems and portable devices that require the use of rechargeable batteries have increased over the years [31]. Lithium ion batteries (LIBs) have many advantages ranging from long cycle life, minute memory effect and high energy density [32]. Due to the lithium activity in Sn and Zn, Zn_2SnO_4 has been utilised as appropriate anode material for Li ion batteries. This gives it an advantage of capacity retention compared to other compounds, such as sodium, magnesium, zinc and aluminium [32]. However, more work needs to be done to the electrode life cycle for improved practical use [33].

2.3.3. Transparent electrodes

Zinc stannate has fascinated researchers as new transparent conducting oxides materials. It has an advantage that their film properties could be tuned to have exceptional thermal

stability and mechanical strength [34]. Ko. *et al*., studied the Zn_2SnO_4 thin films prepared by combinatorial approach and concluded that they exhibited good stability against high temperature oxidation [34]. Zn_2SnO_4 have been used as electron conductors to prepare dye-sensitized solar cells. The Zn_2SnO_4 demonstrated the possible practical use in dye sensitized solar cells (DSSC) with additional development in the use of dyes with higher LUMO position [35].

2.3.4. Photovoltaic devices

In photovoltaics, two semiconductors could be combined to form a composite electrode in order to augment each other. Electrodes composed of two metal oxides such as Zn_2SnO_4-SnO_2 and ZnO-Zn_2SnO_4 have been applied in sensitized solar cells for the enhancement of the photovoltaic performance [36]. Oxide/Zn_2SnO_4 composites were used to study the effect of energy level matching on the enhancement of photovoltaic response by Liu, *et al*. [37]. The use of ZTO as photovoltaic device is still an ongoing study, which is believed to highlight many potential areas of application.

2.3.5. Photocatalysis

Numerous studies have reported on the application of zinc stannate as a photocatalyst [38-40]. Studies have been expanded further to investigate more zinc stannate based materials such as its composite with other compounds, and how different combinations enhance its application in the field of photocatalysis [41, 42]. The effect of different morphologies of ZTO on their photocatalytic efficiency has also been investigated. Recently Pandimurugan and Sankaranarayanan, prepared Zn_2SnO_4 using the microwave assisted method and studied

its photocatalytic as well as antibacterial activity [43]. One of the factors that have pronounced effect on the properties of ZTO is the method of synthesis, and different routes have been reported for the synthesis of ZTO, which will be discussed next.

2.4. Synthesis methods of zinc stannate

Methods for synthesising Zn_2SnO_4 have been advancing over the years, as more and improved methods continue to be reported. These include, high temperature solid state reaction, co-precipitation, electrospinning, chemical bath deposition, sol gel synthesis and hydrothermal method. These methods will be discussed in more detail.

2.4.1. High temperature solid state reaction

This reaction is a process involving mechanical activation by grinding and calcination at high temperature. It is used widely for processing of powders in order to modify the properties (physical and chemical) of the materials [44]. Changes that occur in the process of grinding and high temperature calcination largely influence the final product and its specific application[45]. There are four stages involved in the process of mechanical activation by grinding which are, material obliteration, construction of new surface, fine grinding and conversion of new material with different structure [45]. Song *et al*., studied the optical properties of ceramics obtained by grinding ZnO and SnO_2 powders mechanically activated at different times [46]. The effect of grinding on the synthesis of Zn_2SnO_4 was studied by Nikolić, *et al*., and found that the grading had a decreasing effect on the specific surface area of the zinc stannate obtained [44].

2.4.2. Co-precipitation

Co-precipitation is a two-step method; the first step involves the addition of the precipitator to the metal salt in order to get the precursor of the desired product and the second step is where the desired sample is finally obtained through heat treatment. The following expression is used for the synthetic process of Zn_2SnO_4: [47]

$$2Zn^{2+} + Sn^{4+} + 6OH^{-}\ (pH = 7) \longrightarrow 2ZnSn(OH)_2 \downarrow + Sn(OH)_4 \downarrow \longrightarrow Zn_2SnO_4 \qquad (2.1)$$

Babar *et al*., studied the effect caused by sintering temperature on the properties of the Zn_2SnO_4 sample prepared by co-precipitation method [48]. The study revealed that samples sintered at 400–1200 °C showed combined phases viz. ZnO, SnO_2, Zn_2SnO_4. Furthermore

this method was also used to prepare ZTO, which was applied as gas sensor and displayed exceptional gas sensing properties towards ethanol gas at low operating temperature [39].

2.4.3. Electrospinning

Researchers have paid much attention to electrospinning due to its facile technique of transforming solutions into continuous fibre. Electrospinning is an adaptable technique which uses high electrostatic forces. Its set-up is based on the following: direct current power supply, syringe for electrospun solution, metallic needle and conductive collector as shown in Fig 2.3 [49]. The easy synthesis of Zn_2SnO_4 nanofibers by phase separation of inorganic precursor and polymers, through electrospinning coupled with calcination has been established [7]. Several studies have reported on the synthesis of ZTO nanofiber through electrospinning [17, 50-52]. Furthermore, porous ternary heterojunction nanofibers have been prepared by electrospinning technique, such as ZnO-SnO_2-Zn_2SnO_4 [53].

2.4.4. Chemical bath deposition

This technique involves the hydrolysis of metal ions in solution, and the control of heterogeneous precipitation on a substrate at relative low temperatures (up to 100 °C). This minimal environmental impact process has advantages of minimal cost and simplicity, low deposition temperature and capability of achieving large area coating [54]. It is a field of research in the nanostructure thin films which is fast emerging. The treatment of zinc tin oxide precursor solutions with chemical-bath deposition method was done to enhance the performance of dye-sensitized Zn_2SnO_4 solar cells by Chen. *et al*. [55]. They reported that the films grown from chemical bath deposition showed a limitation in thickness due to the phenomenon of solution supersaturation. However, this could be solved by carrying out the synthesis process in a number of runs [56].

2.4.5. Sol gel synthesis

This process is an exceptional method for forming compositions. It gives room for control or manipulation of the stoichiometry and homogeneity of the prepared material, with the advantage of procuring fine grains and using low temperatures [57]. Ma *et al*., studied the synthesis of Zn_2SnO_4 and its dielectric properties using sol gel method [58]. The study revealed that the inverse-spinel Zn_2SnO_4 ceramics (containing 1 wt% B_2O_3) sintered at 975 °C exhibited good microwave dielectric properties: ε_r=9.3, $Q\times f$=62,000 GHz and τ_f=−50 ppm/°C. Furthermore Zn_2SnO_4 ceramics with low sintering temperatures are promising candidate materials for low-temperature cofired millimeter-wave devices. Recent

work has been done to investigate how annealing temperature could also affect the structural property of Zn_2SnO_4 [59].

2.4.6. Hydrothermal method

Many researchers have fabricated ZTO nanoparticles via the hydrothermal route [60, 61]. Hydrothermal method is well known as an efficient way of synthesising highly crystallized and phase-pure Zn_2SnO_4 nanoparticles which has proven to be difficult to attain using high-temperature solid reactions due to ease of ZnO to evaporate [62]. Fu *et al*., reported that the synthesis of ZTO in the hydrothermal method goes through many intermediate phases during the ZTO nucleation [63]. With increase in the reaction time, $ZnSn(OH)_6$ combines with ZnO, thus forming Zn_2SnO_4 structures. The method is suitable for large quantity production of high-quality Zn_2SnO_4 nanoparticles [9, 64]. Even though there are a number of methods to synthesise ZTO, the hydrothermal method has proven to be more versatile than the rest because of its ease of operation, minimal cost, efficient mass production and ecological friendliness. It is considered to be a green process because the nucleation and growth take place in aqueous medium and under mild conditions.

Additionally, the hydrothermal method has been reported to be the best technique since it produces pure fine oxide in bulk scales [9]. Studies showed that factors such as concentration of alkaline, time of reaction and temperature alter the morphology, size and crystallinity, thus influencing its performance [14]. ZTO could be used in its pure form or combined with semiconductors to form either composites or heterojunctions with the right band gap energy alignment. Example of such semiconductor is graphitic carbon nitride.

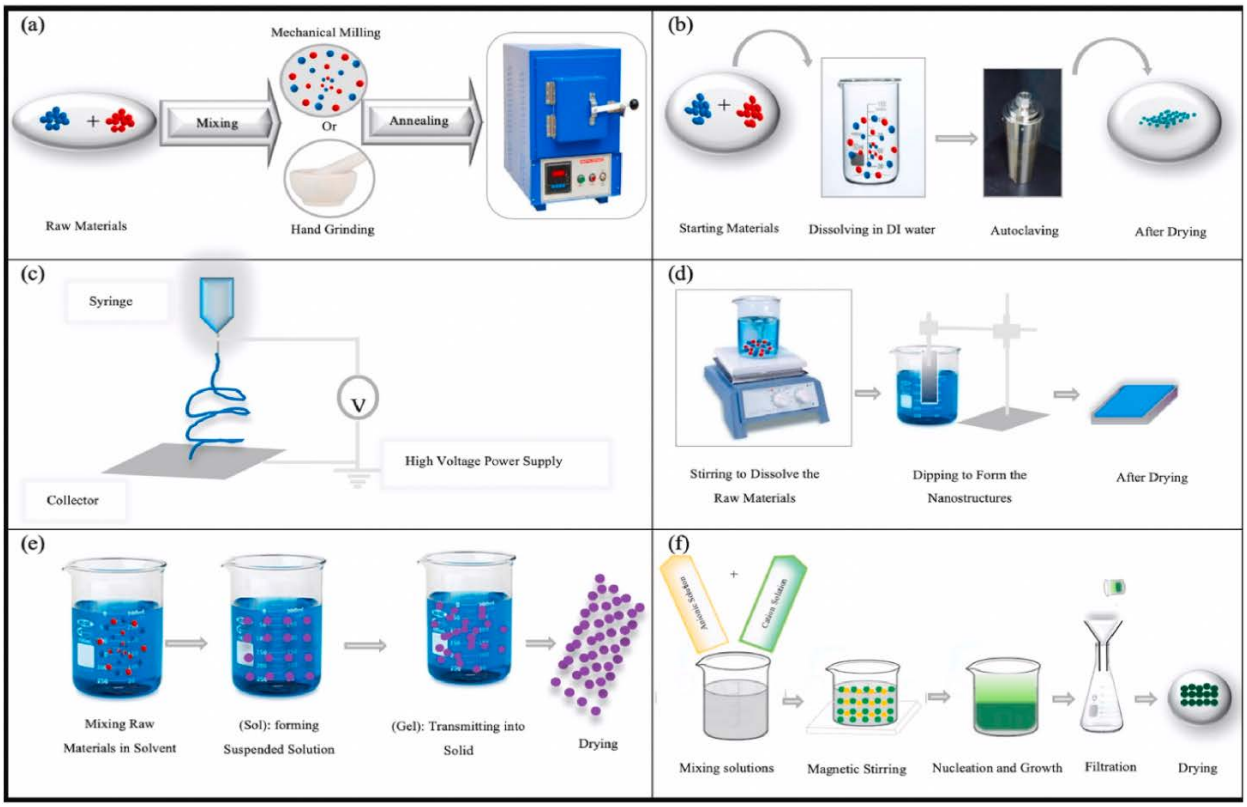

Figure 2. 3: Schematic diagrams of the different synthetic routes: (a) solid state reaction, (b) hydrothermal synthesis, (c) electrospinning, (d) chemical bath deposition , (e) sol-gel and (f) co-precipitation synthesis method [49].

2.5. Graphitic carbon nitride: properties and crystal structure

Graphitic carbon nitride is a polymeric semiconductor that consists of two units, tri-s-triazine (C_6N_7) and s-triazine (C_3N_3), as shown in Fig 2.4. The structure consists of carbon, nitrogen, with a minute amount of hydrogen impurity. Tri-s-triazine is known to be more stable than s-triazine under ambient conditions [65]. Hybridization of carbon and nitrogen atoms results in p-conjugated graphitic planes of g-C_3N_4.

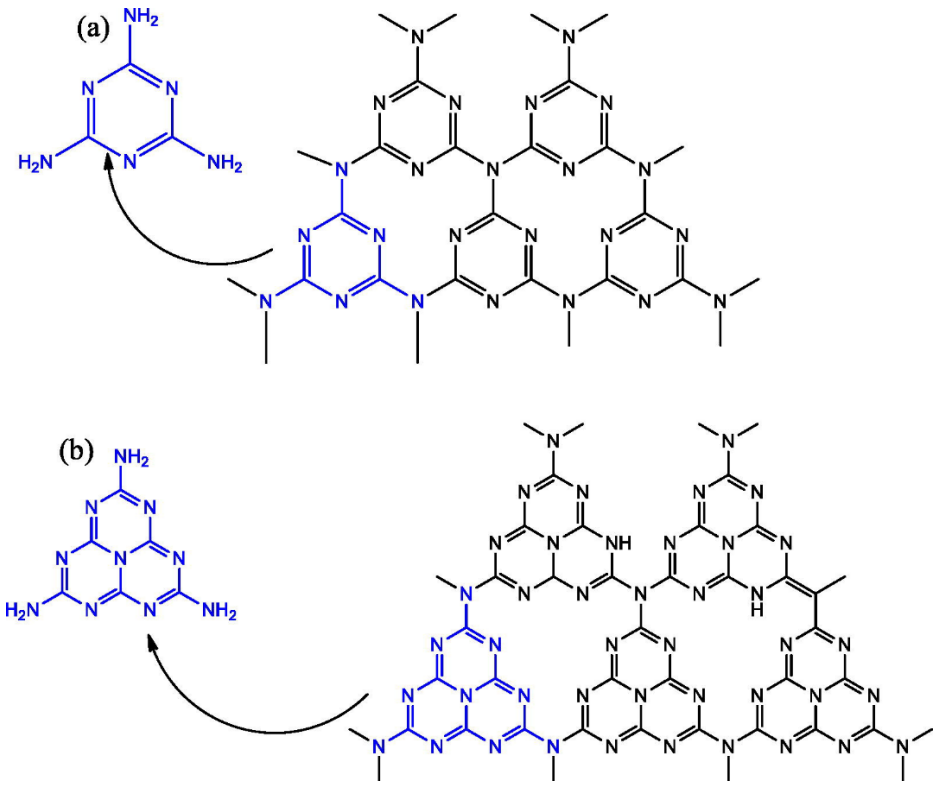

Figure 2. 4: Structures of g-C_3N_4; (a) s-triazine and (b) tri-s-triazine [65]

This material has a band gap of about 2.7 eV as shown in Fig 2.5, suggesting that it is capable of emitting light in the visible region at approximately 400 - 475 nm. Luminescent g-C_3N_4 has shown excellent optical properties, including adjustable emission wavelength, no light scintillation and a stable fluorescence signal. Graphitic carbon nitride has been utilized in gas sensing due to its exceptional advantages such as, ease of preparation, huge surface area, minimal toxicity, and high stability. The greatest merit of g-C_3N_4 is that it is metal free, as most photocatalyst contain metals which can prove to be environmentally toxic and cause unnecessary damage. Furthermore, they have good biocompatibility and low biotoxicity since their composition consists of pure carbon and nitrogen, thus becoming of high interest in carbon nanomaterial research.

When the surface of g-C_3N_4 is modified or doped with other material the fluorescence emission quantum yield is comparable to the high-performance semiconductor quantum dots, but at the same time safer as it does not affect the action of the biomolecules. Another advantage of g-C_3N_4 over some nanomaterials is that the properties of the functional group could be used to control their solubility, photoelectric properties and compatibility with a number of interfaces through its adjustment [66]. Furthermore, its surface area could be enhanced through techniques such as preparation of mesoporous g-C_3N_4. Its enhanced

photocatalytic activity has been reported to be related to the favourable structure, which are the result of different heat-treatment temperatures [67].

There are 5 structural types of g-C_3N_4, which are the cubic phase, α-phase, β-phase, quasi-cubic phase and graphitic-like phase. These materials have characteristic hardness that is comparable to that of diamond, except for graphitic-like phase. Although, the graphitic phase is not as hard as diamond, it has comparable chemical stability which makes it highly valued [66].

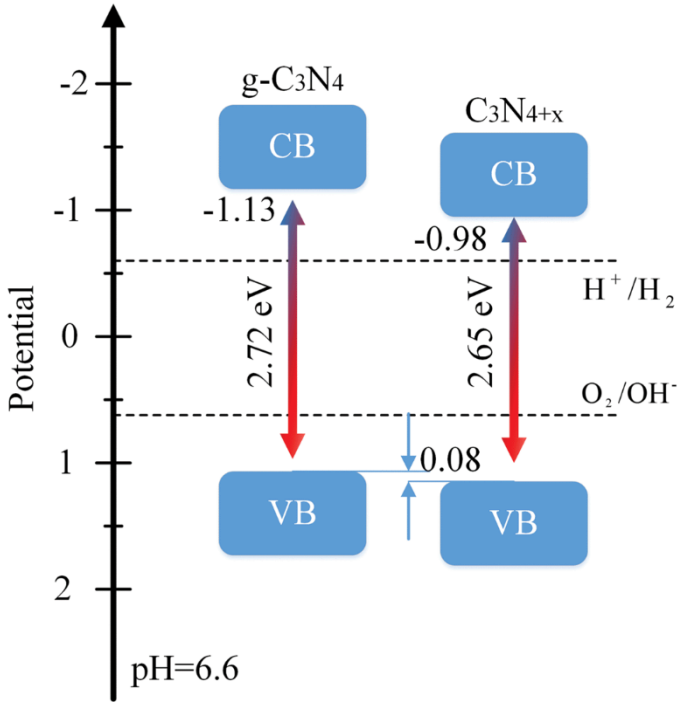

Figure 2. 5: Schematic energy band diagram of g-C_3N_4 [68].

The biodegradability and sustainability of g-C_3N_4, in addition to its tuneable narrow band gap have been applied in a number of fields such as sensing, solar cells, photocatalysis and energy storage [65]. Due to its ability to harvest solar energy, g-C_3N_4 is capable of being used as a photocatalyst and its use in different areas of photocatalysis has been extensively reported. One of the first possible use of g-C_3N_4 as a photocatalyst was reported by Wang *et al*., after which the research on g-C_3N_4 as photocatalyst expanded [69].

2.6. Synthesis methods of graphitic carbon nitride

Graphitic carbon nitride is commonly prepared by thermal polymerization, hot solvent, template-directed solid-state, soft-templating synthesis, and sonochemical methods. Its general synthesis is by the thermal condensation of nitrogen-rich precursors such as

melamine, cyanamide, urea, dicyandiamide or thiourea, which result in a graphene-like structure as shown in Fig 2.6 **[70]**.

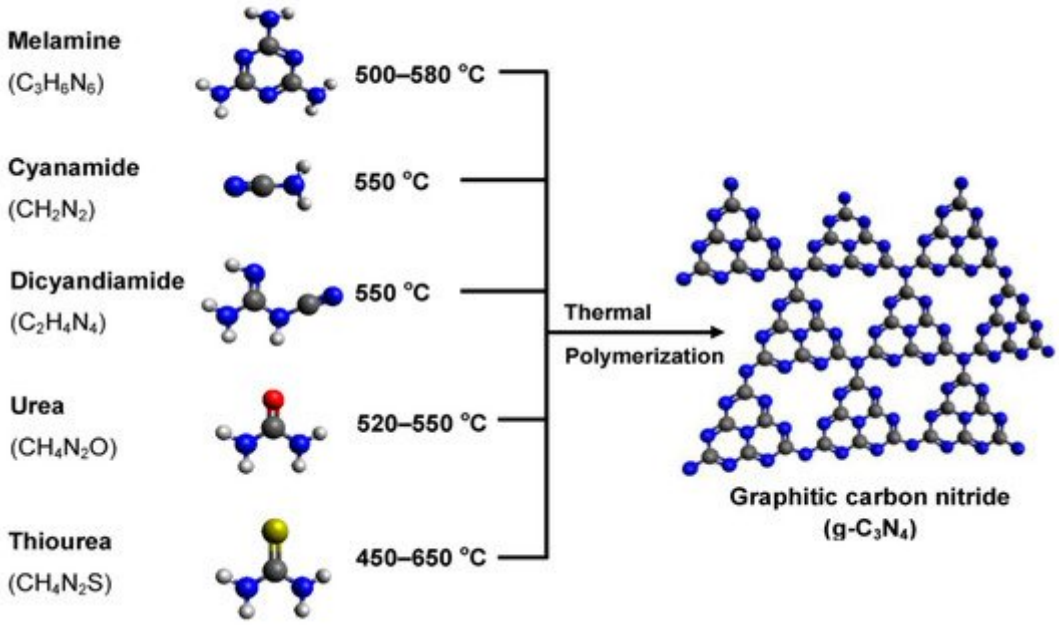

Figure 2. 6: Schematic illustration of the synthesis process of g-C_3N_4 [70].

During the synthesis reaction there is a constant loss of ammonia by urea to form melamine, followed by melem and melon then finally g- C_3N_4 thorough thermal polymerization [71]. The 2D extended graphite-like sheets of g-C_3N_4 shown in Fig 2.7 are formed by triazine rings (C_3N_3) which become linked via nitrido nitrogen atoms [72]. There are two ways in which the synthesis can be conducted, under inert conditions or in air. In both cases no significant change is seen in the bulk structure, however, the variation may lead to difference in degree of condensation, yield and surface property change [73].

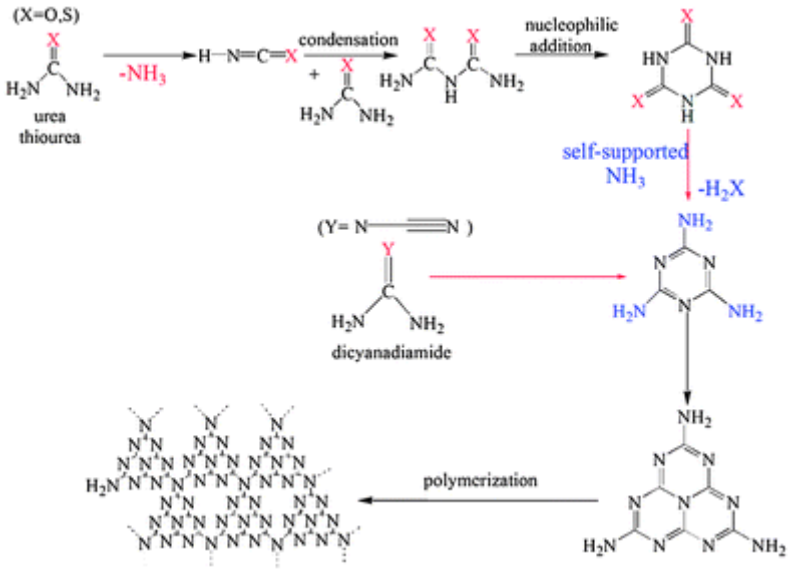

Figure 2. 7: Possible mechanism reaction paths of polymeric carbon nitride [74]

2.7. Photocatalysis

Photocatalysis is the process of a chemical reaction that takes place in the presence of light as well as a photocatalyst. It has quite several applications like antibacterial, antifogging, air purifying, deodorizing including water purification. Water is a necessity for all living organisms. Due to the ever-increasing population, there is also an increase in supply demand, creating a serious need for advanced, efficient and effective ways for wastewater treatment. Many processes have been employed in wastewater treatment but photocatalysis seems to have attracted more attention to researchers due to its green chemical pathway [96]. It is a phenomenon, in which an electron-hole pair is generated on exposure of a semiconducting material to light [97]. Firstly, the reactants are absorbed by the catalyst then the catalyst again absorbs photons, which consequently results in the creation of electrons and holes that are responsible for redox reactions [75].

2.7.1. Mechanism of photocatalysis

A Photocatalytic reaction is dependent on light energy and the catalyst. Semiconductors are used as catalysts that work as sensitizers for light inspired redox process. This is because of their electronic structure with a filled valence band and an unoccupied conduction band [76]. Figure 2.8 shows the schematic illustration of a semiconductor photocatalytic mechanism.

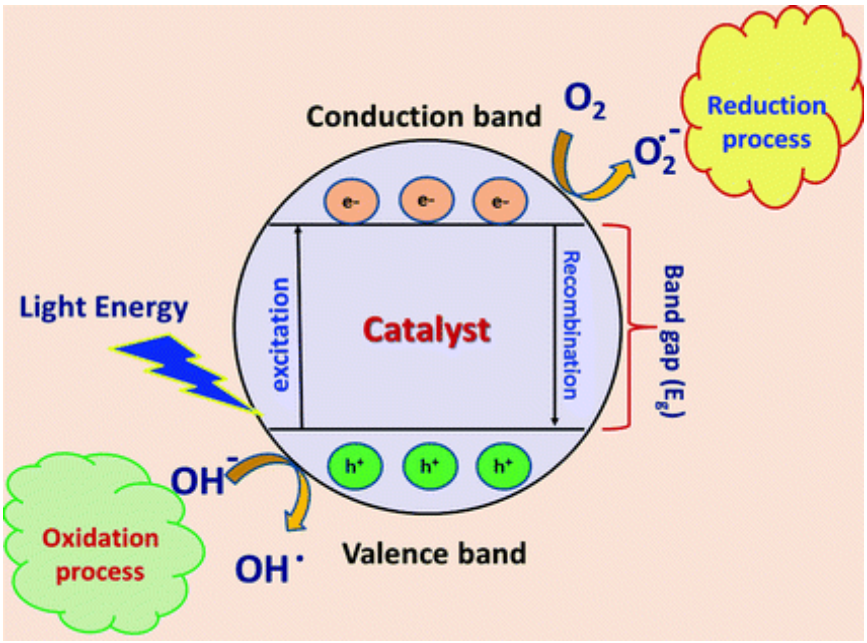

Figure 2. 8: Schematic illustration of semiconductor photocatalytic mechanism [76].

During the process of photocatalysis, a semiconductor material is irradiated with light whose energy is higher than or equals that of the band gap energy of the material. This results in the absorption of photon and subsequent excitation of electrons from the valence to the conduction band, leading to the equal generation of a hole in the valence band as illustrated in Fig 2.8. The excess energy that is dissipated through non-radiative mechanism is as a result of electron-hole recombination. Secondary reaction is initiated by migration of charge carriers to the surface of the catalyst. The holes oxidize molecules and subsequently react with water molecules to produce hydroxyl radicals as shown in equation (2.5) which then react with the organic pollutants in equation (2.9) [77, 78].

photocatalyst (CBM) + Cr(VI) → photocatalyst (2.2)

photocatalyst + hν → catalyst ($e^- + h^+$) (2.3)

$O_2 + e^- \rightarrow O_2^{\bullet-}$ (2.4)

$2O_2^{\bullet-} + 2H_2O \rightarrow H_2O_2 + 2OH^- + O_2$ (2.5)

$H_2O_2 + e^- \rightarrow {}^\bullet OH + OH^-$ (2.6)

$O_2^{\bullet-}$ + Cr(VI) → non-toxic or less-toxic products (2.7)

h^+ + Cr(VI) → non-toxic or less-toxic products (2.8)

•OH + Cr(VI) → non-toxic or less-toxic products (2.9)

2.7.2. Advantages of photocatalysis

Photocatalysis is characterized by exclusive class of chemical modifications [79]. It employs energy from light then uses it to drive reactions that are difficult. It is a promising and efficient solution to the storage of large scale solar energy [79]. Photocatalysis has overcome severe demands of modern chemistry by being an ecologically friendly and energy-sustainable substitute to previous tools [80]. Other important factors that render photocatalysis an advantageous process over other processes are its ease of recovery and salvage, and higher degradation efficiency which all contribute to the reduction of treatment cost [81].

2.8. Heterojunction systems

Semiconductor-based photocatalysis have attracted researchers due to its ability to directly use solar energy for manufacture of solar fuels, like hydrogen and hydrocarbon fuels and for degradation of different pollutants. However, the efficacy of photocatalytic reactions continues to be low due to the fast electron–hole recombination and low light utilization. Consequently, immense attempts have been explored to solve these problems. Like other photo-induced processes, the efficiency of photocatalysis is reduced by recombination processes. Heterojunction photocatalysts have shown to possess higher photocatalytic activity due to the spatial separation of photogenerated electron–hole pairs. This could be addressed by the combination of two or more semiconductors of compatible band structure to form a heterojunction system with the right band alignment [82].

Heterojunctions may be of type I, type II and even type III band alignment as shown in Fig 2.9.

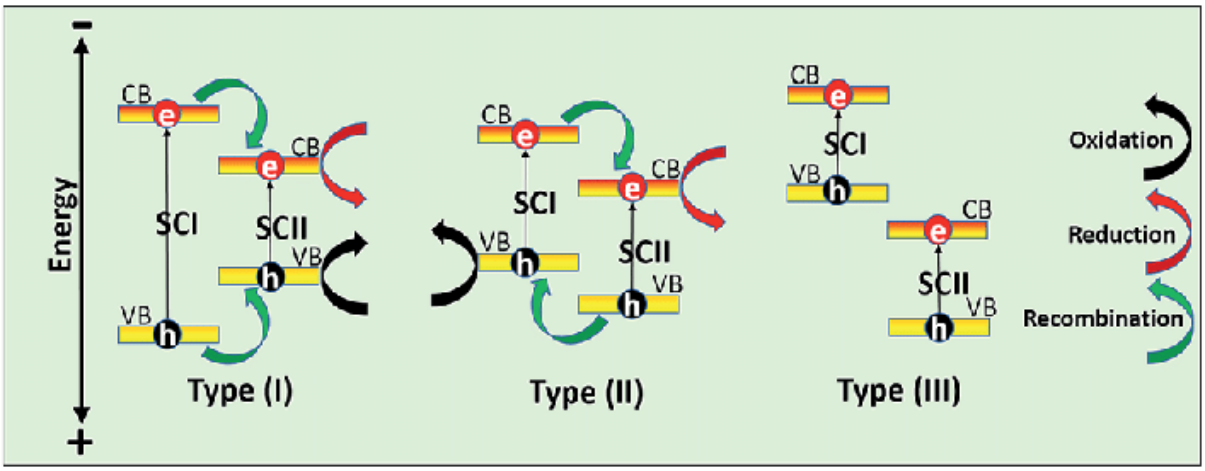

Figure 2. 9: Schematic illustration of the coupling of two semiconductors to form type I, type II, and type III heterojunctions [83].

In Type I band alignment, also known as the 'Straddling' band pattern, a semiconductor with smaller band gap relies on the one with larger band gap and there is an overlap between them. In this type of heterojunction, the VB of semiconductor 1(SCI) is more +ve than VB of SCII, also the CB of SCI is more negative than CB of SCII. Consequently, electrons move from CB of SCI to CB of SCII and holes from VB of SCI to VB of SCII. [84]. Upon sufficient reduction potential by the conduction band minimum, the holes turn to get scavenged by water and becomes oxidized to molecular oxygen and protons, when the valence band minimum lies at the potential ≥ 0.83 V. This results in a semiconductor of bandgap $\leq 2{,}29$ which cannot produce simultaneously superoxide radicals and hydroxyl radicals. Furthermore, a photocatalyst of bandgap ≤ 1.16eV also needs the aid of scavenger in order to drive oxidation-reduction reactions [85]. Latest research has shown to have combated those shortcoming and have since been able to form laddered type 1 heterojunction, which harvest full-solar spectrum in scavenger free photocatalysis [86]

In type II band alignment, also called 'Staggered' band pattern, the CB of SCII is more negative than that of SCI while the VB of SCII is less positive than the VB of SCI. Hence, there is a transfer of photogenerated charge carriers from CB of SCII to the CB of SCI with simultaneous transfer of holes from the VB of SCI to VB of SCII that leads to an efficient charge separation in the course of photocatalytic process. Many semiconductor photocatalyst have shown to have a seriously problem of electron recombination, hence much focus has been to design photocatalyst which can reduce or combat the fast electron recombination issue. Zeng *et al*, have recently constructed a novel SiH/CeO_2(111) type-II heterojunction

with a very small lattice mismatch of less than 1%, with great stability and easy of synthesis. Due to the van der Waals interaction between SiH and CeO_2(111) components, electron and hole accumulation regions form at the heterojunction interface, this has been seen to be very much effective and favourable to the separation of photoexcited electron–hole pairs [87].

Finally, in type III, also referred to as 'Broken gap" pattern, the arrangements of band positions display broken up situations [88]. The bandgaps of the two two photocatalysts are completely separated. Therefore, photoinduced carrier separation and migration barely occur between the two phases, hence efficiency of the photocatalytic reactions is therefore not improved [89].

Both ZTO and g-C_3N_4 have wide bandgaps, so forming a heterojunction using the two semiconductors results in a narrow bandgap. Furthermore, since the ZTO is an n-type semiconductor while g-C_3N_4 is a p-type semiconductor, incorporating the ZTO into g-C_3N_4 will result in the construction of a p-n heterojunction of the type II band alignment, thereby enhancing its photolytic activity as compared to the pristine g-C_3N_4 or ZTO. This type of system would have enhanced photocatalytic activity due to the reduction of the recombination processes, and would be effective in addressing some environmental challenges such as the photoreduction of Cr(VI) to Cr(III).

REFERENCES

1. Shupack, S.I., The chemistry of chromium and some resulting analytical problems. Environmental Health Perspectives, 1991. **92**: p. 7-11.
2. Unceta, N., et al., Chromium speciation in solid matrices and regulation: a review. Analytical and Bioanalytical Chemistry, 2010. **397**(3): p. 1097-1111.
3. Bulut, V., et al., Speciation of Cr (III) and Cr (VI) after column solid phase extraction on Amberlite XAD-2010. Journal of hazardous materials, 2007. **143**(1-2): p. 112-117.
4. Miretzky, P. and A.F. Cirelli, Cr (VI) and Cr (III) removal from aqueous solution by raw and modified lignocellulosic materials: a review. Journal of hazardous materials, 2010. **180**(1-3): p. 1-19.
5. Horrocks, A., et al., Zinc stannates as alternative synergists in selected flame retardant systems. Journal of fire sciences, 2009. **27**(5): p. 495-521.
6. Baruah, S. and J. Dutta, Zinc stannate nanostructures: hydrothermal synthesis. Science & Technology of Advanced Materials, 2011. **12**(1): p. 1-N.PAG.
7. Sun, S. and S. Liang, Morphological zinc stannate: synthesis, fundamental properties and applications. Journal of Materials Chemistry A, 2017. **5**(39): p. 20534-20560.
8. Xu, J., et al., One-step hydrothermal synthesis and gas sensing property of ZnSnO3 microparticles. Solid-State Electronics, 2006. **50**(3): p. 504-507.
9. Miyauchi, M., et al., Single crystalline zinc stannate nanoparticles for efficient photo-electrochemical devices. Chemical communications, 2010. **46**(9): p. 1529-1531.
10. Tangcharoen, T., C. Kongmark, and W. Pecharapa, Synchrotron X-ray absorption spectroscopy study of the local atomic structures and cation ordering in perovskite- and spinel-type zinc stannate synthesized by co-precipitation method. Journal of Molecular Structure, 2015. **1102**: p. 95-100.
11. Kovacheva, D. and K. Petrov, Preparation of crystalline ZnSnO3 from Li2SnO3 by low-temperature ion exchange. Solid State Ionics, 1998. **109**(3-4): p. 327-332.
12. Gou, H., et al., Energetic stability, structural transition, and thermodynamic properties of ZnSnO 3. Applied Physics Letters, 2011. **98**(9): p. 091914.
13. Lo, M.-K., S.-Y. Lee, and K.-S. Chang, Study of ZnSnO3-nanowire piezophotocatalyst using two-step hydrothermal synthesis. The Journal of Physical Chemistry C, 2015. **119**(9): p. 5218-5224.

14. Jaculine, M.M., C.J. Raj, and S.J. Das, Hydrothermal synthesis of highly crystalline Zn2SnO4 nanoflowers and their optical properties. Journal of alloys and compounds, 2013. **577**: p. 131-137.
15. Firooz, A.A., et al., High photocatalytic activity of Zn2SnO4 among various nanostructures of Zn2xSn1− xO2 prepared by a hydrothermal method. Chemical engineering journal, 2010. **165**(2): p. 735-739.
16. Nikolic, M.V. An overview of oxide materials for gas sensors. in 2020 23rd International Symposium on Design and Diagnostics of Electronic Circuits & Systems (DDECS). 2020. IEEE.
17. Wang, L., et al., Comparison of toluene sensing performances of zinc stannate with different morphology-based gas sensors. Sensors and Actuators B: Chemical, 2016. **227**: p. 448-455.
18. Zeng, Y., et al., Synthesis and gas-sensing properties of ZnSnO3 cubic nanocages and nanoskeletons. Sensors and Actuators B: Chemical, 2009. **143**(1): p. 449-453.
19. Zeng, Y., et al., One-pot synthesis and gas-sensing properties of hierarchical ZnSnO3 nanocages. The Journal of Physical Chemistry C, 2009. **113**(44): p. 19000-19004.
20. Zeng, Y., et al., Rapid and selective H2S detection of hierarchical ZnSnO3 nanocages. Sensors and Actuators B: Chemical, 2011. **159**(1): p. 245-250.
21. Yi, Z., et al., Self-assembly of hierarchical ZnSnO3-SnO2 nanoflakes and their gas sensing properties. Transactions of Nonferrous Metals Society of China, 2012. **22**(10): p. 2451-2458.
22. Fan, H., et al., Hydrothermal synthesis of hollow ZnSnO3 microspheres and sensing properties toward butane. Sensors and Actuators B: Chemical, 2011. **153**(1): p. 170-175.
23. Xue, X., et al., Synthesis and ethanol sensing properties of ZnSnO 3 nanowires. Applied Physics Letters, 2005. **86**(23): p. 233101.
24. Wadkar, P., D. Bauskar, and P. Patil, High performance H2 sensor based on ZnSnO3 cubic crystallites synthesized by a hydrothermal method. Talanta, 2013. **105**: p. 327-332.
25. Sun, P., et al., Synthesis of novel SnO2/ZnSnO3 core–shell microspheres and their gas sensing properities. Sensors and Actuators B: Chemical, 2011. **155**(2): p. 606-611.

26. Song, P., Q. Wang, and Z. Yang, Biomorphic synthesis of ZnSnO3 hollow fibers for gas sensing application. Sensors and Actuators B: Chemical, 2011. **156**(2): p. 983-989.
27. Huang, J., et al., Size-controlled synthesis of porous ZnSnO3 cubes and their gas-sensing and photocatalysis properties. Sensors and Actuators B: Chemical, 2012. **171**: p. 572-579.
28. Ma, G., et al., Phase-controlled synthesis and gas-sensing properties of zinc stannate (ZnSnO 3 and Zn 2 SnO 4) faceted solid and hollow microcrystals. CrystEngComm, 2012. **14**(6): p. 2172-2179.
29. Sivapunniyam, A., et al., High-performance liquefied petroleum gas sensing based on nanostructures of zinc oxide and zinc stannate. Sensors and Actuators B: Chemical, 2011. **157**(1): p. 232-239.
30. Singh, S., et al., Fabrication of self-assembled hierarchical flowerlike zinc stannate thin film and its application as liquefied petroleum gas sensor. Sensors and Actuators B: Chemical, 2014. **205**: p. 102-110.
31. Scrosati, B. and J. Garche, Lithium batteries: Status, prospects and future. Journal of power sources, 2010. **195**(9): p. 2419-2430.
32. Hou, X., et al., Preparation and electrochemical characterization of Zn2SnO4 as anode materials for lithium ion batteries. Solid State Ionics, 2010. **181**(13-14): p. 631-634.
33. Zhu, X., et al., Synthesis and performance of Zn2SnO4 as anode materials for lithium ion batteries by hydrothermal method. Journal of Power Sources, 2009. **189**(1): p. 828-831.
34. Ko, J., et al., Transparent and conducting Zn-Sn-O thin films prepared by combinatorial approach. Applied surface science, 2007. **253**(18): p. 7398-7403.
35. Lana-Villarreal, T., G. Boschloo, and A. Hagfeldt, Nanostructured zinc stannate as semiconductor working electrodes for dye-sensitized solar cells. The Journal of Physical Chemistry C, 2007. **111**(14): p. 5549-5556.
36. Li, W., et al., Improvement of photovoltaic performance of perovskite solar cells with a ZnO/Zn2SnO4 composite compact layer. Solar Energy Materials and Solar Cells, 2017. **159**: p. 143-150.
37. Liu, X.-Y., et al., Effect of energy level matching on the enhancement of photovoltaic response about oxide/Zn2SnO4 composites. Journal of Materials Chemistry, 2011. **21**(12): p. 4108-4116.

38. Foletto, E.L., et al., Application of Zn2SnO4 photocatalyst prepared by microwave-assisted hydrothermal route in the degradation of organic pollutant under sunlight. Ceramics International, 2013. **39**(4): p. 4569-4574.
39. An, D., et al., Synthesis of Zn2SnO4 via a co-precipitation method and its gas-sensing property toward ethanol. Sensors and Actuators B: Chemical, 2015. **213**: p. 155-163.
40. Ayesha, B., et al., Synthesis of zinc stannate nanoparticles by sol-gel method for photocatalysis of commercial dyes. Results in Chemistry, 2020. **2**: p. 100023.
41. Lei, D., et al., 3D/2D direct Z-scheme photocatalyst Zn2SnO4/CdS for simultaneous removal of Cr (VI) and organic pollutant. Applied Surface Science, 2020. **517**: p. 146030.
42. Dong, S., et al., A novel and high-performance double Z-scheme photocatalyst ZnO-SnO2-Zn2SnO4 for effective removal of the biological toxicity of antibiotics. Journal of Hazardous Materials, 2020. **399**: p. 123017.
43. Pandimurugan, A. and K. Sankaranarayanan, Antibacterial and photocatalytic activity of ZnO, SnO2 and Zn2SnO4 nanoparticles prepared by Microwave assisted method. Materials Technology, 2021: p. 1-11.
44. Nikolic, N., Z. Marinkovic, and T. Sreckovic, The influence of grinding conditions on the mechanochemical synthesis of zinc stannate. Journal of materials science, 2004. **39**(16): p. 5239-5242.
45. Nikolić, N., T. Srećković, and M. Ristić, The influence of mechanical activation on zinc stannate spinel formation. Journal of the European Ceramic Society, 2001. **21**(10-11): p. 2071-2074.
46. Song, J., et al. Synthesis, Structure and Properties of Super Fine Zn2SnO4. in Key Engineering Materials. 2012. Trans Tech Publ.
47. Dou, J. and Q. Chen, Zinc Stannate Nanostructures for Energy Conversion. Chinese Journal of Chemistry, 2021. **39**(2): p. 367-380.
48. Babar, A., et al., Structural, compositional and electrical properties of co-precipitated zinc stannate. Journal of alloys and compounds, 2011. **509**(27): p. 7508-7514.
49. Masmali, N., Z. Osman, and A. Arof, Recent developments in zinc-based two-cation oxide spinels: From synthesis to applications. Ceramics International, 2021. **47**(3): p. 2949-2962.

50. Choi, S.H., et al., Amorphous Zinc Stannate (Zn2SnO4) Nanofibers Networks as Photoelectrodes for Organic Dye-Sensitized Solar Cells. Advanced Functional Materials, 2013. **23**(25): p. 3146-3155.
51. Choi, S.-H., et al., Microstructural control and selective C 2 H 5 OH sensing properties of Zn 2 SnO 4 nanofibers prepared by electrospinning. Chemical Communications, 2011. **47**(33): p. 9315-9317.
52. Mali, S.S., C.S. Shim, and C.K. Hong, Highly porous Zinc Stannate (Zn 2 SnO 4) nanofibers scaffold photoelectrodes for efficient methyl ammonium halide perovskite solar cells. Scientific reports, 2015. **5**(1): p. 1-14.
53. Zhang, Y., et al., Porous ZnO–SnO2–Zn2SnO4 heterojunction nanofibers fabricated by electrospinning for enhanced ethanol sensing properties under UV irradiation. Journal of Alloys and Compounds, 2021. **854**: p. 157311.
54. Chow, L., et al., Synthesis and characterization of functional nanostructured zinc oxide thin films. ECS Transactions, 2006. **3**(9): p. 65.
55. Chen, C., et al., Efficiency enhanced dye-sensitized Zn 2 SnO 4 solar cells using a facile chemical-bath deposition method. New Journal of Chemistry, 2014. **38**(9): p. 4465-4470.
56. Wang, B., et al., Amorphous inorganic semiconductors for the development of solar cell, photoelectrocatalytic and photocatalytic applications. Chemical Society Reviews, 2021.
57. Dong, M., et al., Microstructure and Microwave Dielectric Properties of TiO2-Doped Zn2SiO4 Ceramics Synthesized Through the Sol–Gel Process. Journal of the American Ceramic Society, 2008. **91**(12): p. 3981-3985.
58. Ma, Q., S. Wu, and Y. Fan, Synthesis and microwave dielectric properties of Zn2SnO4 ceramics. Ceramics International, 2014. **40**(1): p. 1073-1080.
59. Arora, I. and P. Kumar, Effect of annealing temperature on structure-property correlations in Zn2SnO4 nanostructured films for optoelectronics. Materials Research Express, 2020. **7**(3): p. 035023.
60. Thien, N.D., et al., Phase transformation and photoluminescence of undoped and Eu3+-doped zinc stannate (Zn2SnO4) nanocrystals synthesized by hydrothermal method. Journal of Materials Science: Materials in Electronics, 2019. **30**(2): p. 1813-1820.

61. Ruiz-León, D., R. Avila, and C. Venegas, Synthesis and electrical characterization of zinc stannate (zto) prepared by hydrothermal method. Journal of the Chilean Chemical Society, 2015. **60**(3): p. 3029-3032.
62. Dinesh, S., et al., Hydrothermal synthesis of zinc stannate (Zn 2 SnO 4) nanoparticles and its application towards photocatalytic and antibacterial activity. Journal of Materials Science: Materials in Electronics, 2016. **27**(9): p. 9668-9675.
63. Fu, X., et al., Hydrothermal synthesis, characterization, and photocatalytic properties of Zn2SnO4. Journal of Solid State Chemistry, 2009. **182**(3): p. 517-524.
64. Sagadevan, S., et al., Hydrothermal synthesis of zinc stannate nanoparticles spectroscopic investigation. Journal of Materials Science: Materials in Electronics, 2017. **28**(15): p. 11268-11274.
65. Rono, N., et al., A review of the current status of graphitic carbon nitride. Critical Reviews in Solid State and Materials Sciences, 2021. **46**(3): p. 189-217.
66. Chan, M.-H., R.-S. Liu, and M. Hsiao, Graphitic carbon nitride-based nanocomposites and their biological applications: a review. Nanoscale, 2019. **11**(32): p. 14993-15003.
67. Zhao, Z., et al., Synthesis of graphitic carbon nitride from different precursors by fractional thermal polymerization method and their visible light induced photocatalytic activities. Journal of Alloys and Compounds, 2018. **735**: p. 1297-1305.
68. Fang, J., et al., Nitrogen self-doped graphitic carbon nitride as efficient visible light photocatalyst for hydrogen evolution. Journal of Materials Chemistry A, 2015. **3**(26): p. 13819-13826.
69. Dong, G. and L. Zhang, Porous structure dependent photoreactivity of graphitic carbon nitride under visible light. Journal of Materials Chemistry, 2012. **22**(3): p. 1160-1166.
70. Mun, S.J. and S.-J. Park, Graphitic carbon nitride materials for photocatalytic hydrogen production via water splitting: a short review. Catalysts, 2019. **9**(10): p. 805.
71. Prasad, C., H. Tang, and I. Bahadur, Graphitic carbon nitride based ternary nanocomposites: From synthesis to their applications in photocatalysis: A recent review. Journal of Molecular Liquids, 2019. **281**: p. 634-654.
72. Li, C., et al., Synthesis and characterization of nitrogen-rich graphitic carbon nitride. Materials chemistry and physics, 2007. **103**(2-3): p. 427-432.

73. Zhu, J., et al., Graphitic carbon nitride: synthesis, properties, and applications in catalysis. ACS applied materials & interfaces, 2014. **6**(19): p. 16449-16465.
74. Zhang, Y., et al., Porous graphitic carbon nitride synthesized via direct polymerization of urea for efficient sunlight-driven photocatalytic hydrogen production. Nanoscale, 2012. **4**(17): p. 5300-5303.
75. Serpone, N., Photocatalysis. Kirk-Othmer Encyclopedia of Chemical Technology, 2000.
76. Saravanan, R., F. Gracia, and A. Stephen, Basic principles, mechanism, and challenges of photocatalysis, in Nanocomposites for visible light-induced photocatalysis. 2017, Springer. p. 19-40.
77. Banerjee, S., et al., New insights into the mechanism of visible light photocatalysis. The journal of physical chemistry letters, 2014. **5**(15): p. 2543-2554.
78. Ajiboye, T.O., O.A. Oyewo, and D.C. Onwudiwe, Adsorption and photocatalytic removal of Rhodamine B from wastewater using carbon-based materials. FlatChem, 2021. **29**: p. 100277.
79. Yang, X. and D. Wang, Photocatalysis: from fundamental principles to materials and applications. ACS Applied Energy Materials, 2018. **1**(12): p. 6657-6693.
80. Qiu, X., et al., Applications of nanomaterials in asymmetric photocatalysis: recent progress, challenges, and opportunities. Advanced Materials, 2021. **33**(6): p. 2001731.
81. Shivaraju, H., Removal of organic pollutants in the municipal sewage water by TiO2 based heterogeneous photocatalysis. International Journal of Environmental Sciences, 2011. **1**(5): p. 911-923.
82. Low, J., et al., Heterojunction photocatalysts. Advanced materials, 2017. **29**(20): p. 1601694.
83. Safaei, J., et al., Graphitic carbon nitride (gC 3 N 4) electrodes for energy conversion and storage: a review on photoelectrochemical water splitting, solar cells and supercapacitors. Journal of Materials Chemistry A, 2018. **6**(45): p. 22346-22380.
84. Ong, W.-J., et al., Graphitic carbon nitride (g-C3N4)-based photocatalysts for artificial photosynthesis and environmental remediation: are we a step closer to achieving sustainability? Chemical reviews, 2016. **116**(12): p. 7159-7329.
85. Buettner, G.R., The pecking order of free radicals and antioxidants: lipid peroxidation, α-tocopherol, and ascorbate. Archives of biochemistry and biophysics, 1993. **300**(2): p. 535-543.

86. Lopis, A.D., et al., Laddered type-1 heterojunction: Harvesting full-solar-spectrum in scavenger free photocatalysis. Solar Energy, 2022. **240**: p. 57-68.
87. Zeng, J., et al., A novel design of SiH/CeO 2 (111) van der Waals type-II heterojunction for water splitting. Physical Chemistry Chemical Physics, 2021. **23**(4): p. 2812-2818.
88. Kumar, S., et al., Nanoscale zinc oxide based heterojunctions as visible light active photocatalysts for hydrogen energy and environmental remediation. Catalysis Reviews, 2020. **62**(3): p. 346-405.
89. Pan, C., et al., Heterojunction nanomedicine. Advanced Science, 2022. **9**(11): p. 2105747.

CHAPTER 3

3. EXPERIMENTAL

3.1. Reagents

Zinc acetate dihydrate, tin(II) chloride dihydrate, ammonium hydroxide, carbon disulphide, *N*-methylaniline, and ethanol were purchased from Merck chemicals. All reagents where analytical grade and used without further purification.

3.2. Instrumentation

3.2.1. Characterisation of the nanoparticles

Powder X–ray diffractogram (XRD) of the nanoparticles were recorded on a Bruker D8 Advanced XRD machine, equipped with a proportional counter using Cu Kα radiation (λ=1.5405 A, nickel filter). Samples were placed on a flat steel sample holder and scanned from 10 to 80 ºC. The recorded JCPDS standard were matched with the diffraction peak obtained in the samples. The morphology of the nanoparticles was studied using transmission electron microscopy-TEM (Hitachi HF–2000 TEM at 200 kV and FEI Tecnai G 2 Twin at 20 kV), and scanning electron microscopy-SEM (JEOL 6400F Field Emission SEM at 5 kV). Ultraviolet–visible (UV–vis) spectra for all the samples were recorded using varian UV–vis spectrophotometer. The photoluminescence (PL) spectra of the nanoparticles were also measured using Perkin Elmer LS 45 Fluorimeter.

3.3. Synthesis of zinc stannate heterojunctions and g-C_3N_4 incorporated nanoparticles

3.3.1. Synthesis of ammonium *N*-methyl-*N*-phenyldithiocarbamate

The NH_4^+ salt of the ligand (ammonium *N*-methyl-*N*-phenyldithiocarbamate) was prepared by the dropwise addition of carbon disulphide (0.3 mol) to a cold mixture of N-methylaniline (0.3 mol) and ammonium hydroxide (15 mL) in a round bottom flask. The resulting solution was stirred for about 6 h, then filtered and washed with cold ethanol[108].

3.3.2. Synthesis of Zn(II) bis(*N*-methyl-*N*-phenyldithiocarbamate) complex

To a 20 mL ethanol solution of the synthesized ammonium *N*-methyl-*N*-phenyldithiocarbamate (0.1 mol), a 20 mL aqueous solution of $Zn(CH_3COO_2)\cdot 2H_2O$ (0.05 mol) was added. The solution was stirred for 1 h, filtered and the obtained precipitates were washed with a solution of ethanol and water (3:1) and air dried for 12 hours [109].

3.3.3. Synthesis of Sn doped ZnO nanoparticles

About 0.2 g of the synthesised Zn(II) bis(*N*-methyl-*N*-phenyldithiocarbamate) was dispersed in ethanol and sonicated for 5 min. To this suspension, an ethanol solution of tin chloride dihydrate in different percentage ratios (2, 5, 10, 15 and 20%) was added. After stirring for 15 min, the solution was then transferred into an autoclave and heated at 70 - 80 ºC for 4 h. The resulting homogenous mixture was centrifuged and washed with water and ethanol (3- 4 times) to remove any impurities. The product was air dried at room temperature for 24 h to remove the solvent, and then calcinated at 600 ºC for 4 h.

3.3.4. Synthesis of zinc stannate-ZnO nanoparticles

The previously discussed method in 3.3.3 was used with the same percentage ratio but calcination was done at 1000 ºC for 4 h.

3.3.5. Synthesis of zinc stannate-ZnO/g-C_3N_4 nanocomposite

Two methods were employed for the synthesis of the nanocomposites: the *ex-situ* and *in-situ* methods.

3.3.5.1 *Ex-situ* Method

Graphitic carbon nitride (g-C_3N_4) was prepared by the calcination of about 3.30 g of melamine in a crucible at 600 ºC for 4 h. g-C_3N_4 and ZTO-ZnO (obtained in section 3.3.4.) in ratio 10:1 were homogeneously grounded together using pestle and mortar, then transferred into a crucible and calcinated for 1 h at 600 ºC. The resulting product was left to cool to room temperature and collected for analysis.

3.3.5.2 *In-situ* Method

The ZTO-ZnO/g-C_3N_4 was prepared by initially synthesizing ZTO-ZnO nanoparticles as presented in 3.3.4. Finally, the g-C_3N_4/ ZTO-ZnO nanocomposite was prepared by mixing of Melamine and ZTO-ZnO (prepared in 3.3.4.) in ratio 2:1 using mortar and pestle. Then, the blend was transferred into a crucible and calcinated for 4 h at 600 ºC. The resulting product was left to cool to room temperature then collected for analysis.

3.4. Photocatalytic degradation of Cr(VI) in water

The photocatalytic activities of the synthesized g-C_3N_4/ZTO-ZnO@20% and gC_3N_4/ZTO-ZnO@30% were evaluated by studying the degradation of aqueous solution of dichromate ions under visible light irradiation. A 250–W Xe discharge lamp with a circulating water source in the reactor vessel was used for this study. A 0.5 – 2.0 mg/L concentration of the

dichromate ion was prepared and used for the study. For each measurement, 0.5 -2.0 mg of the photocatalyst was introduced into the dichromate ion solution and stirred magnetically in the dark for one hour in order to establish an adsorption equilibrium between the surface of the catalysts and the dichromate ions. The suspension was then exposed to the lamp for 2 h with continuous stirring. During this process, aliquots of the solution were taken at 15, 30, 45, 60, 90 and 120 min. The degradation efficiency of the dichromate ion was studied using UV–visible.

3.5. Calculation of the percentage degradation of Cr(VI)

The percentage of the photocatalytic degradation of dichromate ion was calculated using the following equation:

Degradation yield % = $(C_0 - C_e)/C_0 \times 100$ (3.1)

Where, C_0 is the initial concentration C_e is the concentration of dye after degradation.

REFERENCES

1. Onwudiwe, D.C. and P.A. Ajibade, Synthesis and characterization of metal complexes of N-alkyl-N-phenyl dithiocarbamates. Polyhedron, 2010. 29(5): p. 1431-1436.
2. Onwudiwe, D.C. and P.A. Ajibade, Zn(II), Cd(II) and Hg(II) complexes of N-methyl-N-phenyl dithiocarbamate as single-source precursors for the synthesis of metal sulfide nanoparticles. Materials Letters, 2011. 65(21/22): p. 3258-3261.

CHAPTER 4

4. RESULTS AND DISCUSSION

4.1. X-ray diffraction (XRD) studies

The overlaid X-ray diffraction (XRD) patterns of both the pristine and different concentration of the Sn doped ZnO nanoparticles are presented in Fig 4.1. All the diffraction patterns can be indexed to (100), (002), (101), (102), (110), (103), (200), (112), and (201) planes of hexagonal wurtzite structure. Both pure and doped ZnO nanoparticles crystallized in the hexagonal structure type (space group: P63mc (186)), which corresponds to the JCPDS 00-036-1451 and the lattice constants a =3.24982 Å, and c = 5.20661 Å [1, 2].

The figure showed that the introduction of different Sn-dopant concentration did not change the crystal structure of ZnO at this particular temperature (600 ºC). In addition, the absence of any diffraction peaks attributed to either Sn, SnO_2 or zinc tin oxide confirmed that at 600 ºC, Sn was incorporated into the lattice of ZnO (as a dopant) without the formation of any new phases during this high temperature synthesis process. The incorporation of dopant into the crystalline lattice of materials usually results in lattice strain, and a consequent shift in peak positions [3].

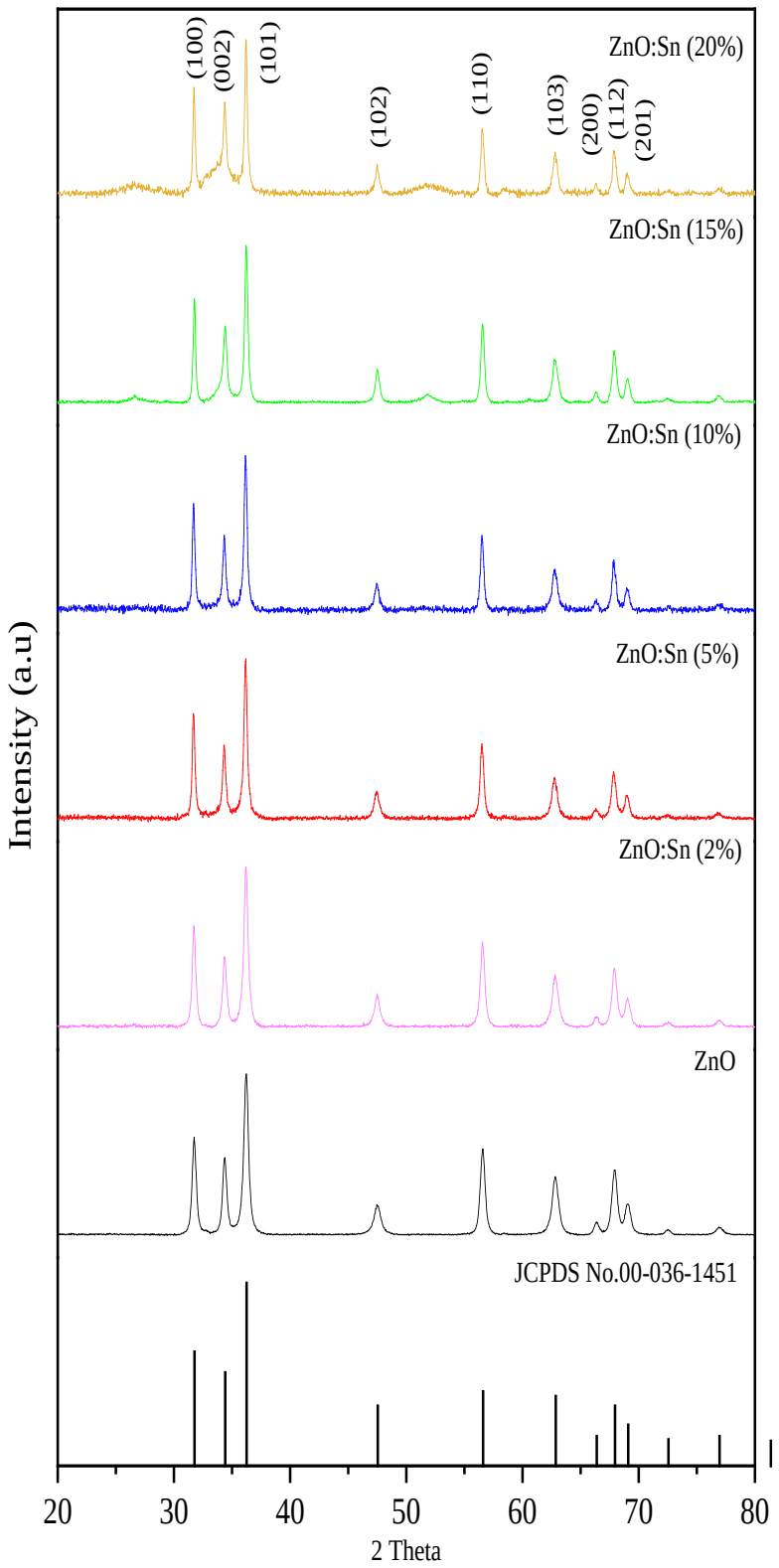

Figure 4. 1: X-ray diffraction patterns of pure and Sn doped ZnO nanoparticles at 600 ºC.

Figure 4.2 presents an overlapped pattern of the three sharp planes in the range 2θ = 30 – 40° for the different doping concentrations. There was a shift in peak positions of the (1 0 0), (0 0 2) and (1 0 1) diffraction patterns towards 2θ = zero, which tends to increase (peak position) with increase in dopant concentration [4]. The peak shifting towards the lower 2θ angle may be due to different strain that arose within the nanoparticles as the doping increased, and also a positive indication for substitutional doping of Sn^{4+} at Zn^{2+} sites, as the ionic radii of Zn^{2+} (0.74 Å) and Sn^{4+} (0.69 Å) are comparable [4].

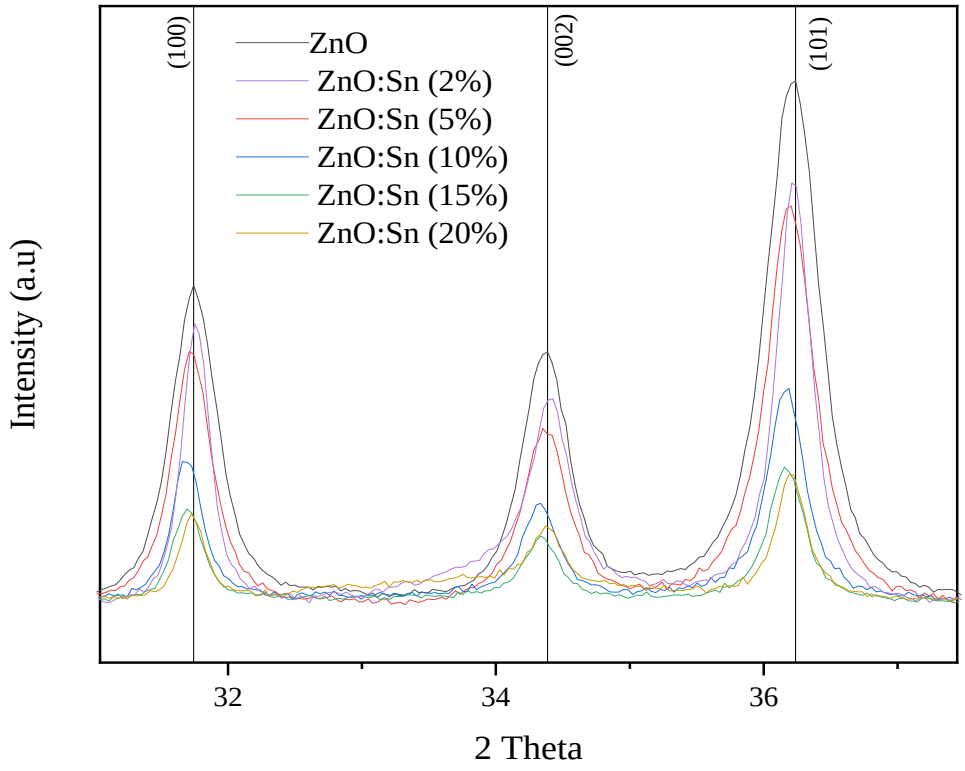

Figure 4. 2: Enlarged view of the (100), (002) and (101) peaks for the X-ray diffraction pattern of pure and Sn doped ZnO nanoparticles at 600 ºC.

Due to the substitution of Zn^{2+} by Sn^{4+} in the lattice of ZnO, a non-uniform stress/strain was generated, which could be related to the remarkable broadening of the diffraction peaks corresponding to (100), (002) and (101) planes shown in Fig 4.2 at 600 ºC. The XRD graph shows that the intensity of the diffraction peaks decreased as the concentration of the Sn was increased. Increase in the concentration of the Sn causes an increase in defects inside the Sn doped ZnO, which then results in a decrease in intensity that indicates poor crystallinity of the sample [5]. Similar results have been reported by Tsay *et al*. [6].

Furthermore, a decrease in the full width at half maximum occurred as the concentration of Sn increased. The full width at half maximum (FWHM) of the pristine ZnO was 0.480, which decreased up to 0.285 in 20% Sn-doped ZnO, thereby suggesting an increase in crystallite size with increase in the Sn concentration and a reduction in the micro-strain [7]. The crystallite sizes (D) of these samples were estimated using the Scherrer's formula:

$$D = \frac{0.94\,\lambda}{\beta Cos\,\theta} \tag{4.1}$$

where λ is the wavelength of X-ray used; β is the broadening of the diffraction line measured at half its maximum intensity; and θ is the diffraction angle, which was calculated from the broadening of the main peak (101). The calculated crystallite size of pure ZnO was 17.0 nm, which increased up to 29.0 nm for the 20% Sn-doped ZnO sample.

An increase in the calcination temperature to 1000 ºC, resulted in the emergence of a peaks at 2θ = 17.9, 29, 34.4, 35.9, 41.8, 51.8, 55, and 60.4, which were ascribed to the (111), (220), (311), (222), (400), (422), (511) and (440) diffraction patterns of zinc tin oxide (ZTO), consistent with the standard JCPDS card No: (00-0 24-1470), and corresponded to the face-centered cubic structure of ZTO with lattice constant a= 8.65740 [8]. This new zinc stannate peak at such a very high temperature could be as a result of the formation SnO_4 and subsequent reaction of this oxidised form of Sn with the ZnO (obtained at 600 ºC), thereby resulting in Zn_2SnO_4-ZnO. Two phases were formed, ZTO and ZnO.

Figure 4.3 (A-E) presents the overlapped XRD patterns for the samples prepared at 600 and 1000 ºC using 2, 5, 10, 15 and 20% Sn dopant respectively. It could be observed that only ZnO was clearly observable in Fig 4.3 (A) and ZTO became more conspicuous as the concentration of Sn was increased, which was clearly observable in Fig 4.3 (E). The samples obtained at 1000 ºC showed improved crystallinity compared to those at 600 ºC, therefore confirming that temperature has a good effect on crystallinity.

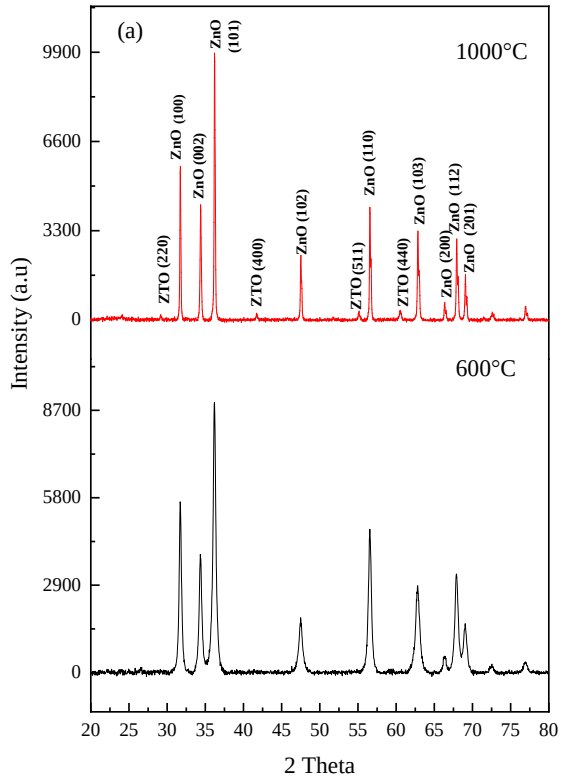
(a)
1000°C
600°C
ZTO (220)
ZnO (100)
ZnO (002)
ZnO (101)
ZTO (400)
ZnO (102)
ZTO (511)
ZnO (110)
ZTO (440)
ZnO (103)
ZnO (200)
ZnO (112)
ZnO (201)
Intensity (a.u)
2 Theta

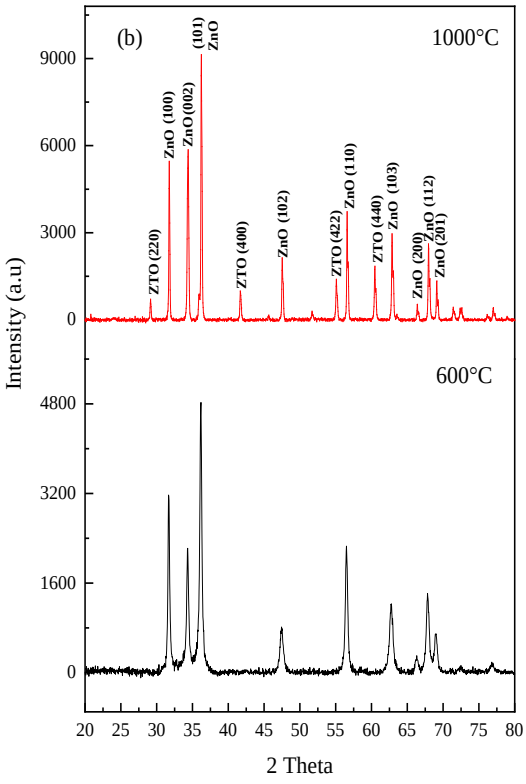
(b)
1000°C
600°C
ZTO (220)
ZnO (100)
ZnO (002)
(101) ZnO
ZTO (400)
ZnO (102)
ZTO (422)
ZnO (110)
ZTO (440)
ZnO (103)
ZnO (200)
ZnO (112)
ZnO (201)
Intensity (a.u)
2 Theta

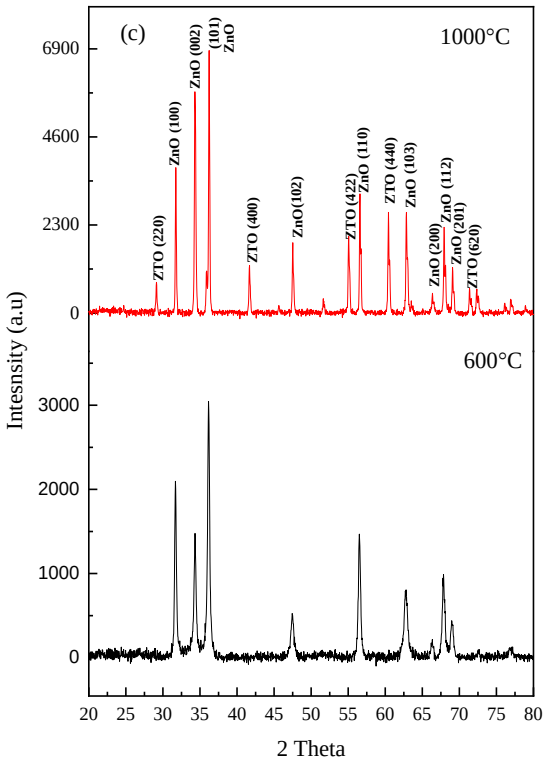
(c)
1000°C
600°C
ZTO (220)
ZnO (100)
ZnO (002)
(101) ZnO
ZTO (400)
ZnO(102)
ZTO (422)
ZnO (110)
ZTO (440)
ZnO (103)
ZnO (200)
ZnO (112)
ZnO (201)
ZTO (620)
Intesnsity (a.u)
2 Theta

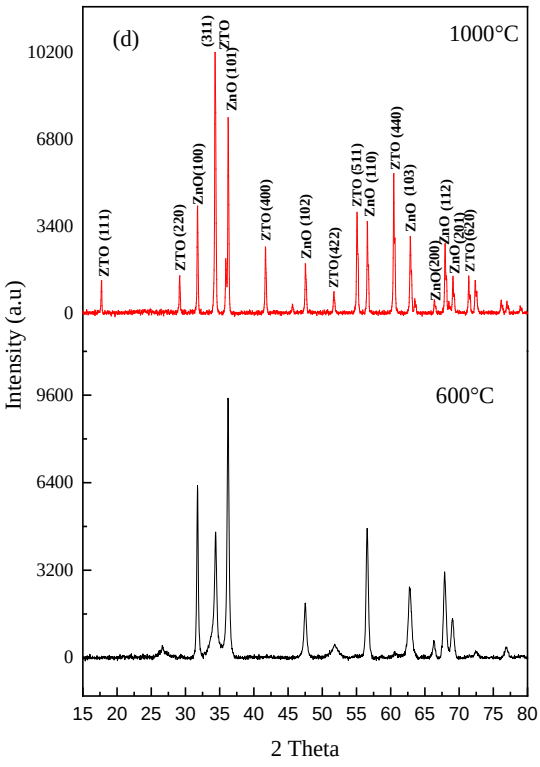
(d)
1000°C
600°C
ZTO (111)
ZTO (220)
ZnO(100)
(311) ZTO
ZnO (101)
ZTO (400)
ZnO (102)
ZTO(422)
ZTO (511)
ZnO (110)
ZTO (440)
ZnO (103)
ZnO(200)
ZnO (112)
ZnO (201)
ZTO(620)
Intensity (a.u)
2 Theta

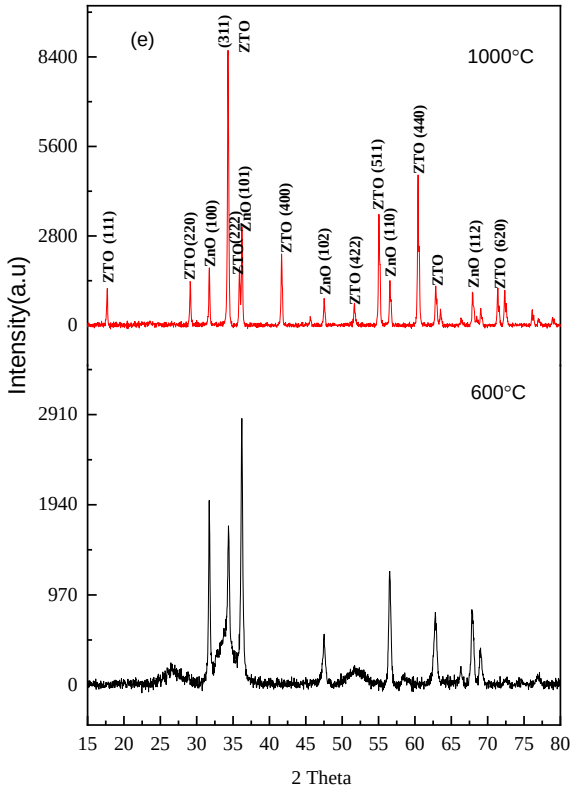

Figure 4. 3: XRD pattern of the complex metal oxide prepared at different temperature (600 and 1000 ºC) using Zndtc and $SnCl_2$ at (2%)(A), (5%)(B), (10%)(C), (15%)(D), (20%)(E).

Williamson Hall method was also used to estimate the crystallite size. This is a simplified integralbreadth method, where both size induced, and strain induced broadening are deconvol -uted by considering the peak width as a function of 2θ [9]. The plots are shown in Fig 4.4, and the calculated crystallite size from Scherrer and Williamson Hall are shown in Table 4.1. The crystallite size (D) for Sn doped ZnO samples showed an increase with increase in the concentration of Sn, from 19.6 nm (2% Sn) to 29.3 nm (20% Sn) and from 28.9 nm (2% Sn) to 86.2 nm (20% Sn) for Scherrer and Williamson hall method respectively.

In the case of the ZTO-ZnO sample, where two phases are involved, the crystallite size for ZnO showed an increase for the Scherrer method from 35.5 nm to 41.1 nm while a decrease was observed for the Williamson hall method from 93.1 nm to 18.3 nm as Sn concentration increased (from 2%Sn to 20%Sn). Furthermore, a decrease in crystallite size was observed for ZTO obtained via the Scherrer's method while the Williamson hall displayed an increasing trend. When compared, the values of the crystallite size obtained by the Williamson-Hall analysis showed large variation, about twice the size of the crystallite size

obtained for Scherrer's method. This variation could be due to differences in averaging the particle distribution [10].

Williamson Hall method is more viable in this study as the increase in ZTO is observed as Sn concentration is increased. This could be that more SnO_2 are formed which then reacts with the ZnO to form the ZTO causing an increase in the size of ZTO as concentration of Sn doping increased, therefore resulting in a reduction of ZnO as more ZTO are formed.

The Williamson Hall method was also used to estimate the strain through a plot of $\beta\cos\theta$ versus $4\sin\theta$. A linear plot was observed in Figures 4.4, 4.5 and 4.6 which is a plot displayed by a substance that experiences elastic deformation due to thermal stress [11]. The strain (ε) present in the material and the crystallite size (D) are calculated from the slope and y-intercept, respectively, of linear fit data plot presented in the 3 Figures (4.4, 4.5, and 4.6). A variation and increase in lattice strain were observed in Table 4.1. The variation in strain could be due to the change in size and microstructure of the particles.

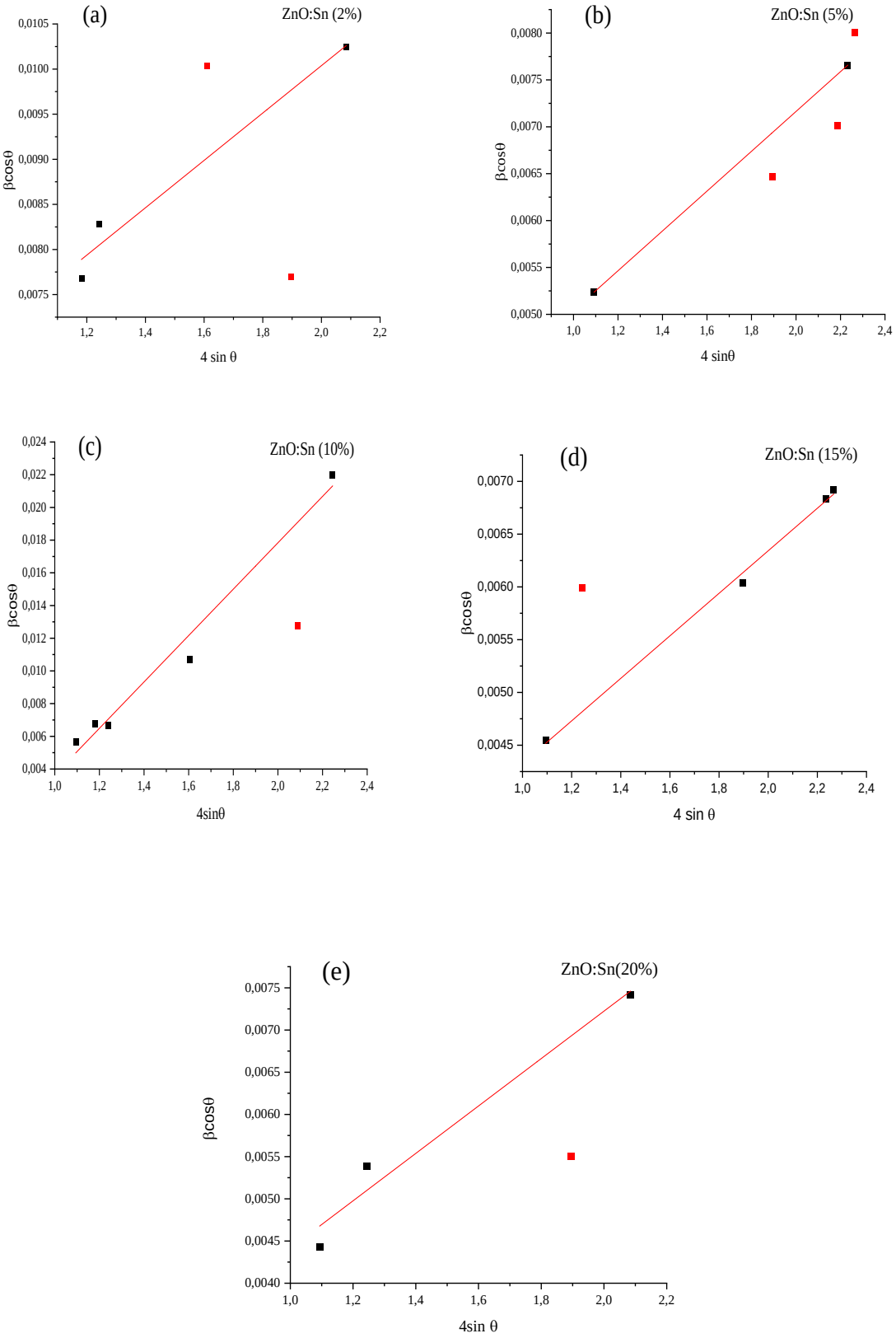

Figure 4. 4: Plot of βhkl cosθ vs 4sinθ of the Sn doped ZnO samples at (2%)(A), (5%)(B), (10%)(C), (15%)(D), (20%)(E) Sn doping at 600 ºC .

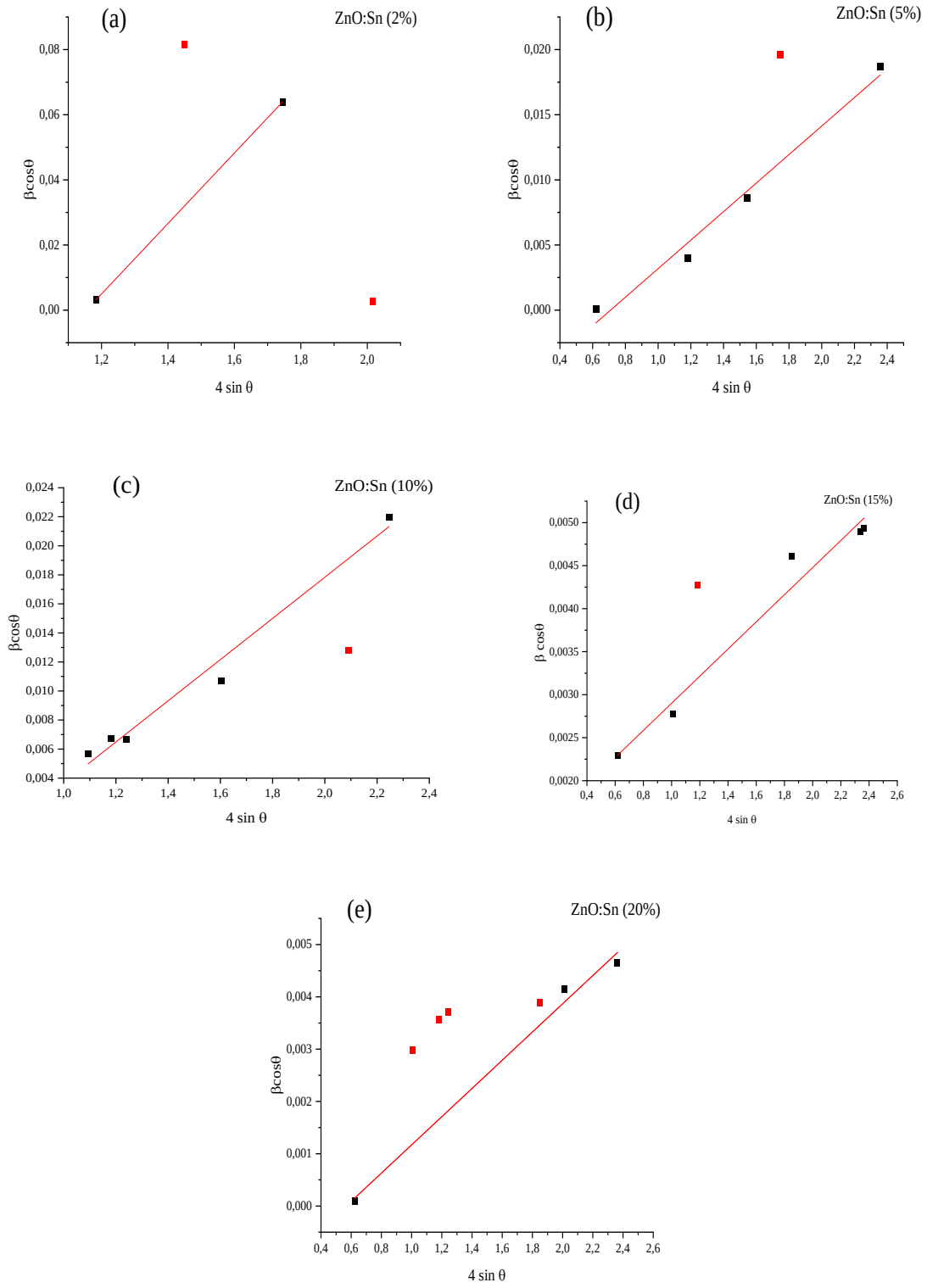

Figure 4. 5: Plot of βhkl cosθ vs 4sinθ of the ZnO samples at (2%)(A), (5%)(B), (10%)(C), (15%)(D), (20%)(E) Sn at 1000 ºC.

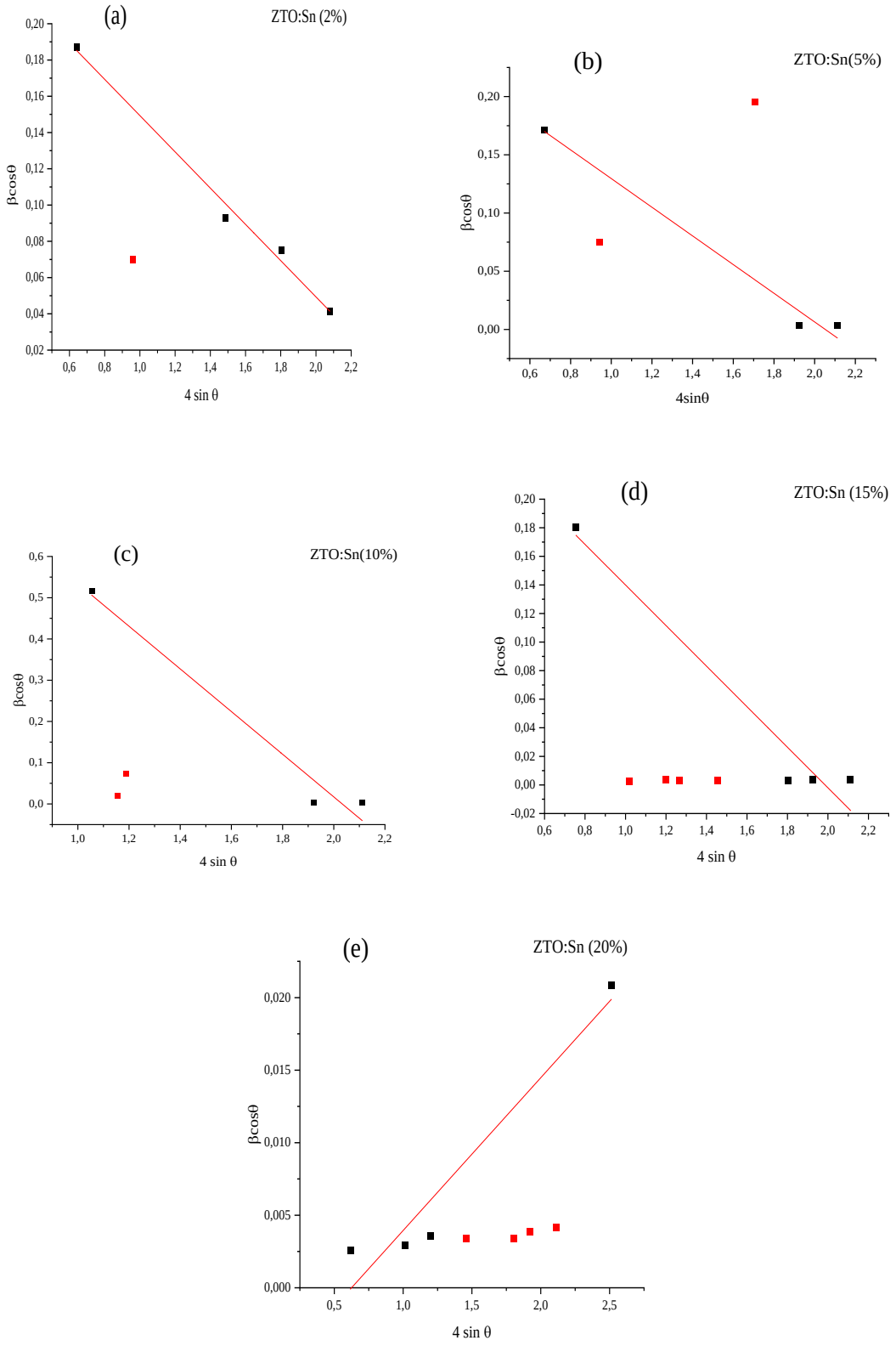

Figure 4. 6: Plot of βhkl cosθ vs 4sinθ of the ZTO samples at (2%)(A), (5%)(B), (10%)(C), (15%)(D), (20%)(E) Sn at 1000 ºC.

Table 4. 1: The geometric parameters of ZnO, Sn doped ZnO and ZTO-ZnO nanoparticles prepared at different calcination temperatures (600 & 1000 ºC) for (2%)(A), (5%)(B), (10%)(C), (15%)(D), (20%)(E).

(A)

Sample	Scherer Method	Williamson- hall method	
	D nm	D nm	ε x 10^{-3}
ZnO	17,4	19.8	0.675
Sn doped ZnO-02% (600˚C)	19.6	28.9	2.63
ZnO ZTO-02% (1000˚C)	35.6 81.0	93.1 1.11	1.22 108.23

(B)

Sample	Scherer Method	Williamson- hall method	
	D nm	Dnm	ε x 10^{-3}
ZnO	17,4	19.8	0.675
Sn doped ZnO-05% (600ºC)	24.9	47.5	2.12
ZnO ZTO-05% (1000ºC)	36.2 60.0	106.7 17.8	1.28 10.95

(C)

Sample	Scherer Method	Williamson- hall method	
	D nm	Dnm	ε x 10^{-3}
ZnO	17,4	19.8	0.675
Sn doped ZnO-10% (600˚C)	26.7	13.2	14.18
ZnO ZTO-10% (1000˚C)	37.1 55.5	88.9 64.2	1,14 2.88

(D)

Sample	Scherer Method	Williamson- hall method	
	D nm	Dnm	ε x 10^{-3}
ZnO	17,4	19.8	0.675
Sn doped ZnO-15% (600˚C)	26.7	60.1	2.02
ZnO ZTO-15% (1000˚C)	39.5 57,4	86,2 105.1	1.07 1.58

(E)

Sample	Scherer Method	Williamson- hall method	
	D nm	Dnm	ε x 10^{-3}
ZnO	17,4	19.8	0.675
Sn doped ZnO-20% (600˚C)	29.3	86.2	2.81
ZnO ZTO -20% (1000˚C)	41.1 51.9	18,3 90.6	3,08 2.7

Doping alters the lattice properties of nanoparticles and affects their structural and geometrical parameters. Table 4.2 (A-E) summarises the lattice properties of the Sn doped ZnO (600 ºC) and the complex metal oxide nanoparticles, ZTO-ZnO (1000 ºC). The table showed that increase in the concentration of Sn doping increased the cell volume, calculated by using the formula $V = 0.866a^2c$, from 47.6714 in pure ZnO to 47.8185 for the 20% Sn doped ZnO.

The lattice parameters (a and c) showed only a slight change with increase in the percentage of Sn doping (for example the value of "a" changes from 8.6497 in 2% Sn to 8.6664 in 20% Sn). The cell volume also experienced an increase ranging from 647.1472 ($Å^3$) to 650.9028 ($Å^3$). Although, only slight change occurred in the cell volume in both Sn doped ZnO and ZTO-ZnO with increase in dopant concentration, the difference between the cell volume of Sn doped ZnO and ZTO is quite huge. The cell volume for 20% Sn doped ZnO is 47.8185 ($Å^3$) while that of 20% ZTO is 650.9028 ($Å^3$). This implies that a significant change in the cell volume could only be observed when there is a structural change, and very slight change in the dopant concentration may not alter the structure but could induce a strain/stress in the ZnO lattice. Further studies were done on the obtained ZTO-ZnO by incorporating the nanoparticle into g-C_3N_4 to form a ternary heterojunction nanocomposite.

Table 4. 2: The structure parameters of ZnO, Sn doped ZnO & ZTO-ZnO nanoparticles prepared at different calcination temperatures (600 & 1000 ºC) for (2%) (A), (5%)(B), (10%)(C), (15%)(D), (20%)(E).

(A)

Sample	2θ	Hkl	Dhkl (Å)	Structure	Lattice Parameter (Å)	V(Å^3)
ZnO	31.76 36.25	100 101	2.8173 2.4773	Hexagonal	a = 3.2531 c = 5.2017 c/a = 1.5989	47.6714
Sn doped ZnO-02% (600˚C)	31.71 36.20	100 101	2.8217 2.4810	Hexagonal	a = 3.2582 c = 5.2087 c/a = 1.5986	47.8853
ZTO-ZnO-02% (1000˚C)	34.38	311	2.6079	Face centred cubic	a = 8.6497	647.1472

(B)

Sample	2θ	Hkl	Dhkl (Å)	Structure	Lattice Parameter (Å)	V(Å^3)
ZnO	31.76 36.25	100 101	2.8173 2.4773	Hexagonal	a = 3.2531 c = 5.2017 c/a = 1.5989	47.6714
Sn doped ZnO-05% (600˚C)	31.66 36.19	100 101	2.8260 2.4823	Hexagonal	a = 3.2632 c = 5.1933 c/a = 1.5914	47.8904
ZTO-ZnO-05% (1000˚C)	34.39	311	2.6076	Face centred cubic	a = 8.6482	646.8173

(C)

Sample	2θ	Hkl	Dhkl (Å)	Structure	Lattice Parameter (Å)	V(Å^3)
ZnO	31.76 36.25	100 101	2.8173 2.4773	Hexagonal	a = 3.2531 c = 5.2017 c/a = 1.5989	47.6714
Sn doped ZnO-10% (600˚C)	31.69 36.15	100 101	2.8230 2.4844	Hexagonal	a = 3.2598 c = 5.2309 c/a = 1.6046	48.1366
ZTO-ZnO-10% (1000˚C)	34.32	311	2.6130	Face centred cubic	a = 8.6664	650.9028

(D)

Sample	2θ	Hkl	Dhkl (Å)	Structure	Lattice Parameter (Å)	V(Å^3)
ZnO	31.76 36.25	100 101	2.8173 2.4773	Hexagonal	a = 3.2531 c = 5.2017 c/a = 1.5989	47.6714
Sn doped ZnO-15% (600˚C)	31.75 36.20	100 101	2.8182 2.4807	Hexagonal	a = 3.2541 c = 5.2275 c/a = 1.6064	47.9373
ZTO-ZnO-15% (1000˚C)	34.35	311	2.6105	Face centred cubic	a = 8.6581	649.0322

(E)

Sample	2θ	Hkl	Dhkl (Å)	Structure	Lattice Parameter (Å)	V(Å^3)
ZnO	31.76 36.25	100 101	2.8173 2.4773	Hexagonal	a = 3.2531 c = 5.2017 c/a = 1.5989	47.6714
Sn doped orZnO-20% (600˚C)	31.73 36.22	100 101	2.8201 2.4798	Hexagonal	a = 3.2563 c = 5.2075 c/a = 1.5992	47.8185
ZTO-ZnO-20% (1000˚C)	34.32	311	2.6130	Face centred cubic	a = 8.6664	650.9028

Two methods: *in-situ* and *ex-situ* were used to incorporate the binary nanocomposite (ZTO-ZnO) into the g-C_3N_4 and the results are presented in Figures 4.7 (A and B) respectively. The XRD pattern for g-C_3N_4, ZTO-ZnO (Sn:20%) and g-C_3N_4/ZTO-ZnO (Sn:30%) are also shown in Figure 4.7. The diffraction pattern of the g-C_3N_4 exhibited a peak around 28 ºC corresponding to (002) plane of g-C_3N_4 (JCPDS 00-087–1526) [12, 13]. The (0 0 2) plane is a characteristic interplanar stacking peaks of aromatic systems. The XRD patterns of ZTO-ZnO showed characteristic peaks which could be indexed to the (111), (220), (311), (222), (400), (422), (511), (440), (531), (533) and (622) plane of cubic structure, with lattice constant a=8.65740 Å [14].

The obtained data is consistent with (JCPDS : 00-024-1470), indicating the formation of ZTO of cubic phase [15]. All the other diffraction peaks can be assigned to hexagonal phase with Wurtzite structure, space group (P63mc) (186), JCPDS card No.36-1451 and unit cell parameters a = b = 3.249823 Å and c = 5.20661 Å indicating the formation of ZnO. The g-

C_3N_4/ZTO-ZnO nanocomposite displayed peaks from the precursor materials: ZTO-ZnO and g-C_3N_4, which confirmed the incorporation of ZTO-ZnO nanoparticles into the g-C_3N_4. There was no additional phase identified, which confirmed the purity of the synthesized samples. However, comparing the diffraction pattern of the ternary nanocomposites obtained via the two methods, showed that the *in-situ* method (Figure 4.7A) was more effective than the *ex-situ* method (Figure 4.7B) for the incorporation of the nanocompositing process. The g-C_3N_4 and nanoparticles were better incorporated for both ZTO-ZnO (Sn:20%) and ZTO-ZnO (Sn:30%), as the peaks for both the nanoparticle and g-C_3N_4 could be clearly seen in the figure. In Figure 4.7B both materials (g-C_3N_4 and nanoparticles) were only incorporated at higher dopant concentration (30%), and higher intensity of the peaks were observed. The poor compositing product in the *ex-situ* approach could be due to the short reaction time during the synthesis in the *ex-situ* (1h) compared to the process time(4h), in the *in-situ* approach.

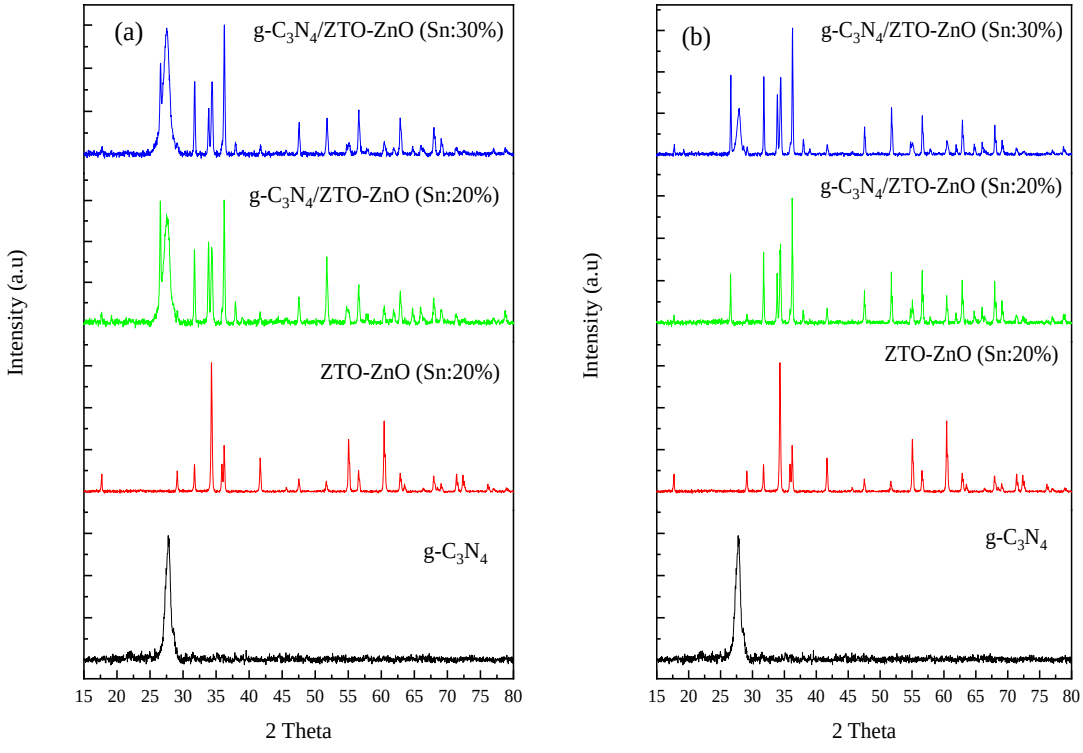

Figure 4. 7: (A) X-ray diffraction patterns of pure g-C_3N_4, ZTO-ZnO(Sn:20%), g-C_3N_4/ZTO-ZnO(Sn:20%) and g-C_3N_4/ZTO-ZnO(Sn:30%) nanocomposite calcinated at 600 ºC *in-situ* method and (B) X-ray diffraction patterns of pure g-C_3N_4 ZTO-ZnO(Sn:20%), gC_3N_4/ZTO-

ZnO(Sn:20%) and g-C_3N_4/ZTO-ZnO(Sn:30%) nanocomposite calcinated at 600 ºC *ex-situ* method.

The compositing of materials with g-C_3N_4 could alter its polymeric nature and results in a shift in the characteristic (002) peak positions. Figure 4.8 presents the overlapped diffraction pattern of pristine g-C_3N_4 and the nanocomposites with 20 and 30% dopant concentration. A shift in the (002) plane towards lower 2θ could be observed for ZTO-ZnO (Sn:20%) and ZTO-ZnO (Sn:30%) and could be attributed to a successful incorporation of the ternary metal oxide into g-C_3N_4, located in the in-plane holes of carbon nitride (bound to the nitrogen atoms) [16].

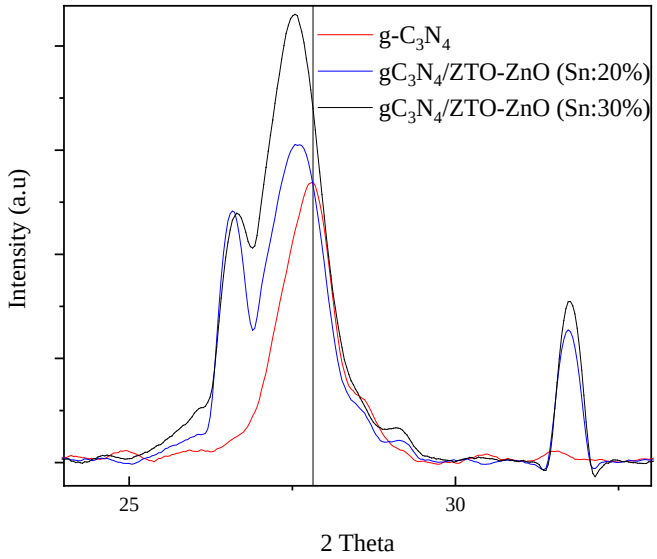

Figure 4. 8: Enlarged view of peaks at around 28 ºC for the x-ray diffraction pattern of pure g-C_3N_4, g-C_3N_4/ZTO-ZnO@20% and gC3N4/ZTO-ZnO@30% nanoparticles at 600 ºC

4.1.1. Proposed synthesis pathway for the synthesis of Sn doped ZnO and ZTO-ZnO nanoparticles

The successful utilisation of metal DTC complexes as single source precursors relies on both the volatility of the metal complexes and the bond strength of the metal–sulphur and carbon–sulphur bonds. The thermal decomposition of some M(II) (Ni and Zn) and M(III) (Cr and Co) complexes of *N*-methylbenzyl– and 4-morpholine–DTC complexes, were reported as early as 1974 [17]. The complexes were reported to decompose to their respective metal sulphides with the loss of H_2S, and the formation of isothiocyanate as intermediate product [18]. Recent

studies have confirmed this as a general trend amongst most dithiocarbamate complexes [19]. However, these are based on observation deduced from experiment conducted under inert atmosphere without the possibility of oxidation.

Based on the calcination product and supported by the reported decomposition pathways of metal dtc, studied with the help of GC-MS [18, 20], a schematic representation of decomposition profile leading to ZnO has been proposed and presented in Scheme 4.1. The first decomposition step was the homolytic dissociation of [$Zn(S_2CNRPh)$] into $Zn(S_2CNRPh)$ and S_2CNRPh radicals. Although, the possibility of a heterolytic dissociation exists, the homolytic scission of the metal–sulphur bond to generate a dithiocarbamate radical is significantly more favourable than heterolytic scission. About 143 kJ mol^{-1} energy was required for the former and 678 kJ mol^{-1} for the later in an experiment conducted using [$Cu(S_2CNEt_2)_2$] [21-23].

Therefore, with similar [$Zn(S_2CNRPh)$], a possible slightly lower enthalpy is expected for a homolytic dissociation. After this first decomposition, there are possible pathways for the second step: (a) the dissociation of the second dithiocarbamate radical via an intramolecular rearrangement (a′) to form ZnS moieties and the loss of thiocyanide and an alkyl group; (b) the dimerization of the resulting $Zn(S_2CNRPh)$ and S_2CNRPh radicals (from the homolytic cleavage) to form a thiuram moiety accompanied with the formation of Zn metal. It is hard to distinguish between these processes, but considering that zinc has no redox chemistry; and therefore, cannot undergo an intramolecular oxidative-addition, it is expected that the homolytic loss of the second dithiocarbamate radical would have an energy barrier very similar to the first dithiocarbamate loss. A free-radical decomposition mechanism has been supported by a study by Wold *et al*., [24] via studying the organic components of the decomposition of [$Zn(S_2CNEt_2)_2$] at 450 °C using mass spectrometry, which identified EtNCS, Et_2NH, CS_2, and ethylene as products.

In the presence of oxygen (such as in the current study conducted in open air), pathway (c) showed that oxidation of the Zn metal could take place, resulting in the formation of ZnO. The introduction of Sn(II) led to the formation of Sn within the lattices of the ZnO resulting in the formation of Sn doped ZnO at 600 ºC (path d) as illustrated in the XRD pattern of Fig 4.1. However, as the temperature increased to 1000 ºC, oxidation of Sn to SnO_2 took place, followed by the reaction of the SnO_2 with the ZnO to form a stannate. This last step was strongly dependent on the concentration of the of the Sn precursor in the starting reagent.

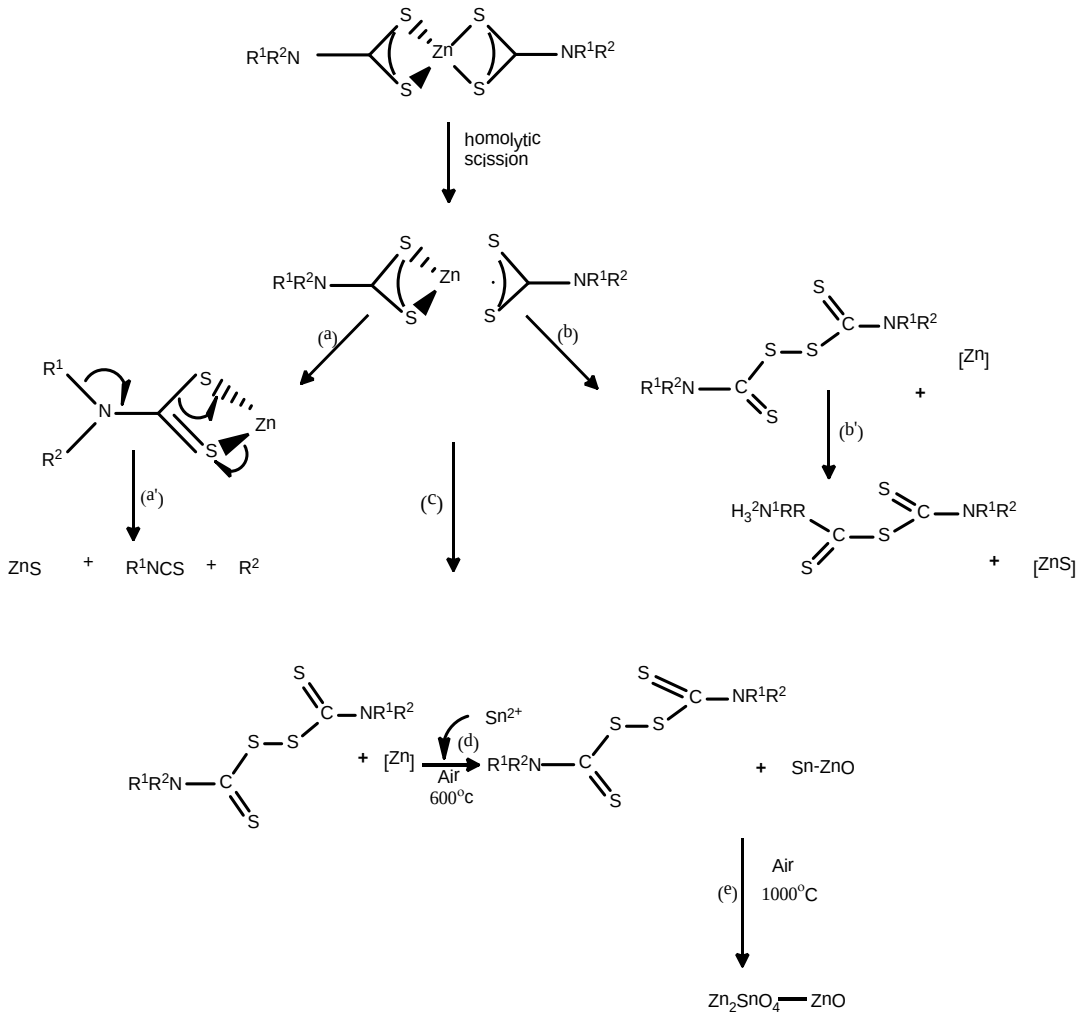

Scheme 4. 1: Schematic representation of possible decomposition mechanism of the complex in air

Since the decomposition of metal dithiocarbamate is to some extent dependent on the nature of the substituents, Me_2, Et_2, Pr_2, Bu_2, Bz_2, Ph_2, PhEt etc, the product of decomposition of the complex with the same type of substituents (alkyl and aryl) on the nitrogen atom: dimethyl dithiocarbamate and diphenyl dithiocarbamate were studied. In both metal complexes, ZnO was obtained as shown in Fig 4.9, thereby indicating that the product of calcination in air is independent on the type of substituent. The decomposition of these complexes under inert atmosphere was reported to yield ZnS nanoparticles as shown in Fig 4.10 [25]. A graphical representation of the different products obtainable from Zndtc at different synthesis conditions is presented in Scheme 4.2

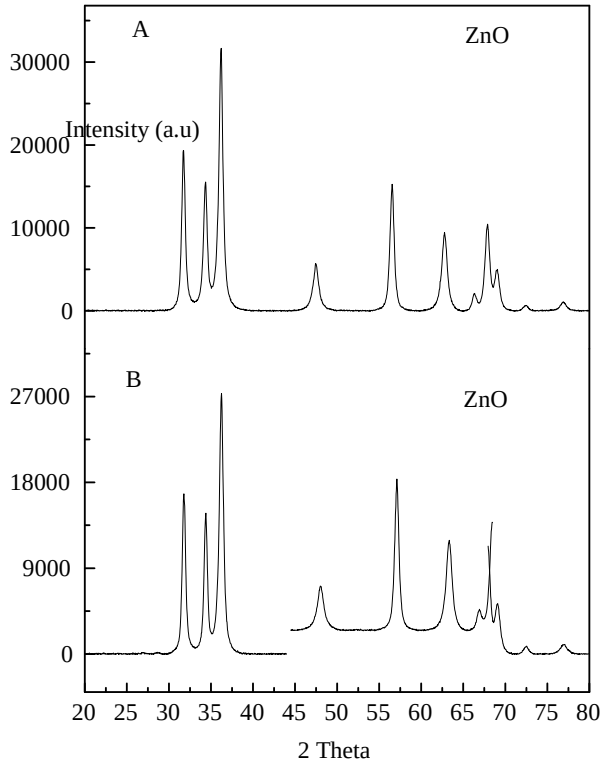

Figure 4. 9: X-ray diffraction patterns of ZnO nanoparticles formed from calcination of Zn (II) bis (diethyl dithiocarbamate)- (A) and Zn (II) bis (diphenyl dithiocarbamate)-(B) at 600 ^{o}C.

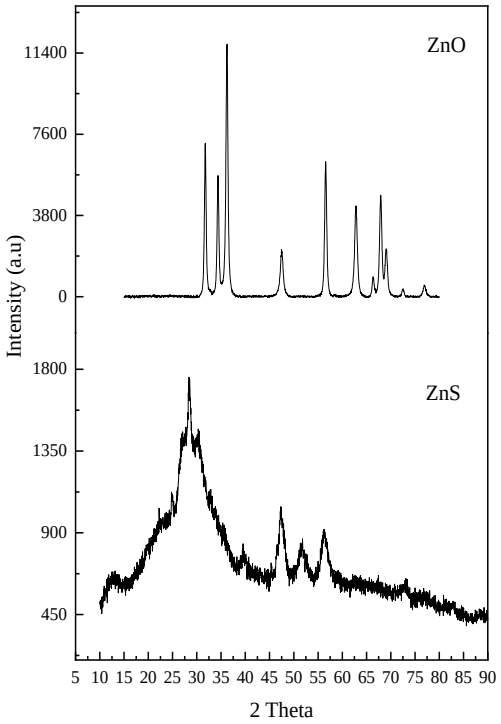

Figure 4. 10: X-ray diffraction patterns of ZnO and ZnS nanoparticles obtained by the calcination of Zndtc in air and under nitrogen atm respectively at 600 ºC.

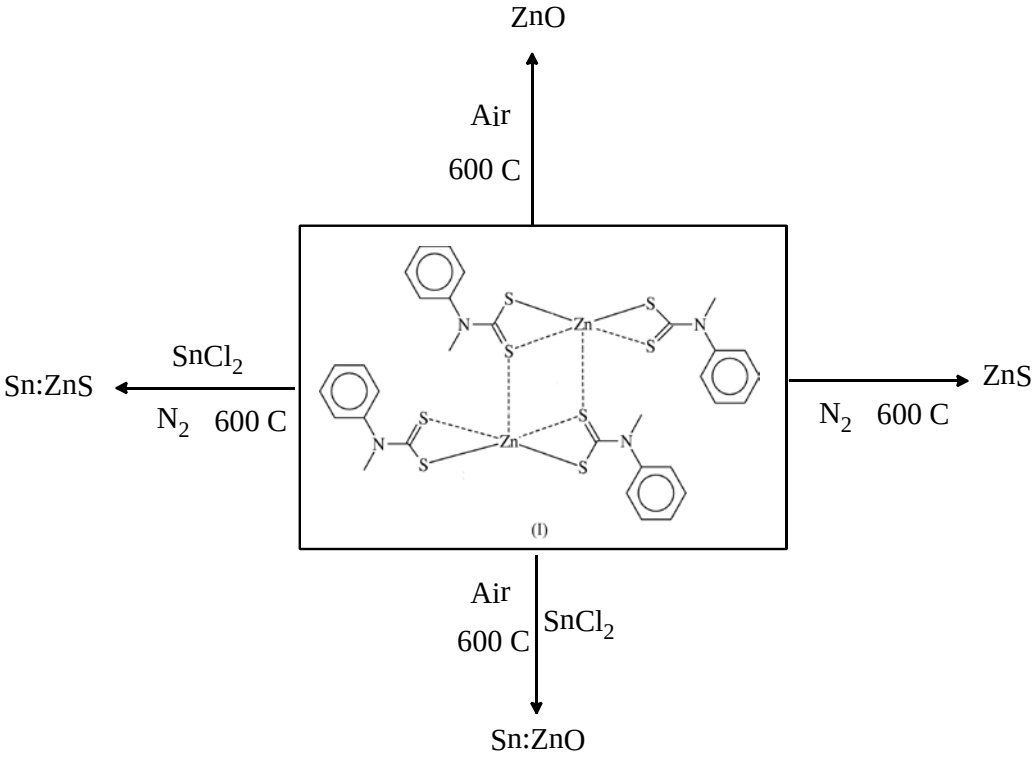

Scheme 4. 2: Synthetic pathway for ZnS, ZnS : Sn, ZnO and ZnO : Sn through calcination of Zn(II) bis N-methyl-N-phenyl dithiocarbamate at 600 ºC.

4.2 UV–vis absorption studies of the Sn doped ZnO

The absorption studies of the prepared Sn doped ZnO samples was conducted in order to examine the influence of Sn doping on the optical properties of ZnO nanoparticles, and the spectra are shown in Fig 4.11. The pristine ZnO shows a steep rise of the absorption edge due to band–band transition to a maximum of about 320 nm. A steep increase in optical absorption has been attributed to the electron transition that occurs between valence band and conduction band of ZnO nanoparticles and this has been observed within the 320 to 360 nm region [26]. The spectra of the ZnO:Sn nanoparticles showed a red shift in the absorption edge, which was an indication of a decrease in the optical band gap energy. As a result of the decrease in band gap the absorption region is altered and extended from ultraviolet to visible region. Furthermore, this is demonstrated by the tauc plot which shows a decrease in band gap as the absorption extents from uthravioet to visible region. This phenomenon is ascribed to the effect of doping on the carrier density [27].

The increase in absorption as the dopant concentration increases could be due to the observed decrease in crystallinity of the material as confirmed from the XRD[28]. Doping of ZnO by Sn atoms implies the substitution of Zn sites by Sn atom, whereby they could act as ionized donors that promote the formation of deep states in the forbidden band gap energy region [29]. Figure 4.12 is the energy level diagram of ZnO showing the intrinsic point defects [30]. Proper doping of ZnO may result in intrinsic defects in ZnO materials to a certain lower level, thereby improving its photoelectric properties [31].

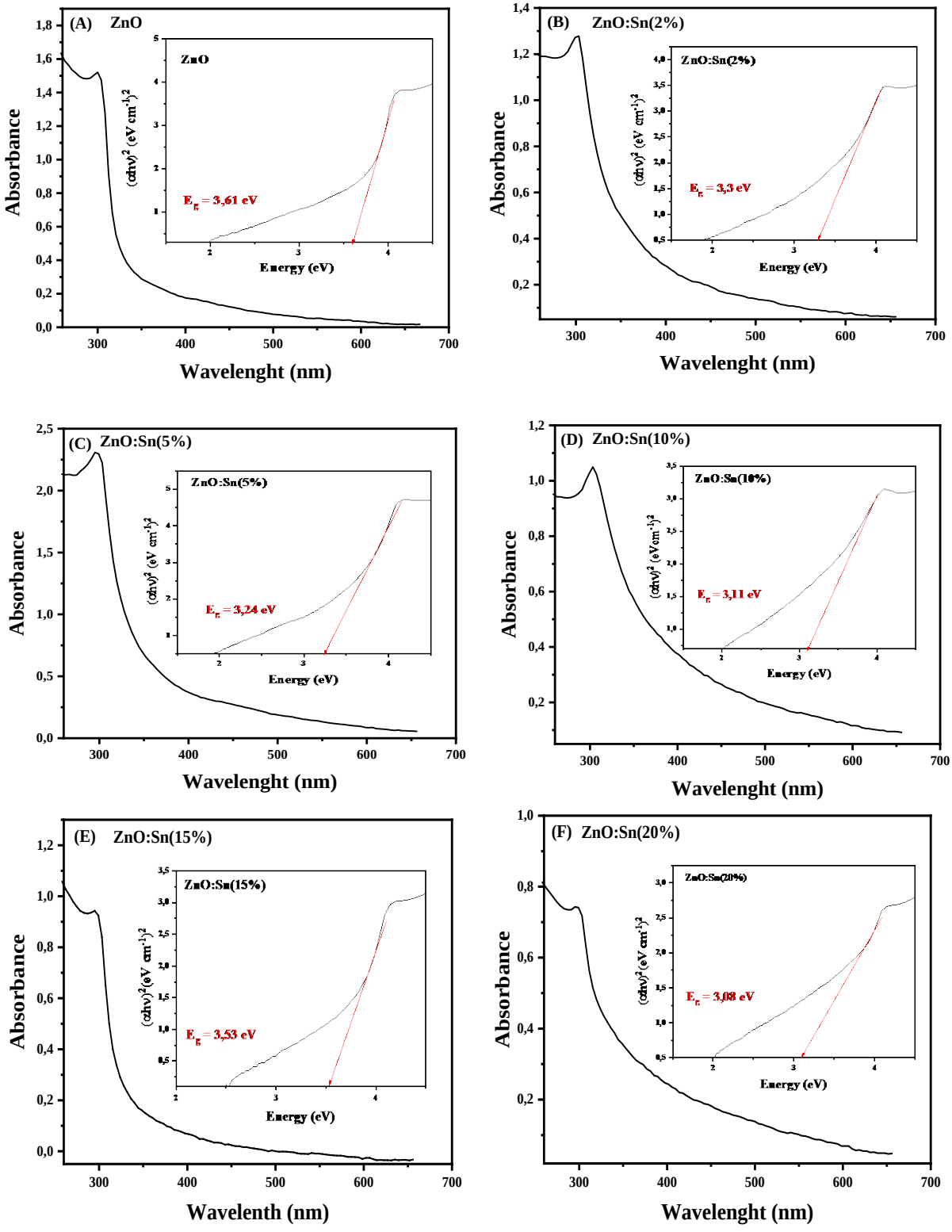

Figure 4. 11: Absorbance spectra of (a) ZnO, (b) ZnO:Sn(2%), (c) ZnO:Sn(5%), (d) ZnO:Sn(10%), (e) ZnO:Sn(15%) and (f) ZnO:Sn(20%). Their respective Tauc plot is in the inset.

The band gap energy could be deduced from the relationship between the absorption coefficient (α) and photon energy (hν) for direct transition semiconductor material using the equation:

$$(\alpha h\nu)^2 = A\,(h\nu - Eg)^n \qquad (4.2)$$

where h is Planck's constant, ν is the photon frequency, A is a band edge constant, Eg is the optical band gap, n could either be $\frac{1}{2}$, $\frac{3}{2}$, 2 or 3, for direct allowed, direct forbidden, indirect allowed and indirect forbidden transition respectively, and α is the absorption coefficient. In this study, we focus on ZnO and ZnO:Sn which are both considered as materials with direct band gap energy, therefore n= ½ [32]. The band gap energy was estimated by the extrapolation of the linear portion of $(\alpha h\nu)^2$ versus hν plot as shown in the insets of Fig 4.11.

The values of the band gap energies obtained for the pristine and Sn doped ZnO are presented in Table 4.3, which showed that the values ranged from 3.61 eV for the pristine ZnO [33, 34] to 3.08 eV in the ZnO:Sn(20%). It indicated a decrease in the band gap energies as the concentration of the Sn atom increased. The band gap of Sn doped Zno showed a reduction compared to pristine ZnO [29, 35]. This could be attributed to presence of localized levels, which exist in the forbidden gap due to the Sn doping. Furthermore, it is also a consequence of the change in the position of the valance band because of the introduction of Sn 5s orbitals [36]. Sn^{2+} ions introduce deep states in the band gap energy of the ZnO, creating a new state lying just below the CB. The conduction process emanating from deep donors is often ascribed to the impurity band or hopping conduction. This is contrary to the conventional free electrons that are excited from the valence band to the conduction band. Any processes mediated by carriers would depend on the relevant conduction mechanisms [36].

Table 4. 3: Band gap energies of pristine ZnO and Sn doped ZnO nanoparticles at different dopant concentration

Samples	**Band gap energy (eV)**
ZnO	3.61
ZnO:Sn (2%)	3.29
ZnO:Sn (5%)	3.24
ZnO:Sn (10%)	3.11
ZnO:Sn (15%)	3.53
ZnO:Sn (20%)	3.08

The Sn doping within the ZnO lattice activates electron-hole pairs and creates surface defects associated with oxygen vacancies [37]. In the presence of Sn metal, the Schottky barrier is formed between Sn and ZnO due to the energy level of CB of ZnO being higher than the Fermi level of ZnO:Sn, thereby leading to free electrons in CB that could be transferred from ZnO to Sn as shown in the electronic band structure of the Sn doped ZnO nanoparticles in Fig 4.12. This results in the prevention of the recombination of electrons and holes on the surface of ZnO [38].

During calcination there is a chance that Sn enters the interstitial site of ZnO since the ionic radius of Sn (0.55) is quite similar to that of Zn (0.60). Sn on the surface of ZnO captures the photoelectron through the surface plasmon effect, and results in the transfer of the same to absorbed O_2 to generate superoxide radicals. Therefore, incorporation of Sn ion effectively suppresses the electron-hole recombination, and acts as an electro trap, facilitating the quick discharge of electrons from the semiconductor photocatalyst to molecular oxygen [39].

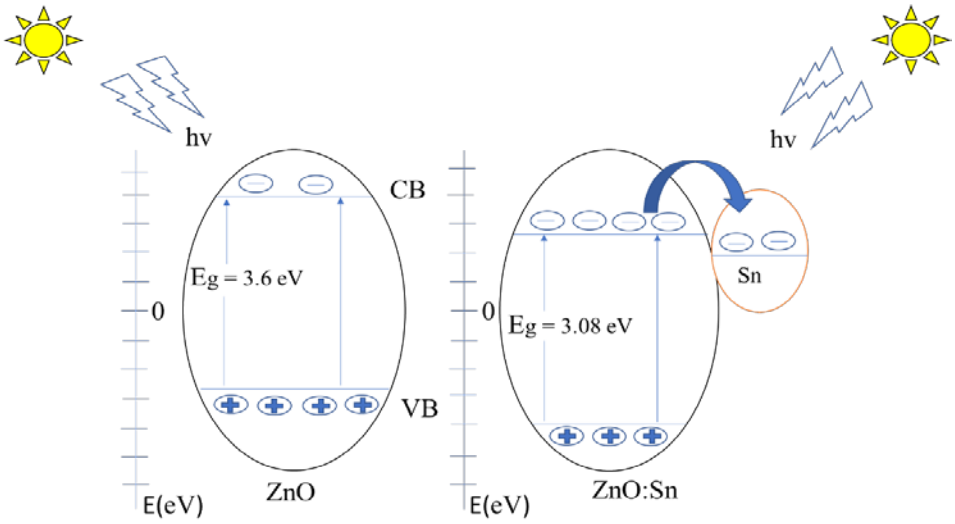

Figure 4. 12: Schematic energy band diagram of ZnO and ZnO:Sn nanoparticles showing the charge transportation processes

Crystal defects in semiconductor photocatalysts permit the excitation of electrons from the valence band to the conduction band. Surface and core defects in nanoparticles are of great importance for photocatalysis reactions. The defect states in the nanocrystals activate visible light photocatalysis in metal oxide semiconductors[40]. The calcination process involved in the synthesis of the Sn doped ZnO lead to the crystal defects and the formation of ZTO-ZnO.

The UV spectra of the ZTO-ZnO are shown in Fig 4.13. An increase in the concentration of the Sn ion increased the ZTO content, which also resulted in a red shift. The red shift is attributed to the increased formation rate of electron−hole pairs on the semiconductor surface[41], resulting in higher photochemical activity. Table 4.4 presents the band gap energies of the different samples with variation in the concentration of Sn ion, which follows a decreasing trend from ZTO-ZnO(2%) to ZTO-ZnO(30%). It has been established that the formation of a heterojunction of ZTO and ZnO resulted in increased photochemical activity as compared to Sn doped ZnO.

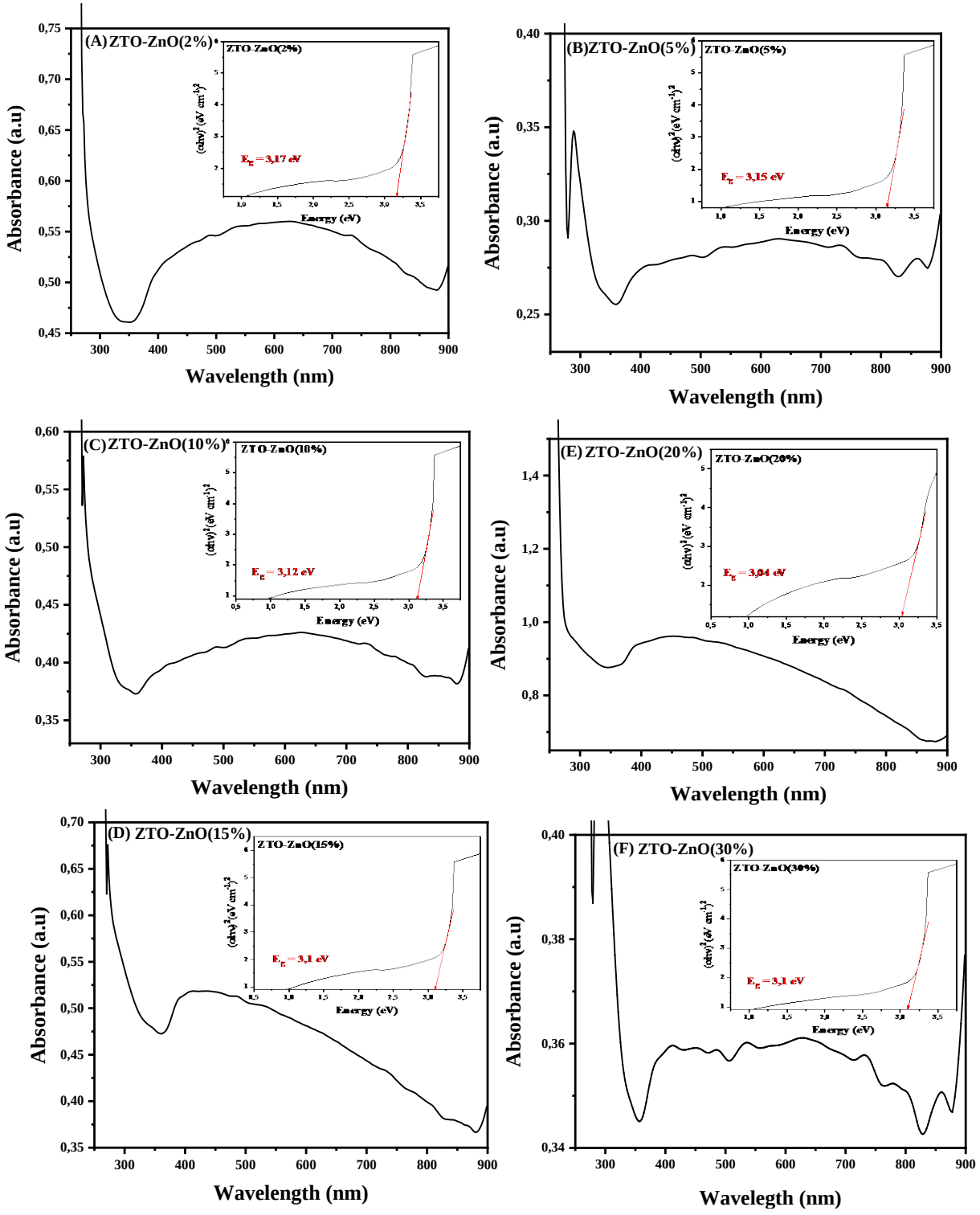

Figure 4. 13: Absorption spectra of (a) ZTO-ZnO(2%), (b) ZTO-ZnO(5%), (c) ZTO-ZnO(10%), (d) ZTO-ZnO (15%), (e) ZTO-ZnO(20%) and (f) ZTO-ZnO(30%), with their respective Tauc plot in the inset.

Table 4. 4: Band gap energy of ZTO-ZnO nanoparticles

Sample	Band gap energy (eV)
ZTO-ZnO (2%)	3.17
ZTO-ZnO (5%)	3.15
ZTO-ZnO (10%)	3.12
ZTO-ZnO (15%)	3.1
ZTO-ZnO (20%)	3.04
ZTO-ZnO (30%)	3.1

Upon the irradiation of ZTO-ZnO with visible light, whose photon energy is greater or equal to the band gap of ZTO and ZnO, excitation of electrons (e^-) from the valence band to the conduction band takes place with simultaneous generation of the same amount of holes in the valance band. Due to the conduction band of ZTO being more positive than that of ZnO, suggesting that electron affinity of ZTO is larger than that of ZnO, electrons are migrated from the conduction band of ZnO to that of ZTO. At the same time, the holes are migrated from the valence band of ZnO to that of ZTO [42], since valence band edge of ZTO is more positive than the ZnO.

During this process, the photogenerated electrons could be trapped by electronic acceptor such as adsorbed O_2 to produce a superoxide anion radical ($\cdot O_2^-$) while the hydroxyl radicals ($\cdot$OH) are formed by the reaction of the photoinduced holes with adsorbed H_2O on the surface of the semiconductor. The $\cdot O_2^-$ radicals formed could react with electrons and hole to produce H_2O_2 that would provide hydroxyl radical($\cdot$OH) by acting as a direct electron acceptor via the reaction with electrons and ($\cdot O_2^-$). The hydroxyl radical ($\cdot$OH) is a strong oxidant for the partial or complete mineralization of organic chemicals [43].

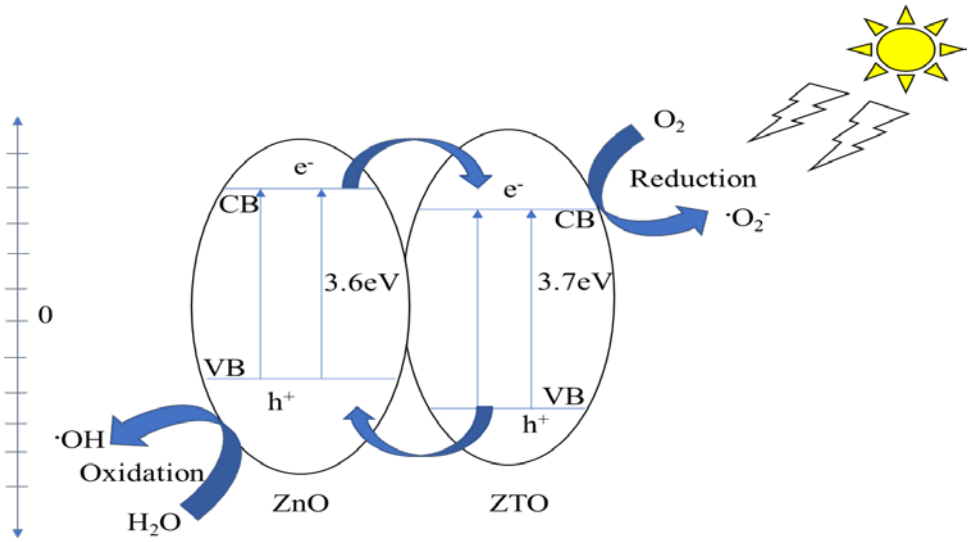

Figure 4. 14: Schematic energy band diagram of ZTO-ZnO heterojuntion nanoparticle showing the charge transportation processes.

The optical absorption spectra of pure g-C_3N_4, g-C_3N_4/ZTO-ZnO(20%) and g-C_3N_4/ZTO-ZnO(30%) are shown in Fig 4.15. Pure g-C_3N_4 showed a maximum absorption peak at 320 nm. Compared with the pristine g-C_3N_4, both g-C_3N_4/ZTO-ZnO(20%) and g-C_3N_4/ZTO-ZnO(30%) nanocomposites showed a decrease in the intensity of the maximum peak at 320 nm upon the introduction of g-C_3N_4.

The observations are attributed to the interaction between g-C_3N_4 and ZTO-ZnO in the composites. The improved photocatalytic activity is attributed primarily to the synergistic effect of the unique structure with various favourable properties. These include separation of photogenerated electron-hole pairs at the heterojunction interfaces caused by matching band structure.

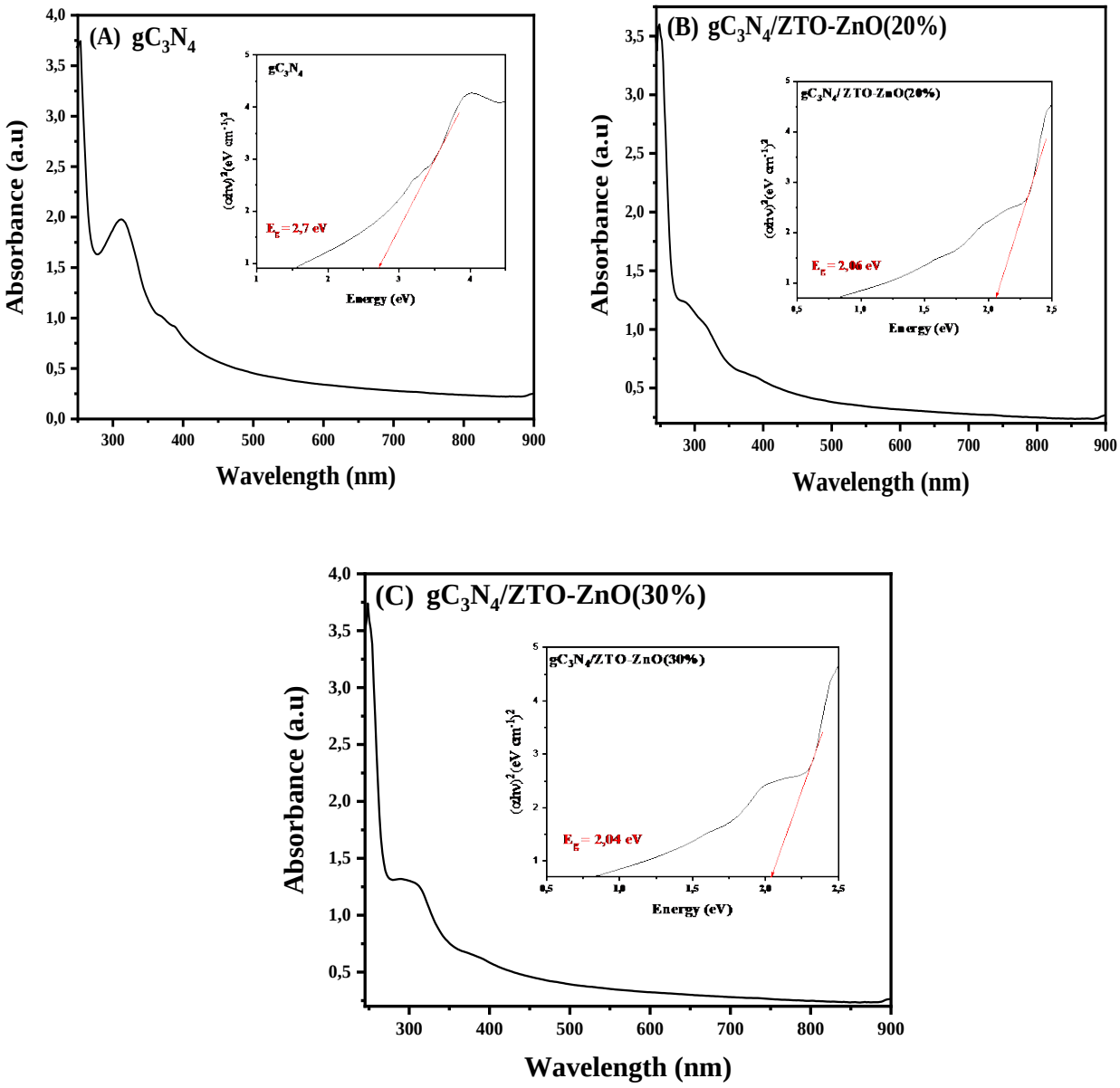

Figure 4. 15: Absorption spectra of (A) gC_3N_4, (B) gC_3N_4/ZTO-ZnO(20%), and (C) gC_3N_4/ZTO-ZnO(30%). Insets are the respective Tauc plot obtained from a plot of $(\alpha h\nu)^2$ versus $h\nu$.

The band gap of the g-C_3N_4, g-C_3N_4/ZTO-ZnO(20%) and g-C_3N_4/ZTO-ZnO(30%) were estimated from the intercept of the tangents to the plots of $(\alpha h\nu)^2$ vs photoenergy (Fig 4.15) as 2.7, 2.08 and 2.06 eV respectively, suggesting that the band gap could be narrowed by the introduction of a heterojunction into g-C_3N_4 interlayers [44]. In addition to narrowing the band gap and enhancing visible light absorption, the introduction of the heterojunction into the g-C_3N_4 interlayer also downshifts the valence band position to improve the hole's oxidation capability [45]. Some of the light-excited electrons in the g-C_3N_4 could be rapidly

transferred at the interface of the composite, while other electrons remain where they are to directly react with O_2 to produce $\cdot O_2^-$. As a result, the prepared g-C_3N_4/ZTO-ZnO(20%) and g-C_3N_4/ZTO-ZnO(30%) ternary composites exhibit considerable enhancement on the photocatalytic activity as compared to pure g-C_3N_4, ZTO-ZnO(20%) and g-C_3N_4/ZTO-ZnO(30%) due to the absorption delving into the visible region [46]. Fig 4.16 presents the schematic energy band diagram showing the charge transportation process.

When g-C_3N_4 is irradiated by light, it generates excited electrons and holes. Since the conduction band energy of g-C_3N_4 is more negative than that of ZTO and ZnO, the excited electrons on the CB of g-C_3N_4 will migrate to the CB of ZnO, which then further migrate to the CB of ZTO driven by the inner electric field between them. Concurrently, the holes generated in the VB of ZTO will also migrate to the VB of ZnO and further transfer to the VB of g-C_3N_4. Therefore, resulting in an effective three-level transfer of photoexcited electron-holes in the ternary composite system. There is also an adequate separation of photogenerated electron-hole pairs at the heterojunction interfaces. This allows for the creation of more reactive species to participate in the photodegradation process.

At the CB of ZTO, the ($\cdot O_2^-$) formed is as a result of electrons trapped by O_2 molecules adsorbed on the surface of the composite. Then, the produced ($\cdot O_2$) on the surface of ZTO reacts with electrons and H^+ in succession to form active ($\cdot OH$) radicals, which are crucial oxidizing species. Thus, the synergistic effect of the nanosheet shapes and matching band structure between g-C_3N_4, ZnO and ZTO is believed to contribute to the enhanced photocatalytic activity of g-C_3N_4/ZnO/ZTO ternary composites [47]. After importing the surface oxygen vacancies on the composite, a number of shallow surface oxygen vacancy states would emerge and partially overlap with the valance band maximum of the heterojunction. This could lead to the rising of the valance band maximum and the shrinking of band gap width [48] in the ternary heterojunction system.

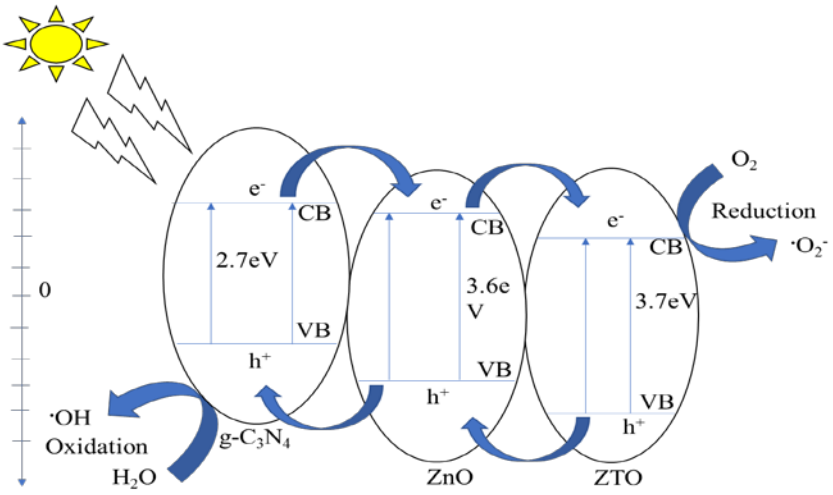

Figure 4. 16: Schematic energy band diagram of g-C_3N_4 and ZTO-ZnO nanoparticles showing the charge transportation processes

4.3 Photoluminescence spectroscopy (PL)

Photoluminescence spectroscopy studies were employed to determine the electronic structure and properties of the material. Red shift from 340 for pristine ZnO to 400 nm for Sn doped ZnO photoluminescence spectra shown in Figure 4.17 suggest substitutional incorporation of Sn^{2+} at Zn sites. It is evident that, substitutional incorporation of dopant ions at host sites can create defects in nanocrystals [49]. It could be observed that the intensity decreases as the dopant concentration increases, and this suggests a lower recombination rate of charge carriers [50]. Doping of the ZnO by Sn in the semiconductor's lattice is helpful for the trapping of excitons which could ultimately result in the charge separation and inhibition of recombination process.

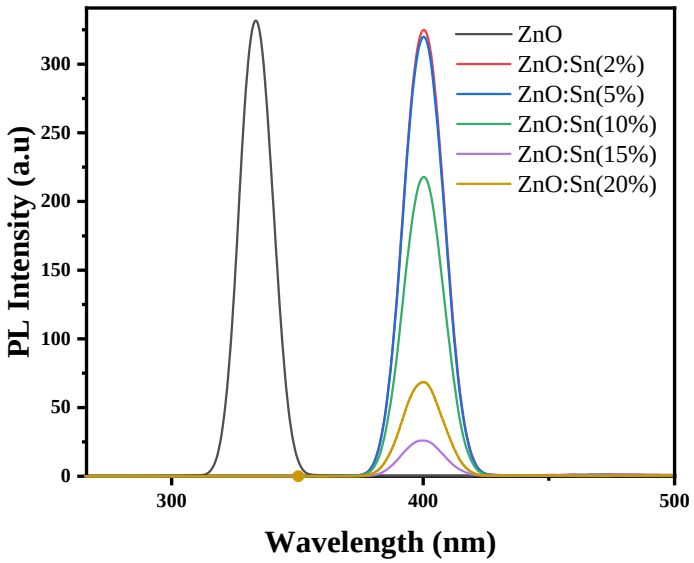

Figure 4. 17: Photoluminescence spectra for pure ZnO and Sn-doped ZnO nanoparticles.

PL spectra of ZTO-ZnO are shown in Fig 4.18. It was used to further explore the effects of forming a heterojunction of different Sn ratios at room temperature. The PL spectra show mainly two common peaks for the five samples. The first peak at 400 nm at the UV region could be due to excitonic emission caused by the Coulombic forces between electron-hole pairs, while the second peak observed at 800 nm occurs due to yellow-green defect emission which could be attributed to the recombination between electrons and trapped holes [51].

The third peak which appears at 460 nm is the blue emissions attributed to intrinsic defects such as Zn and oxygen interstitials which can only be observed for the three higher concentrations of Sn (10, 15 and 20%) [52], suggesting that the defects become more observable as the concentration of Sn was increased. It can be observed that the intensity decreased as the concentration of Sn was increased. The ZTO-ZnO (20%) represented the weakest PL intensity among all the five photocatalysts, suggesting that it's the most efficient photocatalyst since it held the most efficient restriction of recombination of photo-generated electron-hole pairs in the multi-component system.

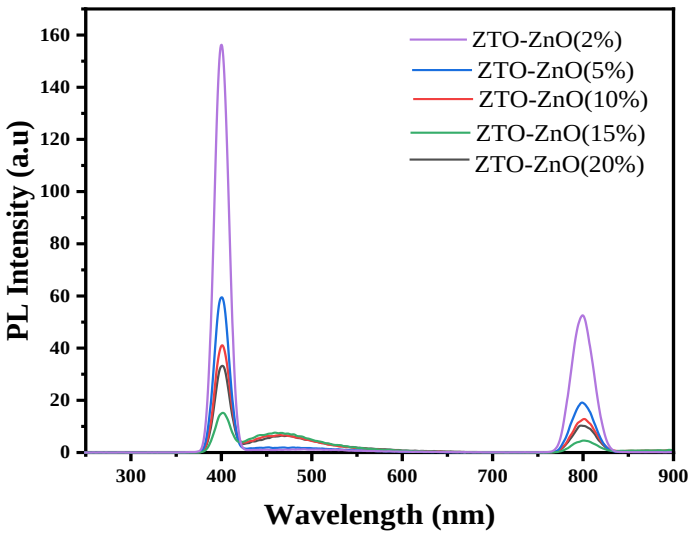

Figure 4. 18: Photoluminescence spectra of ZTO-ZnO nanoparticles.

The composite, ZTO-ZnO Fig (4.18), and pristine g-C_3N_4, Fig (4.19), in their uncombined form exhibited PL with emission peaks around 400 and 460 nm respectively, thus confirming a high electron-hole recombination rate in them. PL intensity was decreased through the coupling of these separate catalysts. This confirms that the formation of heterojunction between the material resulted in inhibition of electron-hole recombination, thus causing an increase in its photocatalytic activity [53, 54].

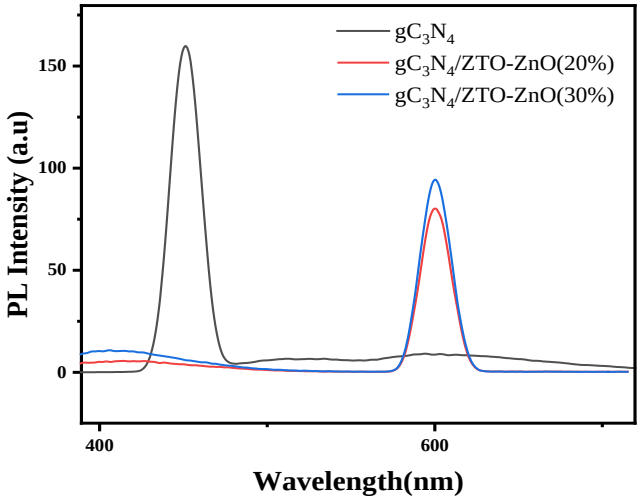

Figure 4. 19: Photoluminescence spectra for gC_3N_4, gC_3N_4/ZTO-ZnO(20%) and gC_3N_4/ZTO-ZnO(30%) nanoparticles.

4.3 Morphological studies

4.3.1. Scanning Electron Microscopy

Figures 4.20 present the SEM micrographs of pristine ZnO and Sn doped ZnO samples at lower concentration (2 and 5%), while Figure 4.21 presents the images at higher dopant concentration (10, 15 and 20%). The micrographs show that the nanoparticles are spherical in shape for both pristine ZnO and at lower dopant concentration (2 and 5%), with distinct change in morphology and greater agglomeration observed in the particles with ≥10% dopant concentration (Figures 4.21). The sample with 10% Sn presents ZnO nanoparticles with plate-like structures, which became quasi-spherical at 15% Sn concentration and finally more spherical morphology as the concentration reached 20%.

A number of factors have been reported to impact on the morphology of nanostructured materials. These include, the choice of precursors, capping agents, doping elements, solvents and the experimental conditions such as temperature, pressure and time which could affect the reaction mechanisms [55]. In this study, factors such as precursor material, doping element, solvent and all other experimental conditions were kept the same throughout the study, with only one parameter varied which was the concentration of the dopant ion Sn^{2+}. Therefore, the difference in the morphologies could only be attributed to the change in the amount of dopant concentration. The morphology of pristine ZnO, at lower and higher magnification in Fig 4.21 (a-b) show the presence of small spherical aggregates. The undoped ZnO is heterogeneous in nature [56, 57]. A closer view of the higher magnification images (shown at the right hand panels) indicated that as the Sn concentration was increased smooth surface morphologies became distinct with a few granular particles on the top of the surface. The variation in the morphology may also be due to the dipolar interaction of the ZnO along the c-axis with Sn^{2+} substitution of Zn^{2+} atoms [58].

The surface micrographs showed that the doping of Sn plays a significant role in changing and improving the structure of the ZnO nanospheres. When the concentration of Sn dopant was further increased, the Sn-doped ZnO nanoparticles showed noticeable variations in the surface morphology [59]. At 20% Sn concentration the morphology changed to large agglomerations that are covered in a few granular particles [59]. The Sn dopant on ZnO could be the driving force which results in anisotropic growth of crystals, hence the observed granular shape [56, 60]. The higher magnification images also showed an increase in grain size as Sn dopant concentration increased. This variation in grain size may be due to the

aggregation of small particles into large grains during annealing of samples at 600°C [61], furthermore, also indicating that the samples could be highly crystalline in nature [60].

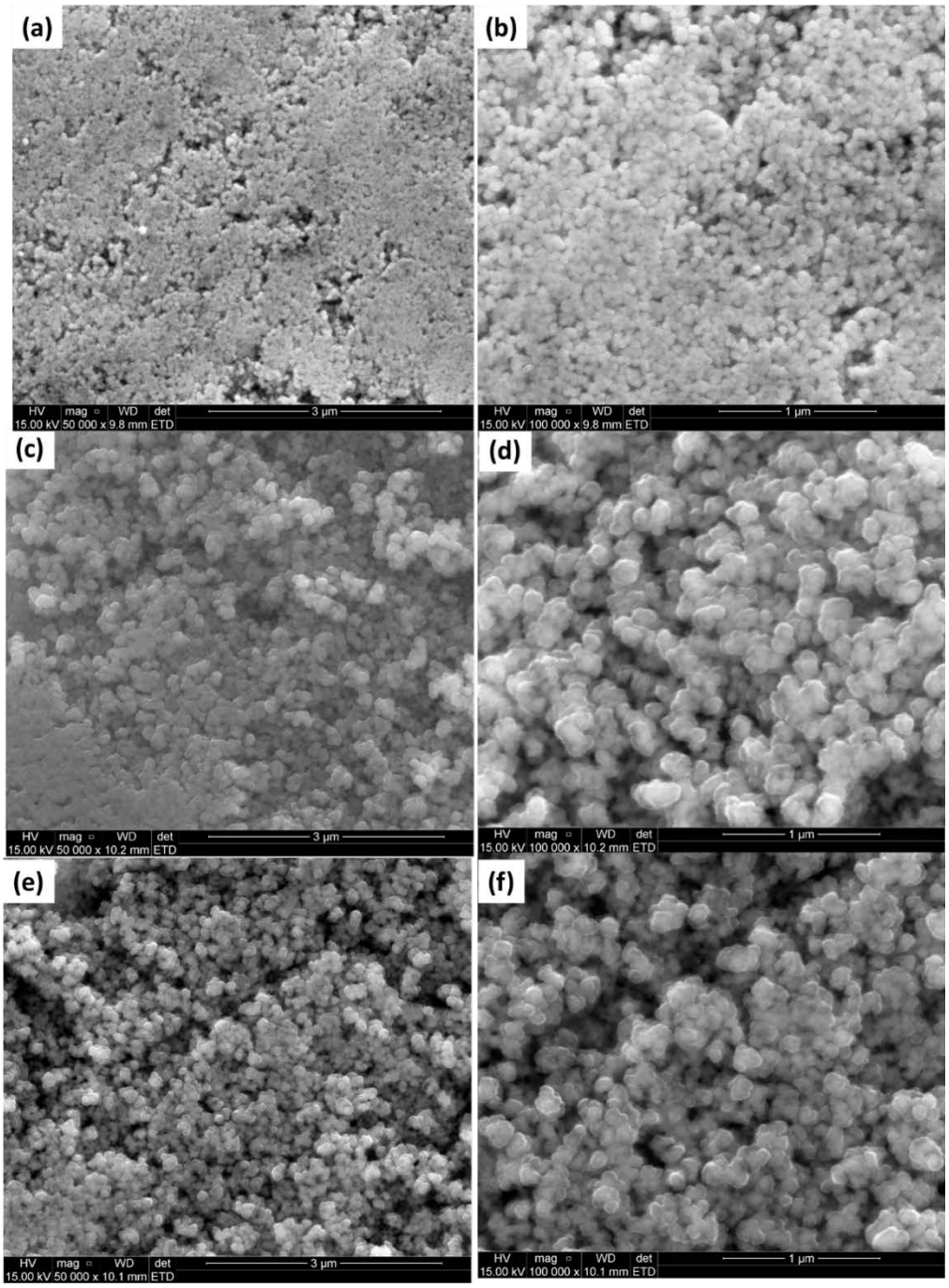

Figure 4. 20: SEM micrograph (a,b) pristine ZnO, (c,d) ZnO:Sn(2%), (e,f) ZnO:Sn(5%) at low and high magnification respectively.

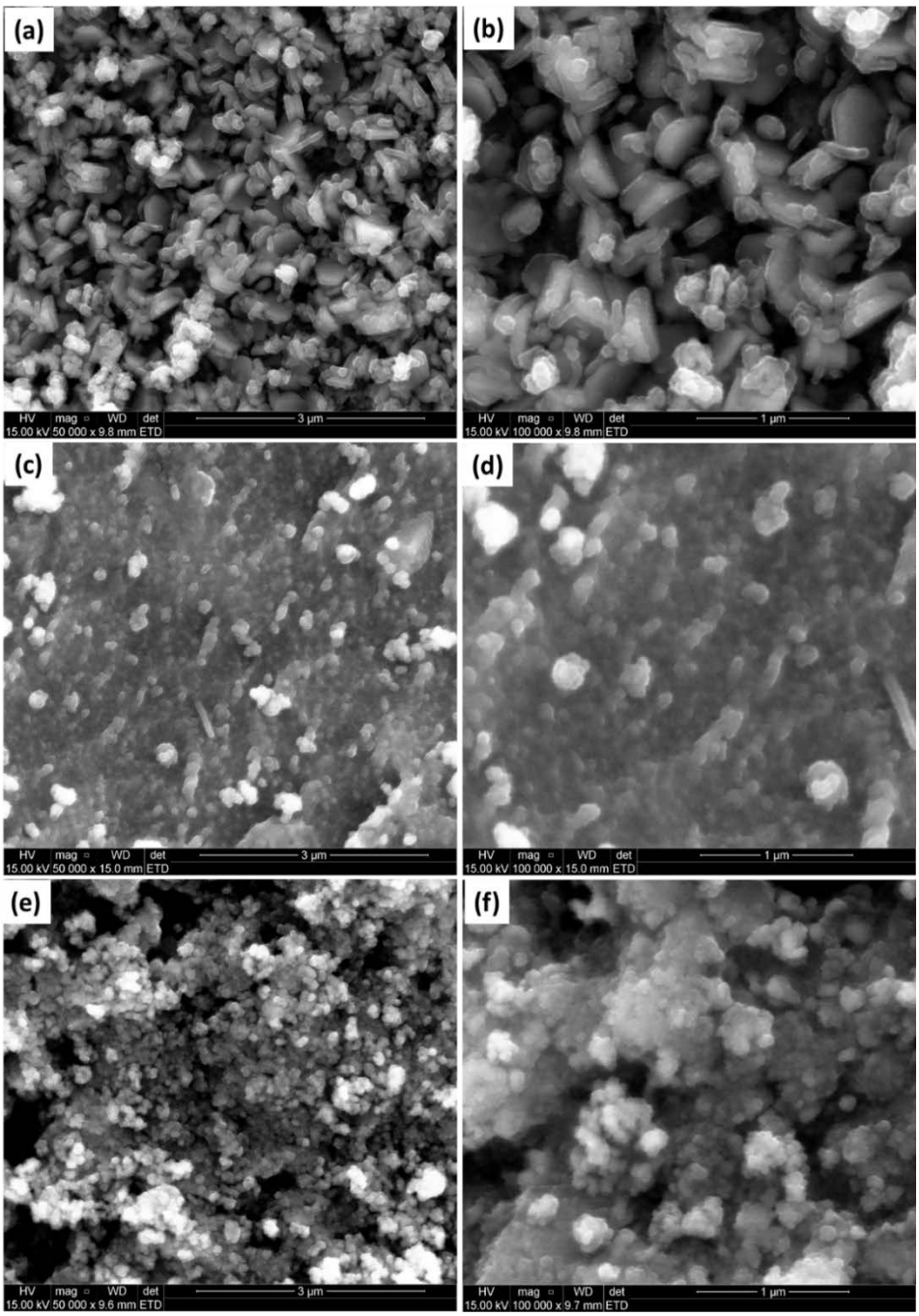

Figure 4. 21: SEM micrograph (a,b) ZnO:Sn(10%), (c,d) ZnO:Sn(15%), (e, f) ZnO:Sn(20%) at low and high magnification respectively.

The SEM images of the prepared composites are shown in Figs 4.22 and 4.23. The images illustrate the occurrence of particles in two different morphologies. Figs 4.22 (a-d) show the results of ZTO-ZnO composite oxides at lower Sn concentration with different fractions of ZTO and ZnO. The images show the admixture of cubic and rectangular particles for the composites prepared using 2 and 5% Sn concentration; and more compact images with spherical morphology and no distinct separable edge was observed in the composite prepared with 10% Sn concentration. The composite prepared using 15, 20 and 30% Sn concentration shows the emergence of more cubic and granular particles. The granular particles could possibly be ZnO nanogranules, while the rectangular shaped particles could be ZTO particles.

During the synthesis of ZTO, Zn^{2+} ions from the ZnO surfaces reacted with Sn^{2+} ions available in the precursor solution forming ZTO compounds [62]. It could be seen that the morphology of the composite formed is influenced by the concentration of the precursor (Sn) used. At low concentration of Sn, the possible amount of ZTO formed were low. When higher concentration of a tin solution was used for the synthesis of the nanocomposite, more of the ZnO were transformed to the nanocomposite with ZTO. Furthermore, a change in morphology was also observed with the dominance of nanoparticles with cubic morphology. This was due to the higher concentration of Sn^{2+} in the solution, which resulted in increased consumption of Zn^{2+} ions released from ZnO, exposing the surfaces to the Sn^{2+} solution to further form ZTO [3]. Hence, the increase in un-uniform cubic ZTO nanoparticles.

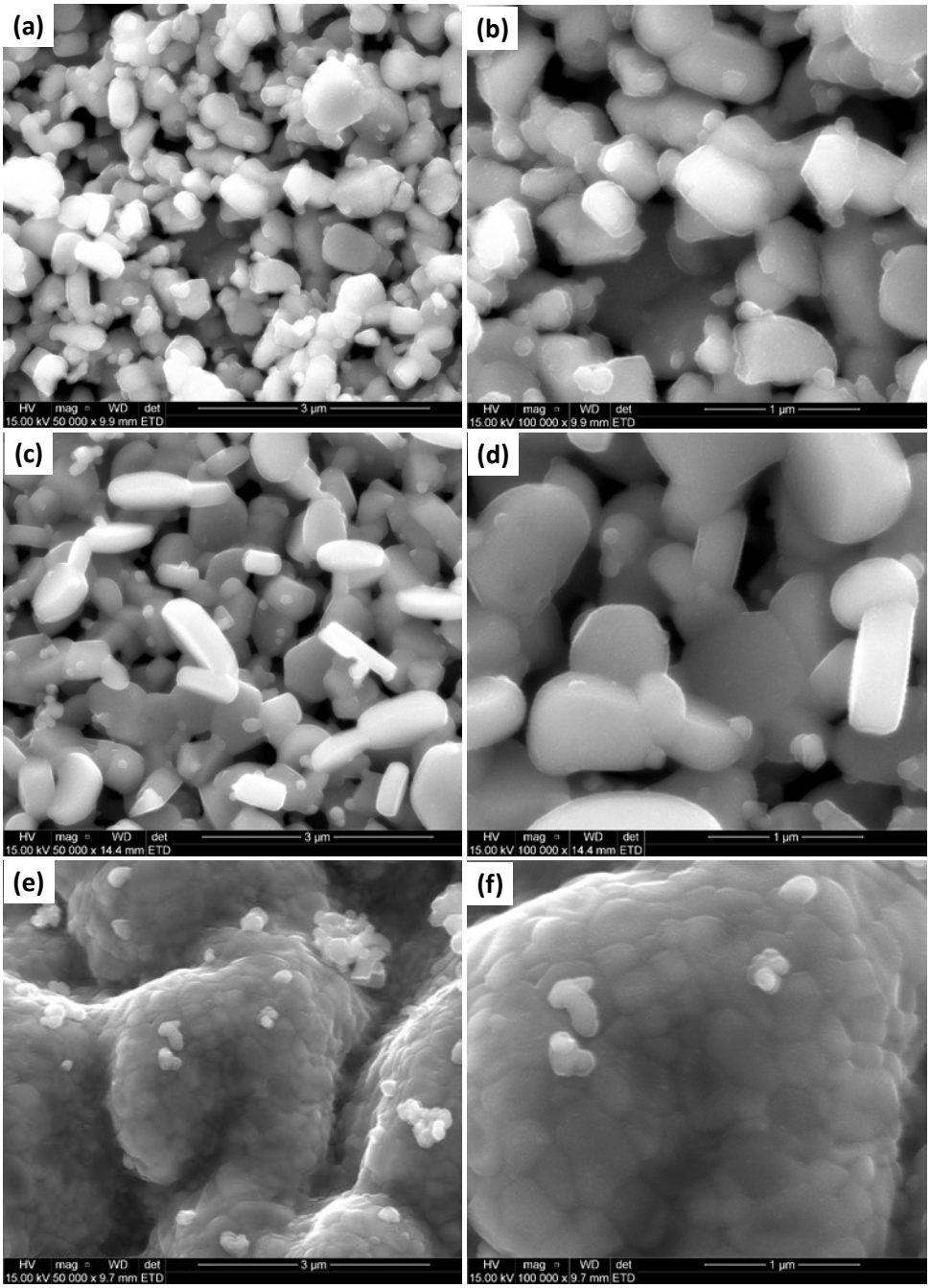

Figure 4. 22: SEM micrograph (a, b) ZTO-ZnO:Sn(02%), (c,d) ZTO-ZnO:Sn(05%) (e,f) ZTO-ZnO:Sn(10%) at low and high magnification respectively.

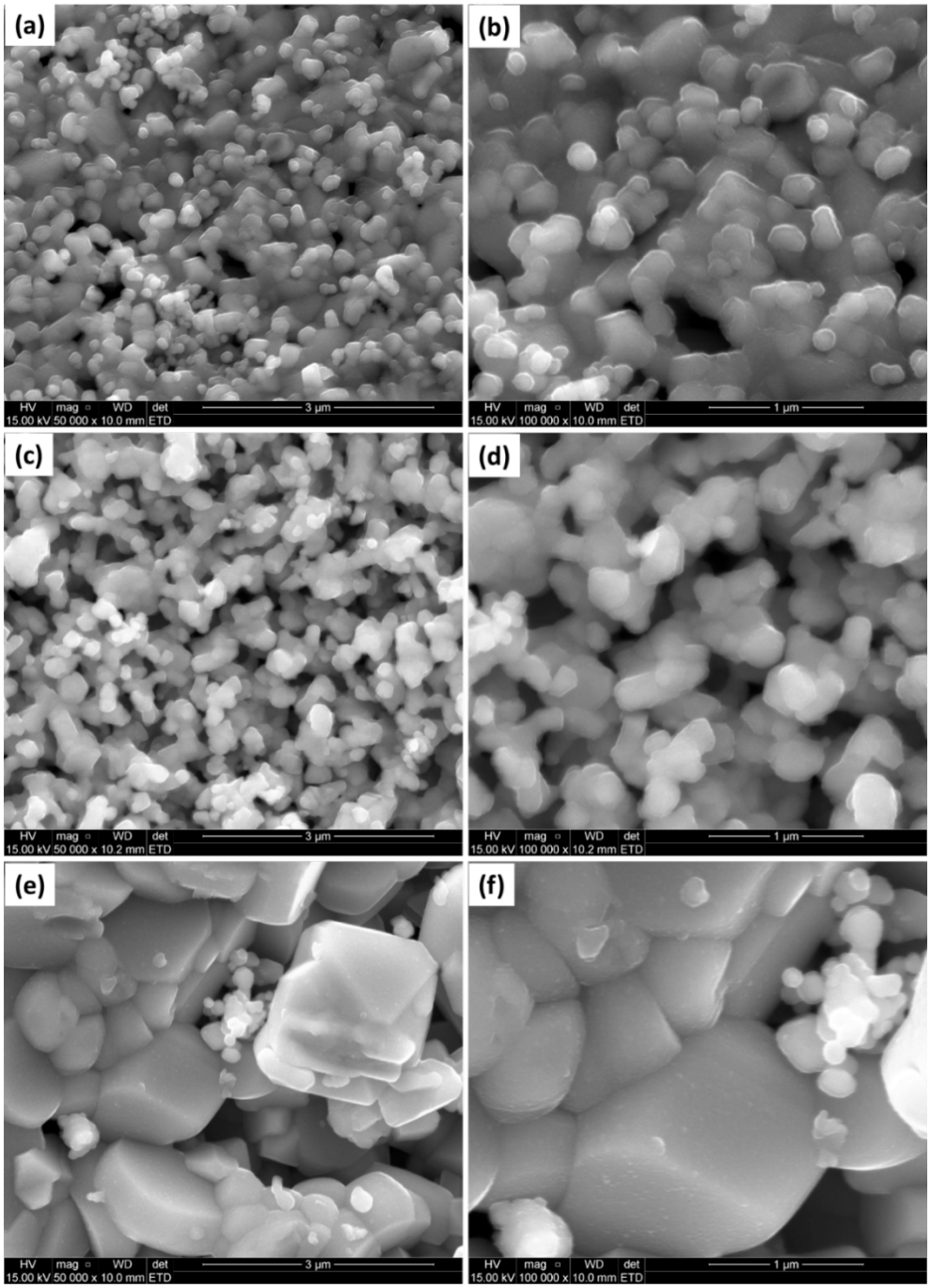

Figure 4. 23: SEM micrograph (a,b) ZTO-ZnO:Sn(15%), (c,d) ZTO-ZnO:Sn(20%) (e,f) ZTO-ZnO:Sn(30%) at low and high magnification respectively.

Fig 4.24 (a-b) show the SEM images of graphitic carbon nitride at low and high magnification, while Fig 4.24 (c-f) are the composites of ZTO-ZnO incorporated with graphitic carbon nitride. The images showed that the g-C_3N_4 are composed of many irregular nanosheets, which are characteristic of g-C_3N_4 [63-65]. The SEM images of g-C_3N_4/ZTO-ZnO(20%) and of g-C_3N_4/ZTO-ZnO(30%). Fig 4.24 (c-f) confirmed the co-existence of g-C_3N_4 nanosheets and ZTO-ZnO nanocubes. The ZTO-ZnO nanocubes were deposited on the surface of the g-C_3N_4, indicating the formation of ternary g-C_3N_4/ZTO-ZnO composites [64]. The surface of g-C_3N_4 became relatively rough after incorporation of ZTO-ZnO nanocubes.

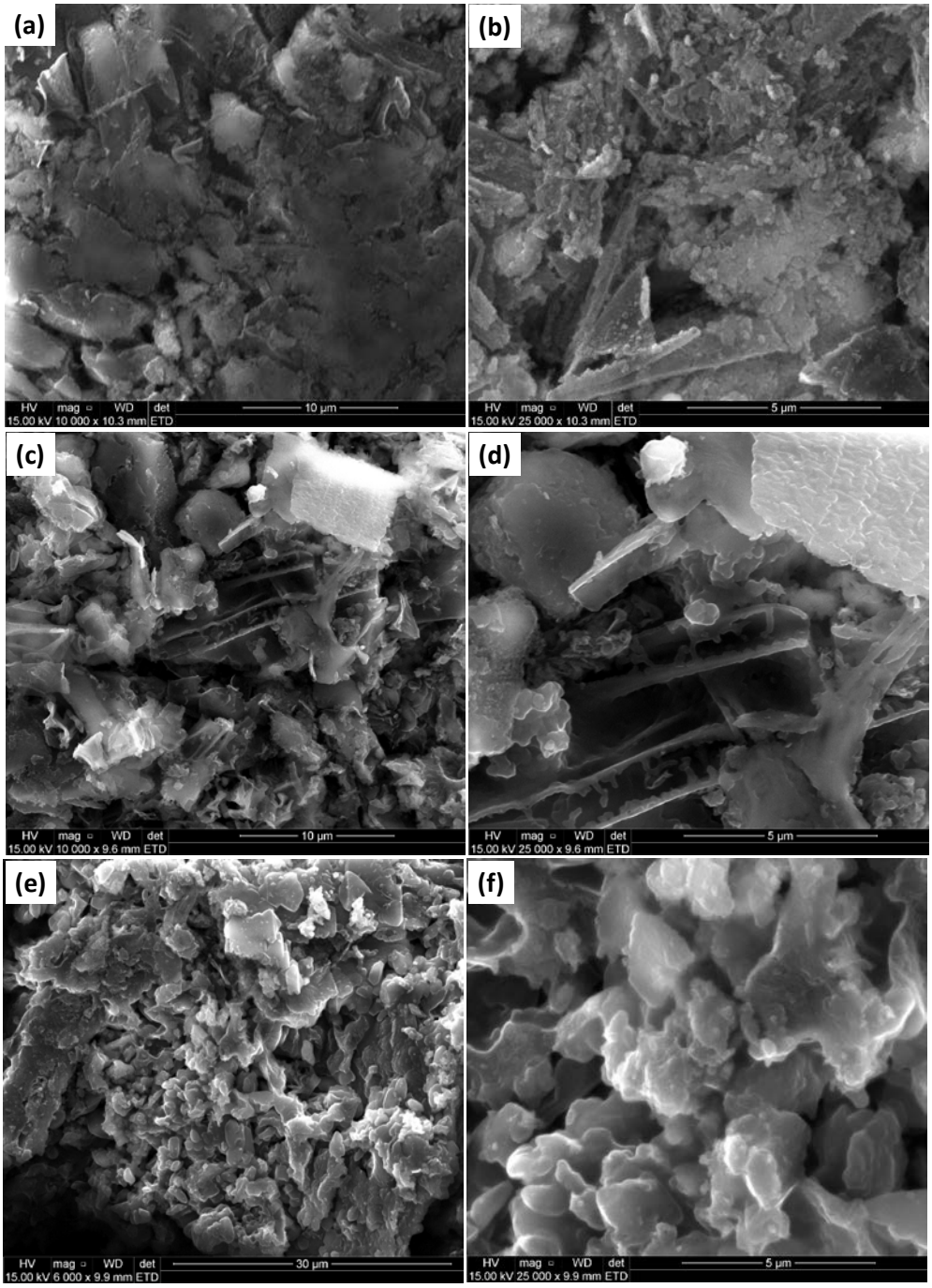

Figure 4. 24: SEM micrograph (a, b) gC_3N_4, (c,d) gC_3N_4/ZTO-ZnO@20%, (e,f) gC_3N_4/ZTO-ZnO@30% at low and high magnification respectively.

4.3.2. Transmission Electron Microscopy

Figs 4.25 and 4.26 show the TEM micrographs of pristine ZnO, Sn doped ZnO nanoparticles and their corresponding high-resolution TEM. The micrographs of the nanoparticles at all concentrations presents spherical nanoparticles, similar to the morphology observed in the SEM. As the concentration of the Sn ion increased, a disappearance in the distict edge of the particles occurred, due to agglomeration and this impeded on the size estimation from the TEM images. This observation could be attributed by the role of Sn^{2+} ion surface changes on ZnO lattice plans. At higher concentration of Sn, the adsorption of Sn^{2+} filling the ZnO growth sites suppresses the growth rate along c-axis, subsequently resulting in the formation of particles with a more granular forms, in which some black spots/regions or particles might suggest the presence of the Sn-ions [4, 66].

Further structural analysis by HRTEM images shows Sn-ions expressed by dark marks in Fig 4.25 (b,d and f) and 4.26 (b,d and f). The uniform fringes with a lattice spacing of 0.24 nm corresponding to (1 0 1) planes of ZnO were observed [67]. The lattice fringes spacing increased from 0.2477 nm to 0.2479 nm, and this expansion of fringes has been reported to be caused by the defects possibly due to electric stress that may exist from Sn doping in the ZnO matrices [68].

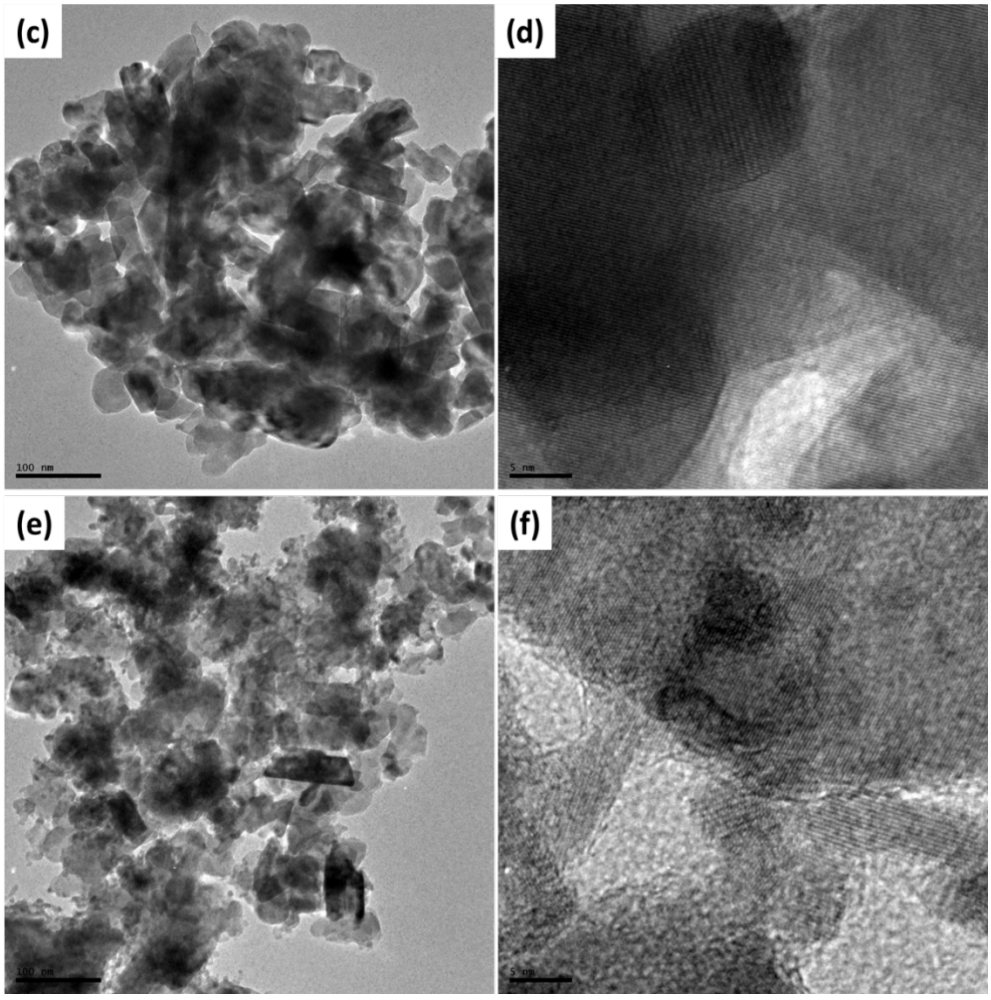

Figure 4. 25: TEM micrograph (a,b) pristine ZnO, (c,d) ZnO:Sn(02%), (e,f) ZnO:Sn(05%) at low and high magnification respectively.

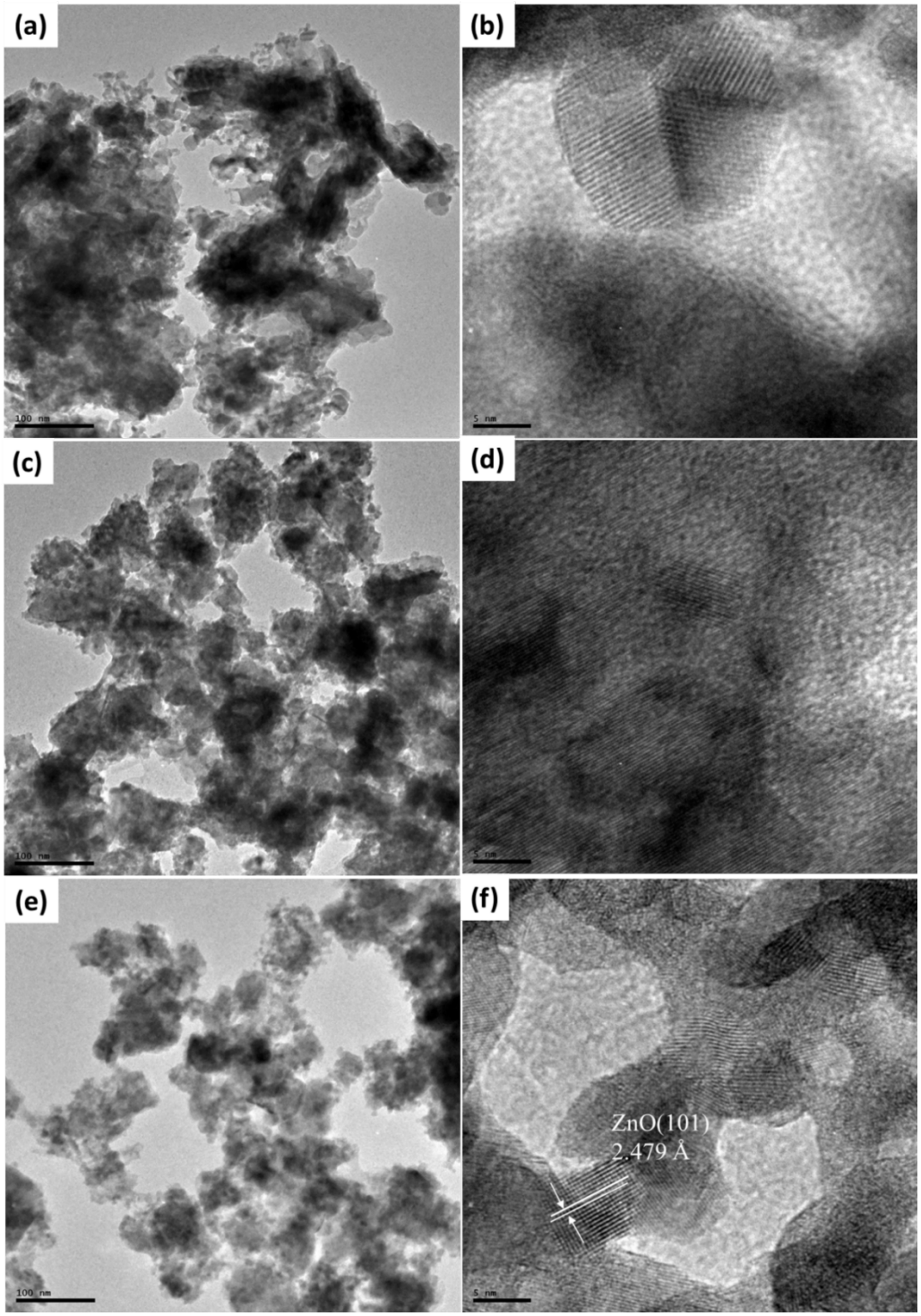

Figure 4. 26: TEM micrograph (a,b) ZnO:Sn(10%), (c,d) ZnO:Sn(15%), (e, f) ZnO:Sn(20%) at low and high magnification respectively.

Nanocomposite of ZTO-ZnO nanoparticles are presented in Fig 4.27 and 4.28. Two different morphologies are observed, and this compliments the SEM results of the ZTO-ZnO composite. The two morphologies identified are the rectangular shaped particles for the ZnO:Sn(2%), which tend to decompose into an admixture of cubic and spherical

morphologies. The ZTO were formed by the reaction of the ZnO and SnO_2, with the dissolution of the crystalline structure and its subsequent re-precipitation in the system wherein Sn^{2+}in the solution reacts with Zn^{2+} supplied from ZnO nanospheres forming ZTO as shown in Fig 4.28 and 4.29 [62, 69].

In the HRTEM images presented in Fig 4.27 (d) and 4.28 (d), the lattice fringes of ZTO-ZnO, with inter-planer distance of 0.50 nm, corresponding well with (1 1 1) planes, and 0.28 nm which corresponds to the (1 0 0) planes of hexagonal ZnO, as shown (Fig 4.28 (d)) further confirm the presence of Zn_2SnO_4 and ZnO phases in the nano-catalyst. This confirmed the results obtained from XRD studies and the existence of mixed ZnO and ZTO phases in the same system.

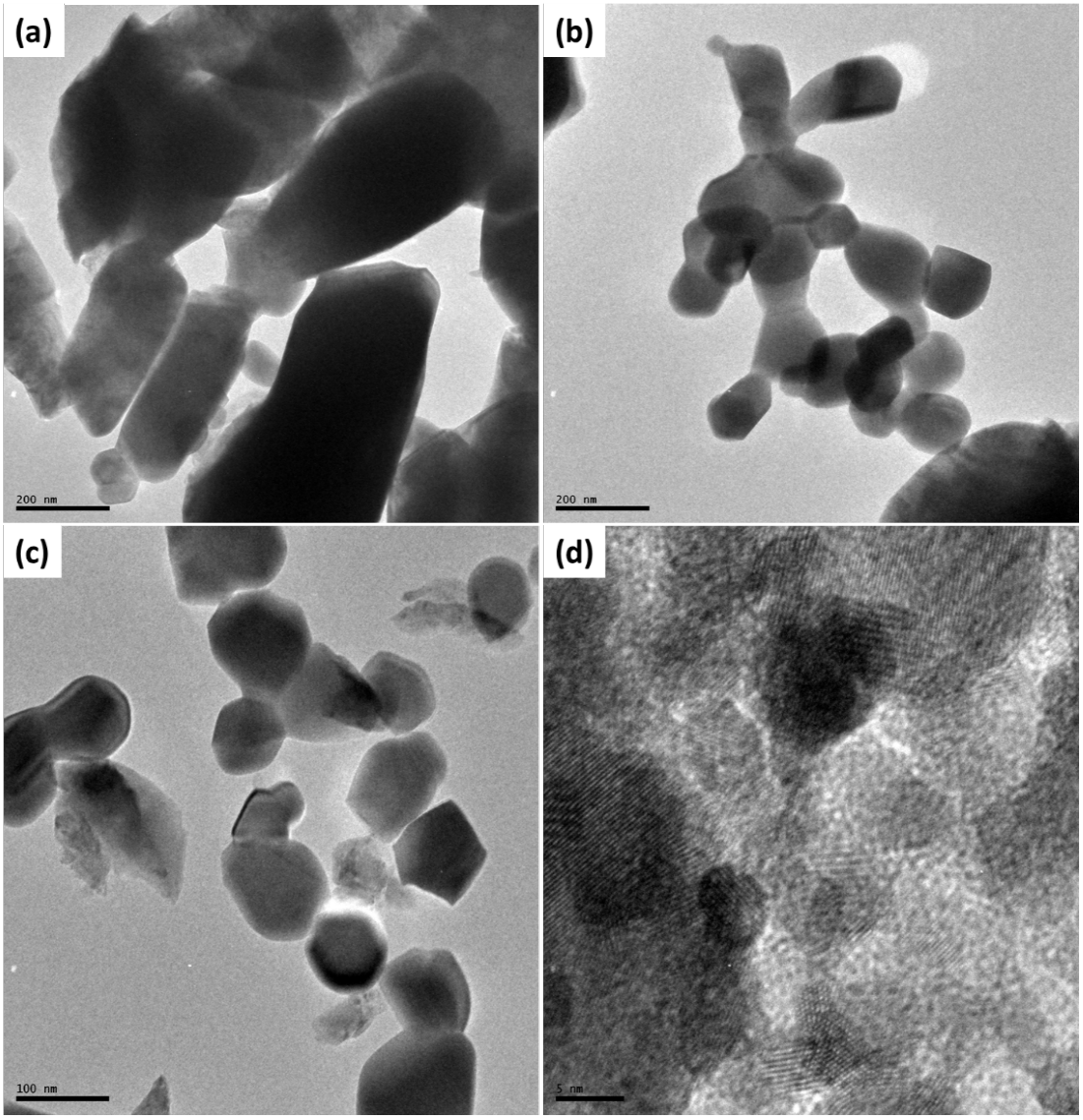

Figure 4. 27: TEM micrograph (a,) ZTO-ZnO:Sn(02%), (b) ZTO-ZnO:Sn(05%) (c) ZTO-ZnO:Sn(10%), (d) HRTEM ZTO-ZnO(10%).

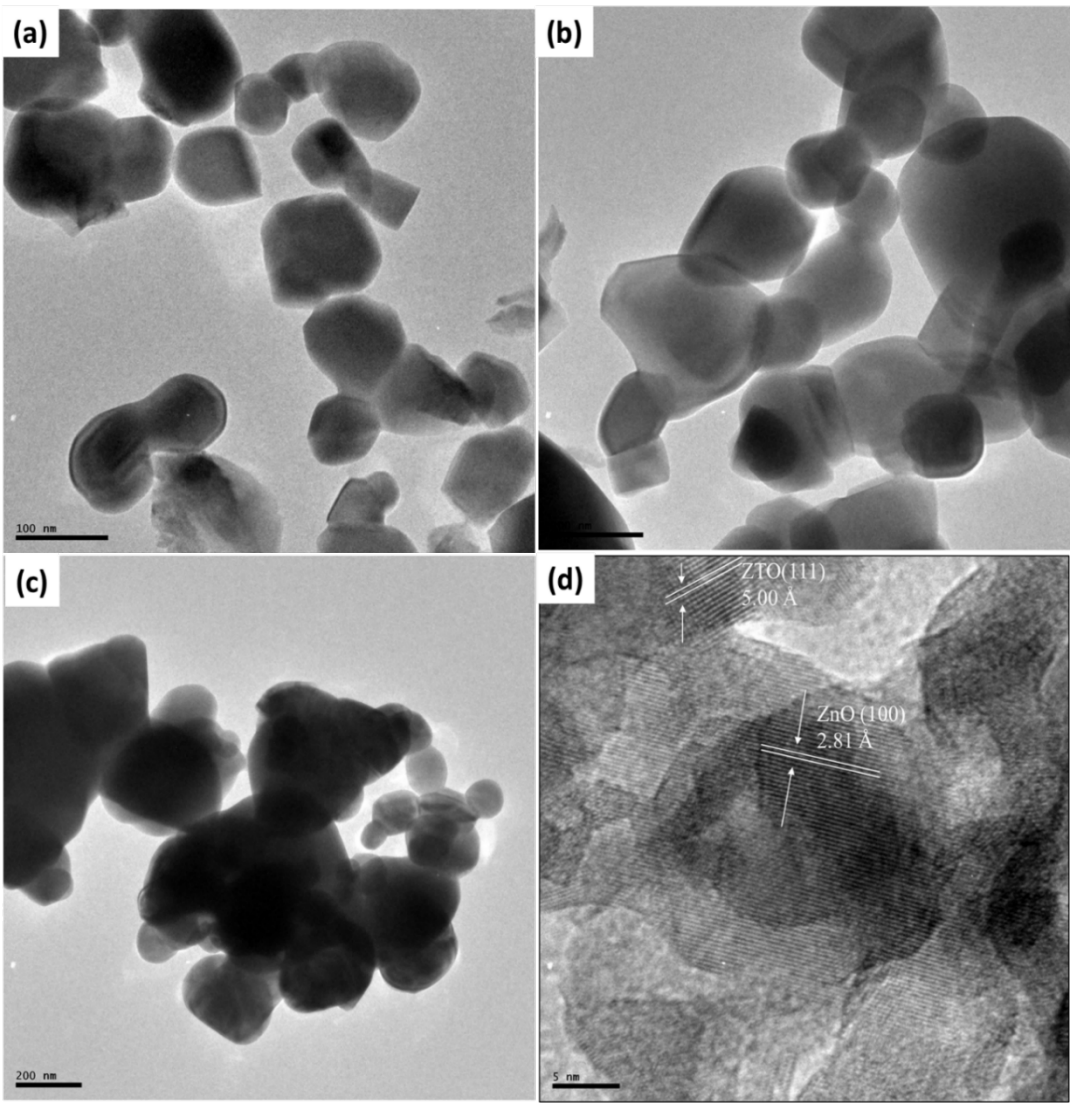

Figure 4. 28: TEM micrograph (a) ZTO-ZnO:Sn(15%), (b) ZTO-ZnO:Sn(20%) (c) ZTO-ZnO:Sn(30%, (d) HRTEM ZTO-ZnO(30%).

The TEM image of pure g-C_3N_4 in Fig 4.29 (a) consists of nanosheets, which are characteristic of gC_3N_4 [70, 71]. Fig 4.30 (b to e) at both at lower and higher magnifications clearly reveal the differences in the morphology of the materials. TEM images of the g-C_3N_4/ ZTO-ZnO show that the heterostructure consists of g-C_3N_4 nanosheets decorated with very small particles which could be the ZTO-ZnO [71]. The higher magnification images (c) and (e) reveal that g-C_3N_4/ZTO-ZnO heterojunction system was formed.

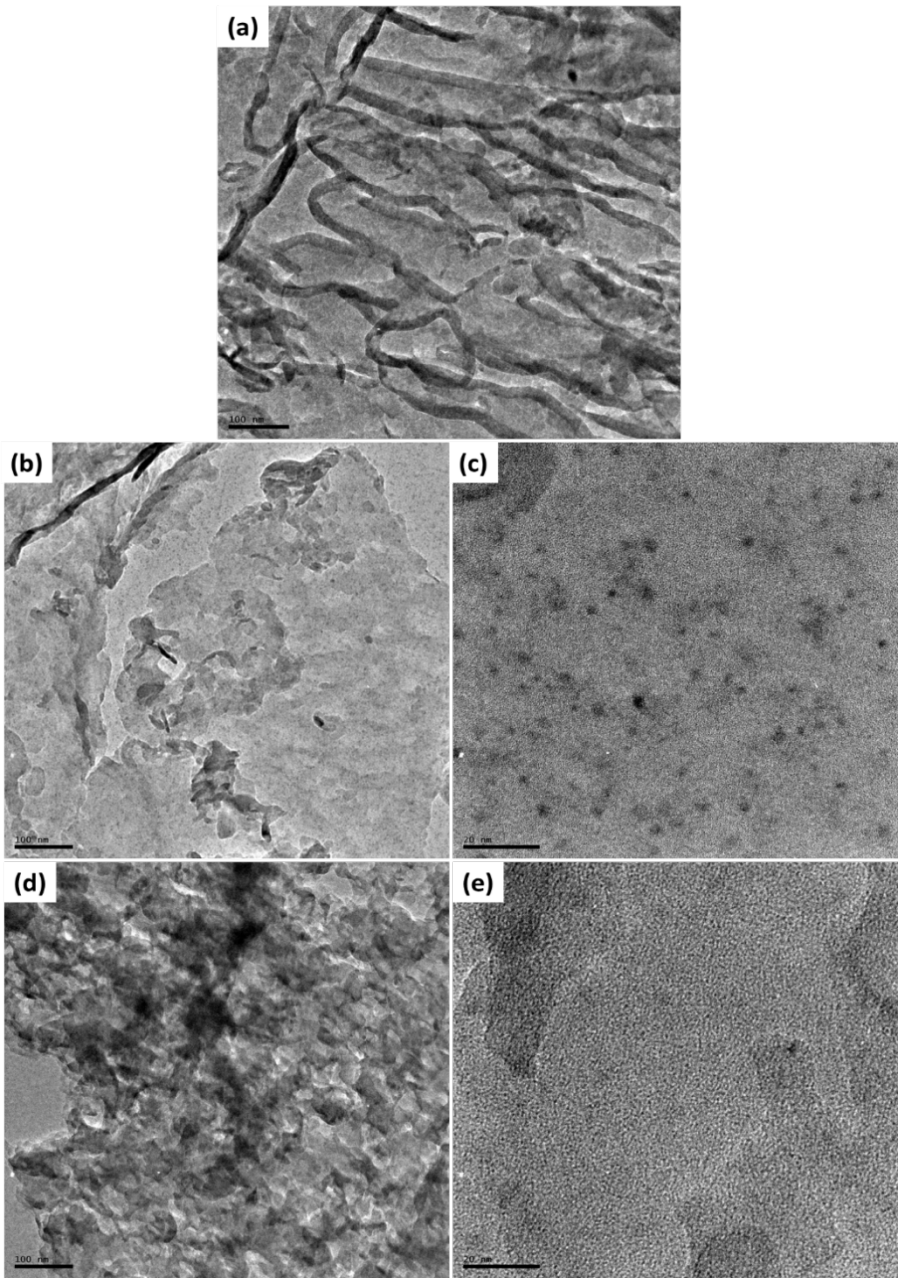

Figure 4. 29: TEM micrograph (a) gC_3N_4, (b,c) gC_3N_4/ZTO-ZnO(20%), (d,e) gC_3N_4/ZTO-ZnO(30%).

4.5. Photocatalytic studies

4.5.1. The effects of solution pH on the Cr(VI) reduction

The chemistry of Cr(VI) is pH dependent; thus, changes with the change in solution pH, which usually affects the removal or reduction of Cr(VI). This might be due to the changes that occur in the oxidation states while in solution and the charge densities of the photocatalysts. Therefore, 10 mg/L of Cr(VI) was investigated using g-C_3N_4/ZTO-ZnO@20 and g-C_3N_4/ZTO-ZnO@30 separately using the Cr(VI) dosage of 2 g/L, and the initial solution pH was varied from 2 to 8. At the initial stage, in both cases, the catalysts removed very small fraction of Cr(VI) in all pH range. However, increase in irradiation time increases the degradation rate of Cr(VI) to Cr(III) up to 120 min which is considered complete irradiation time with almost 100% reduction rate (Fig. 4.30a and b). Cr(VI) was gradually removed at the different time intervals using both g-C_3N_4/ ZTO-ZnO@20 and g-C_3N_4/ ZTO-ZnO@30 photocatalysts (Fig. 4.30a and b). The pH 2 solution has the highest removal of Cr(VI) at 99.2 and 72% for pH 4, it was 85.6 and 50%, pH 6 was 57.2 and 38%, and for pH 8, the percentage reduction was found to be 35 and 25% respectively.

The observed similarity in the reactions of these two different catalysts suggests that the photocatalytic removal of Cr(VI) increased with decrease in solution pH. This might be due to an increased potential difference between the conduction band of the catalysts and Cr(VI)/Cr(III) as well as the anionic-type adsorption of Cr(VI) on to the surface of both catalysts [72]. Also, the thermodynamic driving force for the reduction of Cr(VI) is related to the potential difference between the conduction band of the catalysts and the Cr(VI) ion[73]. The reduced removal rate observed at higher pH may also be attributed to the deposition of $Cr(OH)_3$ on the surface of the catalysts which could be ascribed to the adsorption of Cr(VI) on to the surface of catalysts and its subsequent redox reaction. Thus, photocatalytic reduction of Cr(VI) is possible either by direct capturing of photo-generated electrons or by indirect receiving of electrons from the surface of catalysts or even concurrently[73, 74].

The speciation of Cr^{3+} depends on the solution pH, and hydrolysed $Cr(OH)_3$ is favoured at high solution pH [74]. The observed reduction efficiency obtained at pH 2 using g-C_3N_4/ ZTO-ZnO@20 (Fig.4.30a) was higher compared to g-C_3N_4/ ZTO-ZnO@30 (Fig4.30b). Consequently, g-C_3N_4/ ZTO-ZnO@20 was chosen for further Cr(VI) photocatalytic studies.

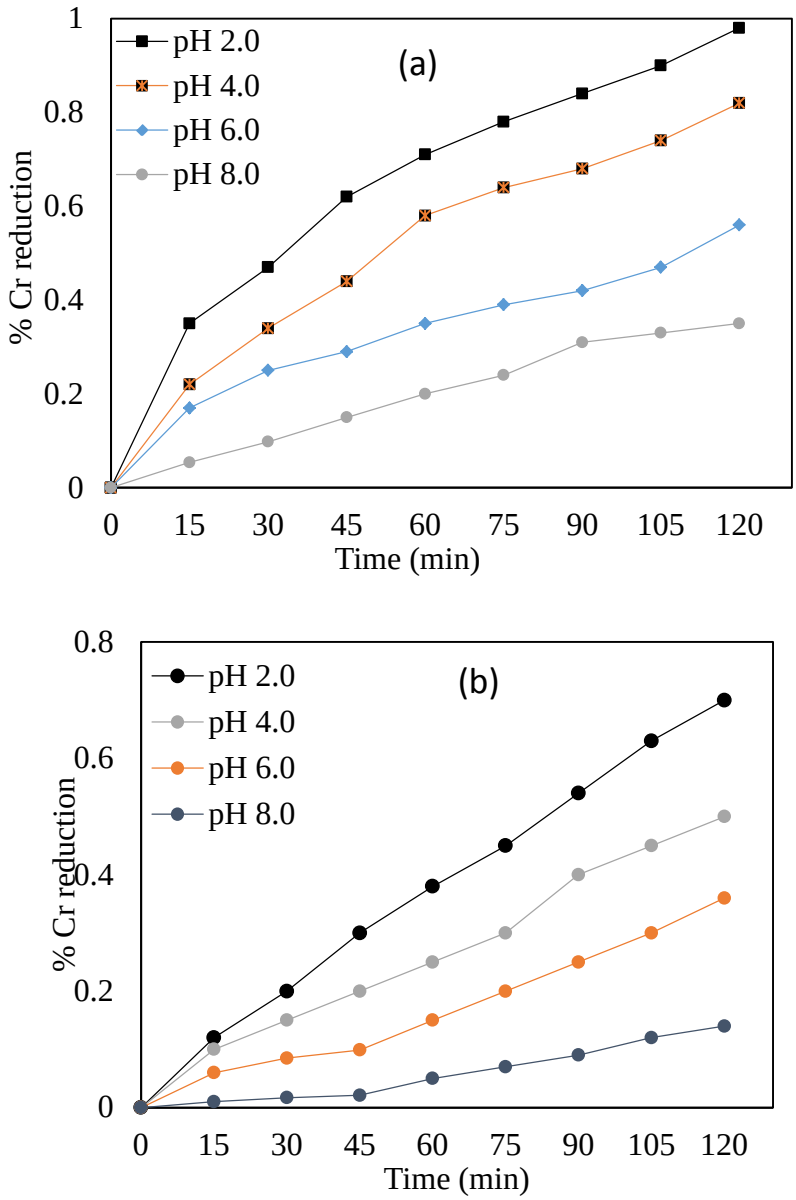

Figure 4. 30: Effect of solution pH on the reduction of Cr(VI) using (a) g-C_3N_4/ ZTO-ZnO@20 and (b) g-C_3N_4/ ZTO-ZnO@30 (conc of photocatalyst =2 g/L, Cr(VI)=10 mg/L)

4.5.2. Effect of photocatalyst (g-C_3N_4/ ZTO-ZnO@20) dosage

Figure 4.31 presents the effect of varying concentration (0.5 to 2 g) of g-C_3N_4/ ZTO-ZnO@20 on the reduction of Cr(VI) to Cr(III) in aqueous solution. The removal rate of chromium increased with increase in the catalyst dosage. Consequently, the highest chromium removal percentage was found to be 99.2% at photocatalyst loading of 2 g/ L. As the g-C_3N_4/ ZTO-ZnO@20 loading was increased from 0.5 to 2 g/L, the percentage of chromium removal also increased from 64 to 93.8% at the optimum irradiation time.

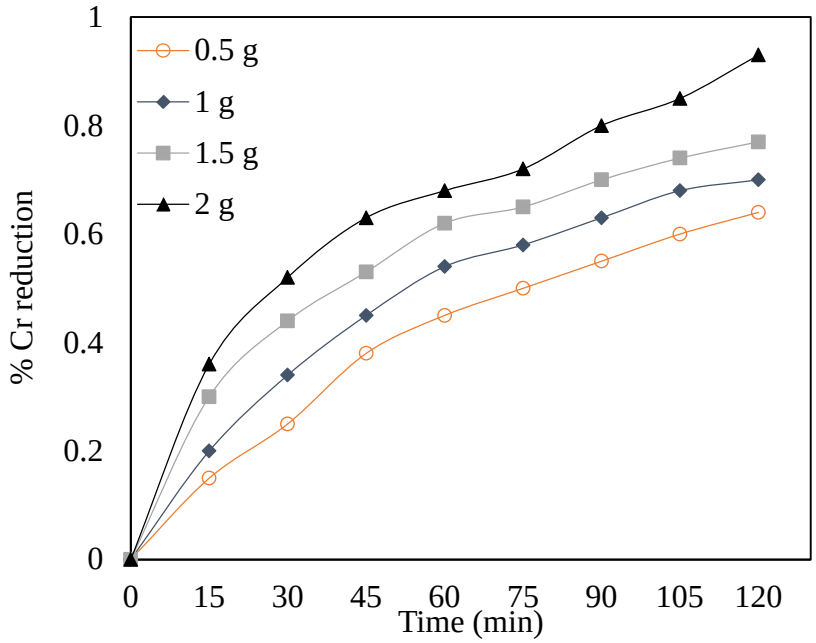

Figure 4. 31: The effect of catalyst loading on the photoreduction of Cr(VI) using g-C_3N_4/ ZTO-ZnO@20 as photocatalyst.

4.5.3. Effect of initial concentration of Cr(IV) on the rate of reduction

The effect of initial concentrations of Cr(VI) was investigated within the range of 10 to 150 ppm and at the optimal conditions of pH 2 and 2 g/L of g-C_3N_4/ ZTO-ZnO@20, and the results obtained are presented in Fig. 4.32. The graph showed that the irradiation time required for complete removal of Cr(VI) under the visible light source was extended as the initial Cr(VI) concentration increased. This observation could be rationalized according to Beer–Lambert's law: as Cr(VI) concentration increased, the path length of photons entering into the reaction mixture decreased, and only fewer photons could reach the catalyst's surface[75].

Therefore, the availability of active sites will be reduced, since the incident intensity, concentration of catalyst and irradiation time are constant. In addition, an increase in Cr(VI) concentrations can lead to the saturation of the limited number of accessible active sites on the photocatalyst surface and/or deactivation of the active sites of the catalyst, which could results in a reduction in the photo reduction rate[75, 76]. The photocatalytic reaction kinetics of Cr(VI) has often been modelled with the pseudo-first and second order kinetics models equation, which also cover the adsorption properties of the Cr(VI) on the photocatalyst surface. This model is expressed in equation (4.3) and (4.4).

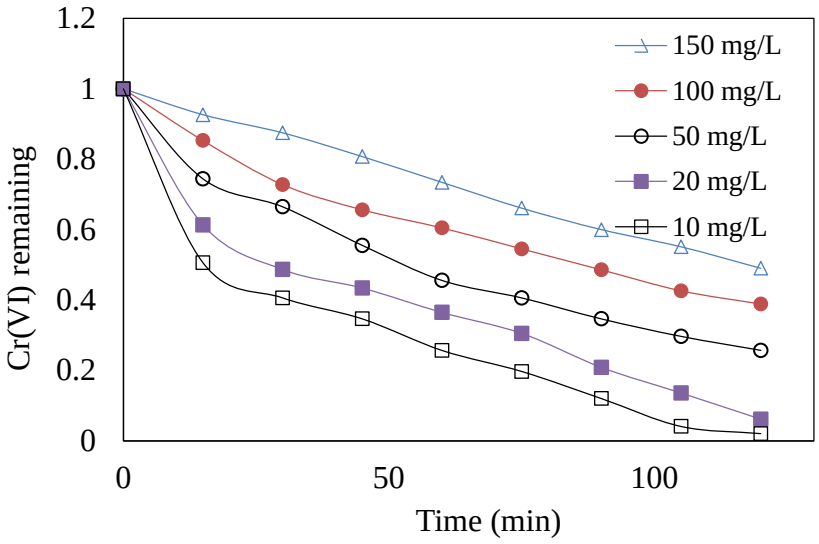

Figure 4. 32: (a) Effect of Cr(VI) concentration on to g-C_3N_4/ ZTO-ZnO@20, (dosage: 2 g/L, irradiation time: 120 min, pH: 2)

Thus, the pseudo-first and second order, kinetics model equations can be expressed in the equation 4.3 and 4.4 respectively:

$$\log(q_e - q_t) = \log q_e - \frac{k_1}{2.303}t \qquad (4.3)$$

$$\frac{t}{q_t} = \frac{1}{k_2 q_e} + \frac{1}{q_e}t \qquad (4.4)$$

where q_e and q_t are the degradation capacity (mg/g) of solute at equilibrium and at time t (min), respectively, k_1 (min^{-1}) and k_2 (g/mg·min) are the rate constants of the pseudo-first and pseudo-second order degradation processes respectively.

The results obtained by comparing their correlation coefficient (R^2) values (Fig. 4.33) suggested that pseudo-first order model well described the photocatalytic activity of g-C_3N_4/ ZTO-ZnO@20 on the reduction of Cr(VI) to Cr(III) compared to pseudo- second order kinetics model. The reaction rate constants (k) for the photocatalytic reduction of Cr(VI) were evaluated from experimental data using the linear regression analysis method. The constants k_1 and k_2 (first and second order reaction rate constants) were obtained as 19.6 and 1.4 g/mg.min respectively (Table 4.5). A non-linear regression method was used to calculate the best values of model constants. A high correlation coefficient (R^2=0.999) confirms the validity of the pseudo-first order model. This is an indication that the photoreduction of

Cr(VI) occurred mainly on the surface of the catalyst and the photoreduction step is the limited step and also determines the overall reaction rate[77]. Also, the increase in overall rate constant *k* with an increase in initial Cr(VI) concentration could be due to the transition from the kinetics control regime at low concentrations to mass transfer limitations at high concentrations. These results were similar to earlier reported studies [78, 79].

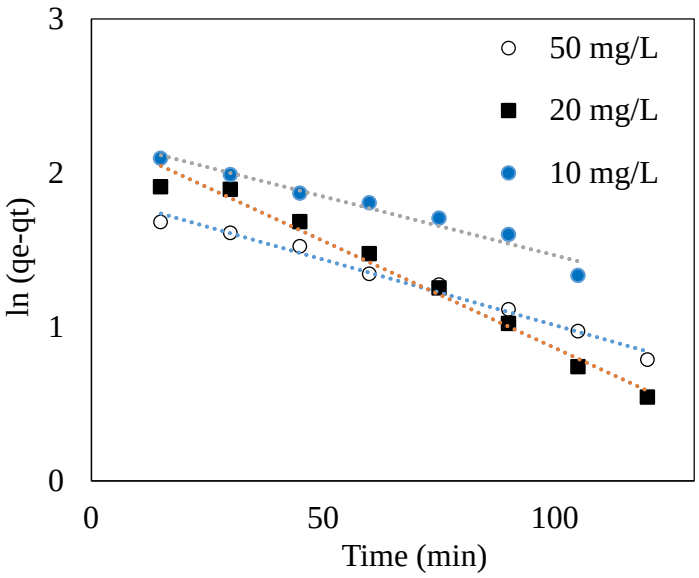

Figure 4. 33: (a) Pseudo first order model for Cr(VI) photo degradation by g-C_3N_4/ ZTO-ZnO@20 (dosage: 3 g/L, irradiation time: 120 min, pH: 2)

Table 4. 5: Kinetics parameters for Cr onto g-C_3N_4/ ZTO-ZnO@20 photocatalysts

	Pseudo-first-order model parameter			Pseudo-second-order model parameter		
Co (mg/L)	k_1 x10^{-2} (g/mg.min)	*a* (mg/g)	R^2	q_e (mg/g)	k_2 10^{-2} (g/mg.min)	R^2
10	1.77	9.53	0.995	14.5	5.1	0.787
20	3.20	9.51	0.998	17.2	3.6	0.765
50	19.6	6.46	0.988	13.1	1.4	0.697

REFERENCE

1. Molefe, F.V., et al., Phase formation of hexagonal wurtzite ZnO through decomposition of Zn(OH)2 at various growth temperatures using CBD method. Optical Materials, 2015. **46**: p. 292-298.
2. Wu, C., et al., Synthesis of Sn-doped ZnO nanorods and their photocatalytic properties. Materials Research Bulletin, 2011. **46**(7): p. 1107-1112.
3. Sheini, F.J., et al., Observation of Photoconductivity in Sn-Doped ZnO Nanowires and Their Photoenhanced Field Emission Behavior. The Journal of Physical Chemistry - Part C, 2010. **114**(9): p. 3843-3849.
4. Siva, N., et al., Synthesis, structural, optical and photocatalytic behavior of Sn doped ZnO nanoparticles. Materials Science & Engineering: B, 2020. **253**: p. N.PAG-N.PAG.
5. Thandavan, T.M.K., et al., Enhanced photoluminescence and Raman properties of Al-doped ZnO nanostructures prepared using thermal chemical vapor deposition of methanol assisted with heated brass. PLoS One, 2015. **10**(3): p. e0121756.
6. Tsay, C.-Y., et al., Effect of Sn-doped on microstructural and optical properties of ZnO thin films deposited by sol–gel method. Thin Solid Films, 2008. **517**(3): p. 1032-1036.
7. Kripal, R., et al., Photoconductivity and photoluminescence of ZnO nanoparticles synthesized via co-precipitation method. Spectrochimica Acta Part A: Molecular and Biomolecular Spectroscopy, 2011. **79**(5): p. 1605-1612.
8. Ben Ali, M., et al., Hydrothermal synthesis, phase structure, optical and photocatalytic properties of Zn2SnO4 nanoparticles. Journal of colloid and interface science, 2015. **457**: p. 360-369.
9. Suryanarayana, C. and M.G. Norton, X-Ray Diffraction: A Practical Approach. 1998: Springer Science & Business Media.
10. Mustapha, S., et al., Comparative study of crystallite size using Williamson-Hall and Debye-Scherrer plots for ZnO nanoparticles. Advances in Natural Sciences: Nanoscience and Nanotechnology, 2019. **10**(4): p. 045013-045013.
11. Kibasomba, P.M., et al., Strain and grain size of TiO2 nanoparticles from TEM, Raman spectroscopy and XRD: The revisiting of the Williamson-Hall plot method. Results in Physics, 2018. **9**: p. 628-635.

12. Vinoth, S., P. Mary Rajaitha, and A. Pandikumar, In-situ pyrolytic processed zinc stannate incorporated graphitic carbon nitride nanocomposite for selective and sensitive electrochemical determination of nitrobenzene. Composites Science & Technology, 2020. **195**: p. N.PAG-N.PAG.
13. Vinoth, S., R. Ramaraj, and A. Pandikumar, Facile synthesis of calcium stannate incorporated graphitic carbon nitride nanohybrid materials: A sensitive electrochemical sensor for determining dopamine. Materials Chemistry & Physics, 2020. **245**: p. N.PAG-N.PAG.
14. Jeronsia, J.E., et al., Hydrothermal synthesis of zinc stannate nanoparticles for antibacterial applications. Journal of Taibah University for Science, 2016. **10**(4): p. 601-606.
15. Baruah, S. and J. Dutta, Zinc stannate nanostructures: hydrothermal synthesis. Science & Technology of Advanced Materials, 2011. **12**(1): p. 1-N.PAG.
16. Fang, T., et al., Ultrasensitive photoelectrochemical determination of chromium(VI) in water samples by ion-imprinted/formate anion-incorporated graphitic carbon nitride nanostructured hybrid. Journal of hazardous materials, 2016. **312**: p. 106-113.
17. Venkappayya, D., THERMAL DECOMPOSITION OF THE COMPLEXES OF DITHIOCARBAMATE AND SUBSTITUTED THIOUREA WITH NI (II), ZN (II), CD (II), CR (III) AND CO (III). 1974.
18. Hill, J.O., J.P. Murray, and K.C. Patil, THE THERMOCHEMISTRY OF THE METAL DITHIOCARBAMATE AND XANTHATE COMPLEXES - A REVIEW UP-DATE. Reviews in Inorganic Chemistry, 1994. **14**(5): p. 363-387.
19. Onwudiwe, D. and A. Ekennia, Synthesis, characterization, thermal, antimicrobial and antioxidant studies of some transition metal dithiocarbamates. Research on Chemical Intermediates, 2017. **43**(3): p. 1465-1485.
20. Sharma, A.K., Thermal behaviour of metal-dithiocarbamates. Thermochimica acta, 1986. **104**: p. 339-372.
21. Cavell, K.J., J.O. Hill, and R.J. Magee, Standard enthalpy of formation of bis (diethyldithiocarbamato) copper (II) at 298 K and the copper–sulphur bond energy. Journal of the Chemical Society, Dalton Transactions, 1980(9): p. 1638-1640.
22. Breviglieri, S.T., E.T. Cavalheiro, and G.O. Chierice, Correlation between ionic radius and thermal decomposition of Fe(II), Co(II), Ni(II), Cu(II) and Zn(II) diethanoldithiocarbamates. Thermochimica Acta, 2000. **356**(1): p. 79-84.

23. Macias, B., et al., Thermal stability of dithiocarbamates derived from α-amino acids with different metal ions. Thermochimica acta, 1993. **223**: p. 213-221.
24. Pike, R., et al., Preparation of zinc sulfide thin films by ultrasonic spray pyrolsis from bis (diethyldithiocarbamato) zinc (II). Thin solid films, 1993. **224**(2): p. 221-226.
25. Hrubaru, M., D.C. Onwudiwe, and E. Hosten, Synthesis and properties of ZnS nanoparticles by solvothermal and pyrolysis routes using the Zn dithiocarbamate complex as novel single source precursor. Journal of Sulfur Chemistry, 2016. **37**(1): p. 37-47.
26. Uekawa, N., et al., Synthesis of a stable sol of ZnO nanoparticles by low-temperature heating of Zn (OH) 2 in ethylene glycol containing Zn2+ ions. Journal of the Ceramic Society of Japan, 2010. **118**(1374): p. 96-101.
27. Li, P., et al., Investigation of the charge-transfer between Ga-doped ZnO nanoparticles and molecules using surface-enhanced Raman scattering: doping induced band-gap shrinkage. Frontiers in chemistry, 2019. **7**: p. 144.
28. Peksu, E. and H. Karaagac, Doping and annealing effects on structural, electrical and optical properties of tin-doped zinc-oxide thin films. Journal of Alloys and Compounds, 2018. **764**: p. 616-625.
29. Yung, K.C., H. Liem, and H. Choy, Enhanced redshift of the optical band gap in Sn-doped ZnO free standing films using the sol–gel method. Journal of Physics D: Applied Physics, 2009. **42**(18): p. 185002.
30. Vempati, S., J. Mitra, and P. Dawson, One-step synthesis of ZnO nanosheets: a blue-white fluorophore. Nanoscale research letters, 2012. **7**(1): p. 1-10.
31. Ye, J., et al., Fermi-level band filling and band-gap renormalization in Ga-doped ZnO. Applied Physics Letters, 2005. **86**(19): p. 192111.
32. Ilican, S., M. Caglar, and Y. Caglar, Sn doping effects on the electro-optical properties of sol gel derived transparent ZnO films. Applied Surface Science, 2010. **256**(23): p. 7204-7210.
33. Pauporté, T. and D. Lincot, Electrodeposition of semiconductors for optoelectronic devices: results on zinc oxide. Electrochimica Acta, 2000. **45**(20): p. 3345-3353.
34. Samanta, P.K., Band gap engineering, quantum confinement, defect mediated broadband visible photoluminescence and associated quantum States of size tuned zinc oxide nanostructures. Optik, 2020. **221**: p. 165337.

35. Aksoy, S., et al., Effect of Sn dopants on the optical and electrical properties of ZnO films. Optica Applicata, 2010. **40**(1): p. 7-14.
36. Acharya, A., et al., Growth and characterization of nano-structured Sn doped ZnO. Journal of molecular structure, 2012. **1022**: p. 8-15.
37. Serpone, N., Is the band gap of pristine TiO2 narrowed by anion-and cation-doping of titanium dioxide in second-generation photocatalysts? The Journal of Physical Chemistry B, 2006. **110**(48): p. 24287-24293.
38. Pham, T.A.T., et al., Facile preparation of ZnO nanoparticles and Ag/ZnO nanocomposite and their photocatalytic activities under visible light. International Journal of Photoenergy, 2020. **2020**.
39. Rajamohan, S., et al., Exploration of Ag decoration and Bi doping on the photocatalytic activity α-Fe2O3 under simulated solar light irradiation. The Canadian Journal of Chemical Engineering, 2018. **96**(8): p. 1713-1722.
40. Baruah, S., et al., Photoreactivity of ZnO nanoparticles in visible light: Effect of surface states on electron transfer reaction. Journal of Applied Physics, 2009. **105**(7): p. 074308.
41. Li, S., et al., A comparative study of photocatalytic degradation of phenol of TiO2 and ZnO in the presence of manganese dioxides. Catalysis Today, 2008. **139**(1-2): p. 109-112.
42. Cheng, B., et al., Individual Ohmic contacted ZnO/Zn 2 SnO 4 radial heterostructured nanowires as photodetectors with a broad-spectral-response: injection of electrons into/from interface states. Journal of materials chemistry c, 2014. **2**(10): p. 1808-1814.
43. Liu, R., et al., Preparation and photocatalytic property of mesoporous ZnO/SnO2 composite nanofibers. Journal of Alloys and Compounds, 2010. **503**(1): p. 103-110.
44. Che, H., et al., Band structure engineering and efficient injection rich-π-electrons into ultrathin g-C3N4 for boosting photocatalytic H2-production. Applied Surface Science, 2020. **505**: p. 144564.
45. Xiong, T., et al., Bridging the g-C3N4 interlayers for enhanced photocatalysis. Acs Catalysis, 2016. **6**(4): p. 2462-2472.
46. Ge, L., C. Han, and J. Liu, Novel visible light-induced g-C3N4/Bi2WO6 composite photocatalysts for efficient degradation of methyl orange. Applied Catalysis B: Environmental, 2011. **108**: p. 100-107.

47. Yuan, Y., et al., Construction of g-C3N4/CeO2/ZnO ternary photocatalysts with enhanced photocatalytic performance. Journal of Physics and Chemistry of Solids, 2017. **106**: p. 1-9.
48. Chen, D., et al., A nanosheet-like α-Bi2O3/g-C3N4 heterostructure modified by plasmonic metallic Bi and oxygen vacancies with high photodegradation activity of organic pollutants. Separation and Purification Technology, 2018. **193**: p. 232-241.
49. Inamdar, D.Y., et al., Room temperature ferromagnetism and photoluminescence of Fe doped ZnO nanocrystals. The Journal of Physical Chemistry C, 2011. **115**(48): p. 23671-23676.
50. Venkatesh, N., et al., Sunlight-driven enhanced photocatalytic activity of bandgap narrowing Sn-doped ZnO nanoparticles. Environmental Science and Pollution Research, 2021. **28**(13): p. 16792-16803.
51. Tuc Altaf, C., et al., Inverted Configuration of Cu (In, Ga) S2/In2S3 on 3D-ZnO/ZnSnO3 Bilayer System for Highly Efficient Photoelectrochemical Water Splitting. ACS Sustainable Chemistry & Engineering, 2020. **8**(40): p. 15209-15222.
52. Bhatia, S., N. Verma, and R. Bedi, Sn-doped ZnO nanopetal networks for efficient photocatalytic degradation of dye and gas sensing applications. Applied Surface Science, 2017. **407**: p. 495-502.
53. Ghattavi, S. and A. Nezamzadeh-Ejhieh, A visible light driven AgBr/g-C3N4 photocatalyst composite in methyl orange photodegradation: focus on photoluminescence, mole ratio, synthesis method of g-C3N4 and scavengers. Composites Part B: Engineering, 2020. **183**: p. 107712.
54. Wu, S., et al., Type II heterojunction in hierarchically porous zinc oxide/graphitic carbon nitride microspheres promoting photocatalytic activity. Journal of colloid and interface science, 2019. **538**: p. 99-107.
55. Clament Sagaya Selvam, N., J.J. Vijaya, and L.J. Kennedy, Effects of morphology and Zr doping on structural, optical, and photocatalytic properties of ZnO nanostructures. Industrial & engineering chemistry research, 2012. **51**(50): p. 16333-16345.
56. Javid, M.A., et al., Synthesis and study of structural properties of Sn doped ZnO nanoparticles. Materials Science-Poland, 2016. **34**: p. 741-746.

57. Ahmed, A.Z., et al., Fabrication and characterization of B/Sn-doped ZnO nanoparticles via mechanochemical method for photocatalytic degradation of rhodamine B. Inorganic and Nano-Metal Chemistry, 2020: p. 1-10.
58. Beura, R., R. Pachaiappan, and P. Thangadurai, A detailed study on Sn4+ doped ZnO for enhanced photocatalytic degradation. Applied Surface Science, 2018. **433**: p. 887-898.
59. Mott, N.F. and E.A. Davis, Electronic processes in non-crystalline materials. 2012: Oxford university press.
60. Humayun, Q., M. Kashif, and U. Hashim, Structural, optical, electrical, and photoresponse properties of postannealed Sn-doped ZnO nanorods. Journal of Nanomaterials, 2013. **2013**.
61. Tariq Jan, J.I., et al., Sn doping induced enhancement in the activity of ZnO nanostructures against antibiotic resistant S. aureus bacteria. International journal of nanomedicine, 2013. **8**: p. 3679.
62. Danwittayakul, S., M. Jaisai, and J. Dutta, Efficient solar photocatalytic degradation of textile wastewater using ZnO/ZTO composites. Applied Catalysis B: Environmental, 2015. **163**: p. 1-8.
63. Lin, Q., et al., Controlled preparation of P-doped g-C3N4 nanosheets for efficient photocatalytic hydrogen production. Chinese Journal of Chemical Engineering, 2020. **28**(10): p. 2677-2688.
64. Hao, R., et al., In situ hydrothermal synthesis of g-C3N4/TiO2 heterojunction photocatalysts with high specific surface area for Rhodamine B degradation. Applied Surface Science, 2017. **411**: p. 400-410.
65. Raza, A., H. Shen, and A.A. Haidry, Novel Cu2ZnSnS4/Pt/g-C3N4 heterojunction photocatalyst with straddling band configuration for enhanced solar to fuel conversion. Applied Catalysis B: Environmental, 2020. **277**: p. 119239.
66. Ameen, S., et al., Influence of Sn doping on ZnO nanostructures from nanoparticles to spindle shape and their photoelectrochemical properties for dye sensitized solar cells. Chemical Engineering Journal, 2012. **187**: p. 351-356.
67. Shanmugam, V. and K.S. Jeyaperumal, Investigations of visible light driven Sn and Cu doped ZnO hybrid nanoparticles for photocatalytic performance and antibacterial activity. Applied Surface Science, 2018. **449**: p. 617-630.

68. Santhi, K., et al., Synergic effect of Sn-doped TiO2 nanostructures for enhanced visible light photocatalysis. Journal of Materials Science: Materials in Electronics, 2021: p. 1-19.
69. Danwittayakul, S., et al., Enhancement of photocatalytic degradation of methyl orange by supported zinc oxide nanorods/zinc stannate (ZnO/ZTO) on porous substrates. Industrial & Engineering Chemistry Research, 2013. **52**(38): p. 13629-13636.
70. Panimalar, S., et al., Studies of MnO2/g-C3N4 hetrostructure efficient of visible light photocatalyst for pollutants degradation by sol-gel technique. Surfaces and Interfaces, 2020. **20**: p. 100512.
71. Ngullie, R.C., et al., Synthesis and Characterization of Efficient ZnO/g-C3N4 Nanocomposites Photocatalyst for Photocatalytic Degradation of Methylene Blue. Coatings, 2020. **10**(5): p. 500.
72. Sane, P., et al., Photocatalytic reduction of chromium (VI) using combustion synthesized TiO2. Journal of Environmental Chemical Engineering, 2018. **6**(1): p. 68-73.
73. Cheng, Q., et al., Hexavalent chromium removal using metal oxide photocatalysts. Applied Catalysis B: Environmental, 2015. **176-177**: p. 740-748.
74. Idris, A., et al., Photocatalytic magnetic separable beads for chromium (VI) reduction. Water Research, 2010. **44**(6): p. 1683-1688.
75. Ravishankar, T.N., et al., Ionic liquid assisted hydrothermal syntheses of Au doped TiO2 NPs for efficient visible-light photocatalytic hydrogen production from water, electrochemical detection and photochemical detoxification of hexavalent chromium (Cr6+). RSC Advances, 2017. **7**(68): p. 43233-43244.
76. Testa, J.J., M.A. Grela, and M.I. Litter, Heterogeneous Photocatalytic Reduction of Chromium(VI) over TiO2 Particles in the Presence of Oxalate: Involvement of Cr(V) Species. Environmental Science & Technology, 2004. **38**(5): p. 1589-1594.
77. Behnajady, M.A., et al., Influence of operational parameters and kinetics analysis on the photocatalytic reduction of Cr(VI) by immobilized ZnO. Environmental Technology, 2012. **33**(3): p. 265-271.
78. Safari, G.H., et al., Photocatalytic degradation of tetracycline using nanosized titanium dioxide in aqueous solution. International Journal of Environmental Science and Technology, 2015. **12**(2): p. 603-616.

79. Stancl, H.O.N., K. Hristovski, and P. Westerhoff, Hexavalent Chromium Removal Using UV-TiO2/Ceramic Membrane Reactor. Environmental Engineering Science, 2015. **32**(8): p. 676-683.

CHAPTER 5

5. CONCLUSION

Semiconductor metal oxides have received widespread attention due to their unique properties, which highlight their potential for application in photocatalysis. However, there is still a need for further development of semiconductor metal oxides with advanced physicochemical properties in order to enhance their practical application for use in wastewater treatment. One of the main factors that limits them from being practically viable is the fast recombination of electron-hole pairs. Hence there is a growing interest in developing photocatalysts which can overcome the fast recombination process.

The highlights of this work was to synthesise and characterize ternary metal oxide of Zn_2SnO_4 nanoparticle and form heterojunction of Zn_2SnO_4-ZnO incorporated into graphitic carbon nitride (g-C_3N_4) for application as a photocatalyst for the reduction of hexavalent chromium to trivalent chromium: Cr(VI) to Cr(III).

The objectives were to analyse the morphology and optical properties of the photocatalysts prepared, then followed with the evaluation of the photocatalytic ability of the nanocomposites to effect the reduction of Cr(VI) to Cr(III). The interest in the removal of the hexavalent chromium is inspired by its toxicity to both humans and animals. Hexavalent chromium is carcinogenic, genotoxic, and hemotoxic. When it enters the bloodstream, it causes oxidation reactions that result in damaging of the blood cells. This oxidative damage could result in hemolysis and, ultimately cause kidney and liver failures.

Pristine zinc oxide, tin doped ZnO and heterojunction of Zn_2SnO_4-ZnO were prepared. The complex metal oxide, Zn_2SnO_4-ZnO heterojunction, was incorporated into graphitic carbon nitride. X-ray diffraction (XRD) was used to study the polymorph and crystallinity of the nanoparticles. The pristine zinc oxide showed a decrease in crystallinity as concentration of dopant increased. Highly crystalline Zn_2SnO_4-ZnO nanoparticles were successfully synthesized using high temperature solid state reaction. XRD results reveal that Zn_2SnO_4 nanoparticles have spinel cubic structure with a crystallite size ranging from 1.11 nm to 90.6 nm with increase in Sn concentration.

Scanning electron microscopy and Transmission electron microscopy were used to study the morphologies of the synthesised nanoparticles. The SEM results showed that the pristine ZnO at lower Sn concentration (2 & 5%) had spherically shaped nanoparticles, 10% Sn presents

ZnO nanoparticles with plate-like structures, which became quasi-spherical at 15% Sn concentration and finally more spherical morphology as the concentration reached 20%. While the Zn_2SnO_4-ZnO showed the admixture of cubic and rectangular particles, thus, confirming formation of the heterojunction. A change in morphology was also observed with the dominance of nanoparticles with cubic morphology, therefore suggesting that the morphology was influenced by increase in the Sn concentration.

The SEM result for g-C_3N_4 incorporated nanoparticles showed the co-existence of the nanoparticles. The Zn_2SnO_4-ZnO nanocubes were deposited on the surface of the g-C_3N_4, indicating the formation of ternary g-C_3N_4/Zn_2SnO_4-ZnO composites. TEM image confirmed the cubic morphology of the Zn_2SnO_4 nanoparticles, and the lattice space distance measured from HRTEM image corresponds well with d-spacing values of (111) and (100) planes.

The optical properties were studied using photolumiscence and UV-vis spectroscopy. The PL spectra of both the Sn doped ZnO and Zn_2SnO_4-ZnO nanoparticles showed a red shift with increase in Sn concentration. A decrease in the PL intensity was observed in the ternary nanocomposite formed from coupling Zn_2SnO_4-ZnO with g-C_3N_4. This could be as result of inhibition of electron-hole recombination, thus an increase in its photocatalytic activity is expected.

The results from the UV-vis analysis showed that the absorption spectrum of the nanoparticles was in the UV region. The band gap of the samples was estimated by Tauc plot. The bandgap of pristine ZnO and Sn doped ZnO were recorded to be 3.61 to 3.08 eV with increase in Sn concentration. While Zn_2SnO_4 nanoparticle showed a range from 3.17 to 3.1eV, therefore showing a slight change with increase in Sn concentration which was in line with reported values.

The photocatalytic performance of the nanocomposite was evaluated by studying the photocatalytic reduction of potassium dichromate under UV light irradiation. The two catalysts g-C_3N_4/ ZTO-ZnO@20 and g-C_3N_4/ ZTO-ZnO@30 were used to study the effects of solution pH on the Cr(VI) reduction. The solution pH was varied from 2 to 8. In both cases, the catalysts removed very little fraction of Cr(VI) in all pH range. However, increase in irradiation time increased the degradation rate of Cr(VI) to Cr(III) up to 120 min. The pH 2 solution had the highest removal of Cr(VI) at 99.2 and 72% followed by pH 4 with 85.6 and 50%, then pH 6 was 57.2 and 38%, and lastly pH 8, with 35 and 25% respectively showing the lowest efficiency at pH 4, suggesting that the photocatalytic removal of Cr(VI) increased

with decrease in solution pH. The reduced removal rate observed at higher pH could be attributed to the deposition of $Cr(OH)_3$ on the surface of the catalysts which could be ascribed to the adsorption of Cr(VI) on to the surface of catalysts and its subsequent redox reaction.

The effect of photocatalyst dosage was only performed for the (g-C_3N_4/ ZTO-ZnO@20) composite due to its efficiency within the solution pH. The dosage was varied between 0.5-2.0 g. The removal rate of chromium increased with increase in the catalyst dosage, which was attributed to the availability of more active sites at higher catalyst loading. The highest percentage chromium removal was found to be 99.2% at photocatalyst loading of 2 g/ L and the lowest being 64% for 0.5g/L. Furthermore, the effect of initial concentration of Cr(IV) on the rate of reduction was also studied. The concentrations of Cr(VI) was investigated within the range of 10 to 150 ppm, and the result showed that the more irradiation time was required for complete removal of Cr(VI) as the initial Cr(VI) concentration increased. The observation could be as a result that as Cr(VI) concentration increased, the path length of photons entering into the reaction mixture decreased, and only fewer photons could reach the catalyst's surface.

The results obtained by comparing their correlation coefficient (R^2) values suggested that pseudo-first order model well described the photocatalytic activity of g-C_3N_4/ ZTO-ZnO@20 on the reduction of Cr(VI) to Cr(III) compared to pseudo- second order kinetics model. The reaction rate constants (k) for the photocatalytic reduction of Cr(VI) were evaluated from experimental data using the linear regression analysis method. The constants k_1 and k_2 (first and second order reaction rate constants) were obtained as 19.6 and 1.4 g/mg.min respectively

Also, the increase in overall rate constant k with an increase in initial Cr(VI) concentration could be due to the transition from the kinetics control regime at low concentrations to mass transfer limitations at high concentrations. These results were in agreement with earlier reported studies.

RECOMMENDATIONS

The following recommendations have been drawn based on the studies conducted and the results obtained**:**

- The synthesis of the heterojunction nanocomposites of Zn_2SnO_4-ZnO incorporated into functionalised graphitic carbon nitride such as the nitrogen, oxygen doped graphitic carbon nitride and protonated graphitic carbon nitride could be explored for the purpose of comparing both the properties and efficiency
- The prepared nanoparticles could be evaluated for degradation of other heavy metals such as lead.
- Real wastewater from mining industries containing Cr(VI) should be used for photocatalytic analysis of the nanomaterials as part of future studies.